POLITECNICO
MILANO 1863

SCUOLA DI INGEGNERIA INDUSTRIALE
E DELL'INFORMAZIONE

Preliminary assessment for a miniaturized small body terrain sampler

Tesi di Laurea Magistrale in
Space Engineering - Ingegneria Spaziale

Author: **Giulia Sala**

Student ID: 968416
Advisor: Prof. Michèle Lavagna
Co-advisors: Jacopo Prinetto
Academic Year: 2022-23

Abstract

Asteroid mining has always had an important role in the space exploration history. This especially because certain types of asteroids have resulted to be made of materials which could be seen as a source of resources. Thus, studies about asteroids could enhance not only the continuous research of proving the existence of others forms of life but also the future exploration and colonization of planets different from Earth.
Contemporary drilling missions in extreme environments have the necessity of exploiting large and heavy rovers. However, reaching specific areas of some asteroids, through big satellites or rovers, could be a problem. In this work a 1U compact sampling mechanism with integrated bio-marker analyzer has been preliminarily designed with the goal of improving the present drilling missions scenario.
Deimos has been considered as the case study of this work, because it has been discovered that Deimos composition is similar to carbonaceous asteroids. Moreover, the TASTE mission, with the goal of sampling and in-situ analyzing Deimos soil, could be a possible application case of this work. The compact 1U Surface Sample Analyzer will be the payload of a lander which will land on Deimos. The soil sampling mechanism is a hollow screw which drills the soil few centimeters' depth thanks to a dedicated electric motor. While drilling, the sampled material is transported upwards and is directly delivered into the experimental chamber. In the latter, the sampled soil properties are studied thanks to a Lab-On-Chip.
In this thesis the scientific instrument has been considered an independent and multi-scenario analyzer which could be exploited also on other missions not related to Deimos. The main guiding parameters to preliminarily design the components of the payload, such as thrust, torque and power which have to be exerted by the drill bit, have been carried out from a testing activity involving micro corers conducted by Leonardo Robotics team in Nerviano.
Keywords: asteroid mining, Deimos, CubeSat, Lab-On-Chip, micro corers.

Abstract in lingua italiana

L'estrazione mineraria dagli asteroidi ha sempre avuto un ruolo importante nella storia dell'esplorazione spaziale. Questo specialmente perchè alcuni tipi di asteroidi sono risultati essere costituiti da materiali che possono essere fonte di risorse. Così, gli studi riguardanti gli asteroidi potrebbero migliorare non solo la continua ricerca della prova dell'esistenza di nuove forme di vita ma anche la futura esplorazione e colonizzazione di pianeti differenti dalla Terra.
Al giorno d'oggi le missioni di perforazione in ambienti estremi hanno la necessità di impiegare grandi e pesanti rovers. Tuttavia, raggiungere specifiche aree di alcuni asteroidi, attraverso l'impiego di grandi satelliti o rovers, potrebbe essere un problema. In questo lavoro un compatto meccanismo di campionatura con un integrato analizzatore con bio-marcatore con dimensioni di 1U è stato preliminarmente progettato con lo scopo di migliorare l'attuale situazione delle missioni di perforazione.
Deimos è stato considerato il caso di studio di questo lavoro perchè è stato scoperto che la composizione di Deimos è simile a quella degli asteroidi carboniosi. Inoltre, la missione TASTE, con l'obiettivo di campionare e analizzare in-situ il terreno di Deimos, potrebbe essere un possibile caso applicativo per questo lavoro di tesi. Il compatto analizzatore di campioni di superficie con dimensioni di 1U sarà il payload del lander che atterrerà su Deimos. Il meccanismo di campionatura del terreno è costituito da una vite cava che penetra il terreno per qualche centimetro di profondità grazie a un dedicato motore elettrico. Durante la penetrazione, il materiale campionato è trasportato verso l'alto ed è direttamente rilasciato nella camera sperimentale. In quest'ultima, le properietà del terreno campionato sono studiate grazie a un Lab-On-Chip.
In questa tesi lo strumento scientifico è stato considerato un indipendente analizzatore multi-scenario che potrebbe essere impiegato anche in altre missioni non relative a Deimos. I principali parametri guida per il design preliminare dei componenti del payload, come forza, coppia e potenza che devono essere esercitate dalla punta del trapano, sono stati ricavati da test su micro carotatori condotti dal team di Robotica di Leonardo a Nerviano.
Parole chiave: estrazione mineraria dagli asteroidi, Deimos, CubeSat, Lab-On-Chip, micro carotatori.

Contents

Introduction

The aim of this chapter is to introduce the reasons which have guided this thesis' work. A brief review about the interest in mining missions to asteroids has been conducted. Then, it has been introduced which and how soil properties influence the drilling activities and the thesis' case study. Eventually, it has been highlighted the innovative contribution that a compact sampling mechanism with integrated bio-marker analyzer will bring in the nowadays acquisition missions scenario.

Asteroid mining

Scientists are interested in studying Near-Earth Objects, especially asteroids, because they could be a sort of supply of resources for future exploration missions [1]. This is justified by the fact that the acquired materials from M-type asteroids could be exploited in the development of innovative structures for space applications [1]. While, C-type asteroids could support life in space as they have been resulted to be rich of water and carbon [1]. This aspect has become particularly important for the research of the presence of others forms of life in our solar system as well as for the humans' desire to colonize Mars or other planets similar to Earth. Moreover, future exploration missions could be improved by the exploitation of asteroids molecules for the generation of fuel and oxidizer implied in chemical propulsion systems [1]. Eventually, water represents a sort of shielding against different radiations sources present in space, hence, it could be useful in different missions' scenario or space applications [1]. Different missions, with the goal of sampling and analyzing in situ asteroids soil samples, have been developed during the space exploration history. All the past mining missions to NEOs, and in particular to asteroids, have few common characteristics. The first one: drills are capable of reaching at least 1 m depth. The second one: the penetrating mechanisms are substantially composed by a drill rod with an integrated sampling tube which picks up samples thanks to a dedicated electromagnetic mechanism by releasing a spring [11]. Another common way to acquire the desired amount of soil is moving, again through a spring, the coring tube integrated in the sampling tube to create an empty space to be filled with the samples

during the acquisition and to push them out during the release [66]. The aforementioned characteristics traduce into the need of having long length and massive rods which make up complex penetrating mechanisms and which cannot be placed inside a CubeSat. This thesis is a kind of innovative one since it wants to lead the basis for designing a compact and very simple analyzer with integrated sampling mechanism.

Soil properties influencing drilling activities

Analytical investigations taking into account the drill characteristics as well as different soil's properties and behavior have to be developed to preliminarily study the performance of a drilling activity [2]. The soil response, caused by the thrust and torque exerted by the drill bit, depends, of course, on the values of the applied loads, but also on various geotechnical properties of the soil itself [2]. These soil's properties are:

- The shear strength, or compressive strength. This strength is influenced by two contributes: the cohesive strength and the frictional strength [2]. The latters are strictly related to the intra particle cohesion forces and the angle of internal friction of the soil. These are intrinsic contact properties present between particle grains which must be overcome to allow the movements of grains permitting sampling and acquisition activity [2].
- The bulk density. As can be expected, while drilling the resistance increases with the increasing of the soil's bulk density [2].
- The shape and size of grains. In fact, circular grains tend to be easier to drill with respect to grains having different shapes and rocks made of smaller grains tend to be stronger than the others [2].

However, analytical studies are not always able to represent all the possible different scenarios which can be met during a drilling mission. While designing a sampling tool, also unexpected events have to be taken into account. For example, the acquisition mechanism can encounter soil's areas characterized by higher density or soil's grains with shape and size different from the expected ones. Testing activities have to be performed to ensure that the drill bit has to be able to overcome these situations allowing a safe drilling. Moreover, through experimental simulations can be tested the ability of the tool to acquire samples in the effective mission environment characterized by microgravity. In fact, the latter can cause the instability of the mining system and anchoring techniques have to be introduced in order to counteract the microgravity effect [33].

Case study: Deimos soil

The aim of the thesis is to preliminarily design a miniaturized small body terrain sampler, thus, which is able of working in a microgravity environment. Moreover, the main objective of the sampling mechanism is the analysis of asteroids soils. Hence, the Deimos soil has been considered as the case study of this work. This because it has been discovered that both Deimos and Phobos are covered by a regolith similar to the one found on D and C-type (carbonaceous chondrites) asteroids [6].

Thanks to spacecrafts which have flown by or entered into orbit around Mars, such as Mariner 9, Viking 1 and 2, and Mars Express missions, Deimos and Phobos have been explored [12]. Vikings made many new discoveries about Deimos and Phobos, such as the first mass determination showing their anomalies with respect to Mars and other asteroids due to their low densities and the fact that, as also Mariner noticed, Phobos and Deimos surfaces are covered by a fine-grained regolith of tens meters or more thickness [12]. Even though both Martian moons surfaces have resulted to be mantled in dozens to hundreds of meters of regolith [52], they show different surfaces characteristics, and Deimos surface appears to be smoother as if it has loose material on its surface [64].

The Natural History Museum (NHM), together with ESA, has started the development of a new European Space Agency Sample Analogue Collection and Curation Facility (ESA^2C) to support present and upcoming activities for technology improvement that are required for both human and robotic exploration of Mars, Phobos, Deimos, C-Type Asteroids and the Moon [37][61]. The analogue materials, which have to be developed, must replicate as far as possible the expected geological environment of the target body in terms of both geotechnical and mineralogical properties. In Table 1 have been reported the physical parameters of the regolith as applicable for the sampling tool design for Phobos, Deimos and C-type Asteroids, resulting from NHM and ESA studies [37][61].

Regolith sample properties	Values
Surface regolith (loose material vs solidified surface)	loose material
Compressive strength (applicable to loose regolith)	0.3 - 30 MPa
Bulk density (sample material)	1.2 - 2 g/cm^3
Sampled grain size	μm - 3 cm
Shape	any (rounded, tabular, elongated)
Intra particle cohesion forces	0.1 - 5 kPa
Angle of internal friction	20° - 40°
Surface temperature	min -70°C, max +110°C

Table 1: Regolith sample properties analogue to Phobos, Deimos and C-type Asteroids [37].

Thesis' expected results and impact

The expected outcome of this thesis will be the preliminary design of all the components that make up a compact and simple scientific architecture able of sampling and analyzing a small amount of soil. Therefore, at the end of this research the preliminary design of a miniaturized small body terrain sampler could be considered concluded, and the obtained results will lead to next design phase. Being able of designing such a compact architecture would be something innovative because asteroid mining has always been developed exploiting large and complex instruments actuated by a significant amount of power and housed in big rovers or satellites which are also more expensive than CubeSats. The proposed sampling mechanism integrated with bio-marker analyzer will have reduced dimensions, so it could be the payload of a CubeSat. Moreover, the TASTE mission, in which a lander, housing the aforementioned scientific instrument named Surface Sample Analyzer, with the goal of landing on Deimos surface, could be a possible application case [34]. Since the proposed architecture will be studied as an independent and multi-scenario analyzer it could become the payload of missions which have the goal of reaching and studying various extraterrestrial soils, also different from the Deimos one. Eventually, having different CubeSats, capable of sampling soil, will result in being able of sampling different samples in a wide portion of the same soil, maybe also covering areas difficult to reach through big rovers.

1 | Surface Sample Analyzer High Level Requirements

The main goal of the Surface Sample Analyzer is to acquire and in-situ analyze various soil samples at different depths. In particular, the sampler is supposed to penetrate the soil up to 2 or 3 cm depth to collect environmental pollution free samples. The soil samples are transmitted upwards into the drill bit and directly delivered into the experimental chamber. The latter is composed by a selector and an external shell. After the acquisition and the analysis of a specific soil sample, the latter is expelled, and the chamber is ready for acquiring another sample. The sampled soil analysis is performed by a Lab-on-Chip, installed and levelled to the selector's surface. To reach the desired pressure and temperature condition to permit the LoC capillarity effect and to prevent reagents degradation [39][40] and to seal the chamber, a pressurizer is injected into the selector. Also, a solvent is injected to dilute the soil sample before the analysis. After the analysis and before the discharge of the sampled soil, the chamber is depressurized to allow the vaporization of the solvent.

The SSA has been assumed to be housed inside a small lander, which allows the system to reach the soil to be sampled. For this reason the system has to be designed in order to have dimensions of 1U CubeSat. Thus, due to its reduced size, the SSA has to be characterized by a reduced mass and power consumption.

The application case of the Surface Sample Analyzer is the acquisition of asteroids soils. Thus, the system has to be able to survive and work in vacuum, hence, in presence of microgravity and out gassing condition. Moreover, the SSA components have to be kept at a temperature between their operating temperatures range and have to be protected from radiations.

If the lander, where the SSA is assumed to be housed, can be moved on the surface, which has to be studied, the acquisition activity can be performed drilling different surface areas. This has been considered as a nice to have requirement since its achievement strictly depends on the lander design.

The aforementioned SSA High Level Requirements are listed in Table 1.1.

ID	Importance	Verification	Requirement
SSA-HLR-01	M	T	The product shall be able to sample soil at different depths.
SSA-HLR-02	M	T	The product shall be able to analyze the acquired soil samples.
SSA-HLR-03	M	T	The product shall be able to expel the analyzed soil samples.
SSA-HLR-04	M	T	The product shall be able to handle inert gas.
SSA-HLR-05	M	T	The product shall be able to handle liquid.
SSA-HLR-06	M	I	The product shall have dimensions of 100x100x100 mm.
SSA-HLR-07	M	I	The product shall have a reduced mass.
SSA-HLR-08	M	T	The product shall require a reduced power supply.
SSA-HLR-09	M	T	The product shall operate in microgravity.
SSA-HLR-10	M	T	The product shall withstand out gassing.
SSA-HLR-11	M	T	The product shall operate in its admissible temperatures range.
SSA-HLR-12	M	T	The product shall be protected from radiations.
SSA-HLR-13	M	I	The product shall be the payload of a lander.
SSA-HLR-14	NH	T	The product should be able of mining different surface areas.

Table 1.1: Surface Sample Analyzer High Level Requirements list.

2 | Surface Sample Analyzer general configuration

In order to achieve the Surface Sample Analyzer goals, three different mechanisms belonging to the SSA have been identified. The first one is responsible for the rotation of the selector inside the external shell of the experimental chamber, the second one regards the translation of the experimental chamber and the third and last one is about the rotation of the drill bit. The necessary components needed to satisfy each mechanism goal are going to be presented in this chapter. It's important to point out the fact that all the components have to be housed inside a 1U CubeSat structure which protect them from the outside and which have to maintain the payload shape. Moreover, the components have to be connected through cables to receive the required power supply and commands. Eventually, the components, cables and structure have to be made of space proven materials to survive and operate in the analyzed mission environment.

2.1. Selector rotation mechanism components

The requirement of the selector rotation mechanism is to allow the selector to rotate around its symmetric axis within the external shell of the experimental chamber. This to align its hole to the feeding or discharge hole, to allow the acquisition of the sampled soil or the expulsion of the analyzed sample respectively, or to assume a neutral configuration during the soil sample analysis.
In order to satisfy the aforementioned goal of the mechanism, the following components have to be designed:

- Selector. The important aspect of the selector is its material because it has to act as a sealant when pressurized and to maintain the selector shape while rotating. Moreover, the selector has to be able to handle both gas and liquid avoiding any losses while operating in microgravity. Eventually, on the selector surface has to be installed the LoC with its sensitive surface exposed within the chamber to allow the analysis of the sampled soil.

- Motor. The motor has to ensure the rotation of the selector against the friction torque between the selector and the external shell of the experimental chamber. In particular, a stepper motor will be selected because this kind of motors present very simple open loop speed and position control, with a great accuracy of the stepping angle, high reliability, long life, because there is no sliding electrical contacts, and direct compatibility with digital control [45]. Moreover, stepper motors are ideal for positioning and slow speed operation which perfectly fit with the purpose of the selector rotation mechanism [45].
- Encoder. The stepper motor has to be coupled with an encoder to guarantee a precise alignment between the hole of the stepper motor and one specific hole of the external shell. In fact, the role of the encoder is to check the position of the stepper motor rotor [16] in a closed loop control logic as depicted in Figure 2.1.
- Driver/Controller. It has to control the motion of the motor. The driver could be also useful for reducing the step size of the motor through micro-stepping which could prevent the stepper motor from jerky movements when a slow speed is required [45].
- Motor + Encoder Case. The motor and the encoder are accommodated into a case and through it are fixed to the external shell of the experimental chamber. This because otherwise the motor case can rotate with its rotor.
- LoC. The analysis of the acquired soil can be developed thanks to the LoC.
- Pressure/Depression valve. The valve is exploited to reach the required pressure of 1 atm and temperature between 4° and 25°C to permit the LoC capillarity effect and to prevent reagents degradation [39][40] but also to depressurize the chamber which permits the vaporization of solvent after the analysis. Moreover, depressurizing the chamber, the friction contributes, caused by the selector rotation, decrease.
- Solvent + Tank. The solvent is fundamental to dilute the soil sample before it is analyzed by the LoC, and it has to be housed inside a specific tank able to avoid any liquid losses.
- Inert gas + Tank. The inert gas has to force the selector to expand to seal the entire chamber and to allow to reach the required operating condition of the LoC. A tank is needed to house the inert gas avoiding possible gas losses due to microgravity.

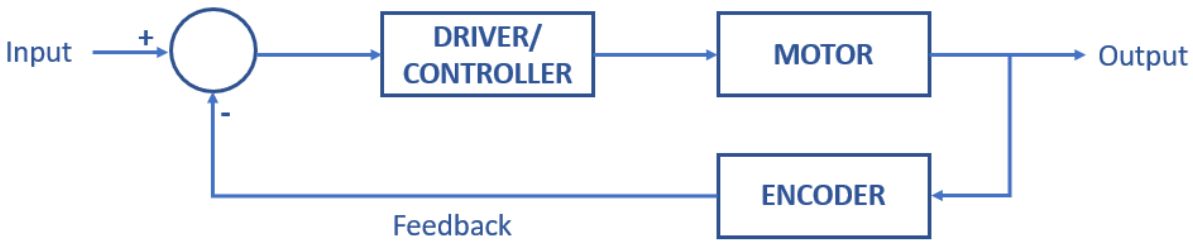

Figure 2.1: Closed loop control logic scheme.

2.2. Drill rotation mechanism components

The goals of this mechanism are basically two. The first is to provide the required torque and angular velocity by the drill for a successful drilling activity. The second is to decouple the rotation of the drill from the external shell of the experimental chamber, where the drill bit is inserted. In fact, while the drill bit rotates the experimental chamber cannot do the same.
In order to meet the aforementioned goals of the drill rotation mechanism the following components have to be designed:

- Enclosed vertical screw conveyor. It's a fundamental item in the sampling and acquisition activity, and it has to be driven by a drilling motor during the activity. Moreover, it has to convey a small quantity of soil to the experimental chamber to be analyzed by the LoC. In fact, the latter requires only few grams of soil to develop its analysis.

- Motor. The motor has to provide the necessary torque to the screw conveyor in order to allow a successful drilling activity. A stepper motor has been chosen for the benefits it can provide with respect to other kinds of motors, as already discussed in section 2.1.

- Encoder. The stepper motor has to be coupled with an encoder to guarantee a controlled rotation of the drill, while drilling, provided by the stepper motor.

- Driver/Controller. As already discussed in section 2.1, a driver coupled with the motor encoder is a fundamental item to control the stepper motor motion through a closed loop control logic.

- Motor + Encoder Case. The motor and the encoder are attached to the bottom part of the external shell of the experimental chamber through a case. This because otherwise the motor case can rotate with its rotor. The choice of having the motor

coupled with the encoder on an axis parallel to the one of the drill has been derived from the need of having a compact assembly composed by the experimental chamber and the drill bit which can vertically translate inside the 1U SSA to ensure an optimal drilling activity. This kind of solution needs a power transmission mechanism.

- Single stage spur gears. This allows the transmission of the required power by the drill bit from the stepper motor to the drill itself. In order to have a very simple power transmission, single stage spur gears have been chosen to have the minimum quantity of the simplest gears type. In fact, the stepper motor drives the pinion and is directly splined on its shaft. The pinion drives the gear and the latter is directly splined on the drill bit.
- Bearings. Two bearings result to be fundamental in order to decouple the rotation of the drill bit from the experimental chamber and to absorb the force caused by both the drill bit and the single stage spur gears while drilling.
- Bearings Spacers. The two bearings must be spaced in order to better absorb the aforementioned forces.
- Bearings + Bearings Spacers Case. The two bearings as well as the bearings spacers must be housed inside a case and has to be attached, through it, to the external shell of the chamber.

2.3. Chamber translation mechanism components

The main requirement of the chamber translation mechanism is to allow the translation of the experimental chamber coupled with the drill bit. Of course, the translation involves the whole experimental chamber comprehending the external shell, the selector and all components attached to the chamber. The latters are the coupled motor and encoder for the selector rotation and the coupled motor and encoder and its related power transmission chain for the drill bit rotation. Eventually, also the liquid and inert tank, the pressure/depression valve and the discharge apparatus has to be connected to the experimental chamber.
In order to satisfy the aforementioned goal of the mechanism the following components have to be designed:

- Linear actuator. A linear actuator is needed in order to allow the translation of the experimental chamber coupled with the drill bit during the drilling activity.

  - Motor. A stepper motor has been chosen for the benefits it can provide with respect to other kinds of motors, as already discussed in section 2.1.
  - Screw. A screw which coupled with the stepper motor can provide the required force and velocity during drilling has been selected.
  - Bearing. The addition of a bearing, at the end of the screw, to absorb the produced forces has been taken into account.

- Encoder. The stepper motor has to be coupled with an encoder to guarantee a controlled motion of the experimental chamber and the drill bit provided by the linear actuator.
- Driver/Controller. As already discussed in section 2.1, a driver is needed to regulate the motion of the stepper motor.
- Motor + Encoder Case. The motor and the encoder are attached to one of the internal surfaces 1U box housing all the components of the SSA through a case. This because otherwise the motor case can rotate with its rotor.
- Bearing Case. The bearing exploited in the linear actuator has to be housed in a case attached to one of the internal surfaces of the payload structure.
- Columns. The external shall of the chamber has to be guided in its translation driven by the linear actuator.
- External shell of chamber. The external shell of the experimental chamber has to be designed in order to have the necessary housings for the columns and the screw of the linear actuator in order to be safely moved. On the bottom surface of the external shell there must be two holes: one aligned with the enclosed conveyor, to collect soil samples, and the other one to expel the residuals after the analysis. While, on the top surface of the external shell there must be two inlets for the inert gas and solvent, and one outlet for the depressurization.
- Discharge apparatus. It has to be connected to the external shell of the experimental chamber to acquire the soil samples expelled after the analysis.

3 | Drill bit and Surface Sample Analyzer design

3.1. Drill bit design

The design of a drill bit capable of conveying the sampled regolith directly from the satellite surface to the experimental chamber will be presented in this chapter. In the latter, also a simulant with similar chemical composition and geotechnical properties to Deimos soil will be introduced. The selection of the characteristic dimensions of the drill bit, the choice of the regolith simulant and the study of their interaction during the drilling process will lead to the required thrust, torque and power by the drill to allow a safe and reliable acquisition and sampling process. Moreover, the obtained values of required thrust, torque and power will guide the mechanisms and subsystems design of the Surface Sample Analyzer.

3.1.1. Leonardo testing campaign

A testing campaign developed by the Leonardo Robotics team in Nerviano [36] aimed to study the drilling of a regolith simulant implying micro corers is going to be described in this section. The implied tools in the campaign and the experimental results which have been obtained will be the drivers for designing the drill bit and the mechanisms acting during the drilling process.

UKAM micro corers

The commercial micro corers used during the testing activity are manufactured by UKAM Industrial and feature a triple electroplated diamond layer which is applied along the cutting edge. Although these drilling tools are manufactured in several sizes and up to an outside diameter of 4”, only the three smallest versions have been tested during the campaign:

- 3EDCD1800: 1/8” of outside diameter
- 3EDCD3160: 3/16” of outside diameter
- 3EDCD1400: 1/4” of outside diameter

The three chosen tools can be visualized in Figure 3.1.

Figure 3.1: From left to right: 1/4", 3/16", 1/8" [36] - *Courtesy of Leonardo.*

For each version, five corers have been acquired and were available for the activity. In Table 3.1, the manufacturer specifications are listed.

Item No.	Outside Diameter [inch]	Shank Diameter [inch]	Recommended Velocity [rpm]
3EDCD1800	1/8 (0.125)	1/4	2500
3EDCD3160	3/16 (0.187)	1/4	2500
3EDCD1400	1/4 (0.250)	1/4	2000

(a) UKAM micro corers specifications (1/2).

Drill Length [inch]	Shank Length [inch]	Rim Depth [inch]	Drilling Depth [inch]
2-5/8	7/8	0.20	1.56

(b) UKAM micro corers specifications (2/2).

Table 3.1: UKAM micro corers specifications [36].

By default, the corers internal chamber is long as the corer itself, and it is open at both ends. In order to evaluate the tools' behavior, some corers have been modified by closing the rear opening and by reducing the sampling chamber length to 10 or 20 mm. This has made possible to perform different levels of oversampling at different depths, simply by increasing the drilling depth beyond the nominal length of the chamber as is shown in Figure 3.2.

Figure 3.2: Modified micro corers [36] - *Courtesy of Leonardo.*

Also, a fourth corer type has been internally manufactured by SES and features the same diameters of the SD2 drill sampling tool, which equipped the Philae lander in the frame of the Rosetta mission. Differently from the other corers, this one is not equipped with a diamond cutting edge. Two different versions were used for the tests: the first with a 20 mm-depth chamber, as shown in Figure 3.3, the second with a reduced 10 mm-depth chamber.

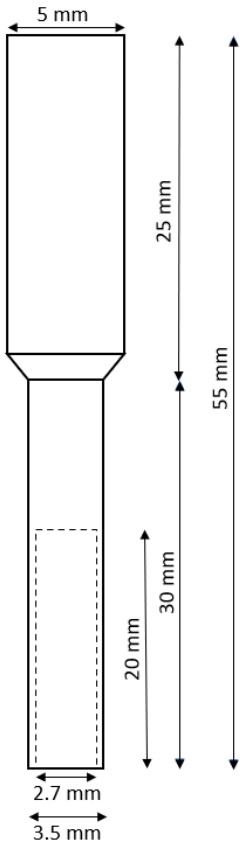

Figure 3.3: SES "SD2 derived" corer dimensions [36] - *Courtesy of Leonardo.*

Lunar highland soil simulant

The main drilling and sampling material which have been used for the testing activity was the lunar highland simulant called NU-LHT-2M. The simulant bulk material has been tested at both ambient and low temperature, frozen it to about -170 °C with different percentage of water content (0%, 5.9% and 11.9%).
Figure 3.4 reports the composition of several lunar simulants among which the above-mentioned NU-LHT-2M.

	64001/ 64002	NU-LHT-1M	NU-LHT-2M	OB-1	JSC-1	JSC-1A	JSC-1AF	FJS-1	MLS-1
Lithic fragments	31.1	–	–	–	90.9	90.9	91.9	80.2	52.3
Glass	8.9	22.4	7.2	52.6	–	–	–	0.5	36.6
Agglutinates	32.5	29.0	23.5	–	–	–	–	–	–
Plagioclase	23.3	38.8	54.9	43.9	1.5	1.5	3.4	14.1	2.6
(Plag. An%)	*95*	*80*	*80*	*75*	*68*	*70*	*70*	*50?*	*47*
Olivine	–	2.9	9.5	0.0	5.6	5.6	4.1	1.1	0.0
Clinopyroxene	0.6	2.0	4.0	0.1	1.3	1.3	0.4	1.2	2.2
Orthopyroxene	3.2	4.4	0.2	–	–	–	–	–	–
Spinel minerals	0.03	0.05	0.01	0.19	–	0.04	0.02	0.05	0.03
Fe-sulfide	0.01	0.00	0.04	–	–	–	–	–	–
Ca-phosphates	0.12	–	0.43	–	–	–	–	–	–
Ilmenite	0.1	0.3	0.2	0.0	–	0.1	0.0	0.1	1.1
Native iron	0.01	–	–	–	100	–	–	–	–
Other (sim. only)	–	0.2	0.1	3.1		0.5	0.1	2.6	5.2
Total	100	100	100	100		100	100	100	100

Figure 3.4: NU-LHT-2M mineralogy among other lunar simulants [55].

Figure 3.5 shows the geotechnical properties of NU-LHT-2M simulant with respect to other lunar simulants.

	Lunar Soil & Lunar Soil Simulants					Lunar Highland Simulants	
Geotechnical Properties	Lunar Soil	JSC-1	KLS-1	BP-1	DNA-1A	NU-LHT-2M	NAO-1
Specific Gravity, G_s	2.90 – 3.24	2.90	2.94	2.81	2.70	2.74	2.92
Fines, %	40 – 65	40 - 50	48	28	30	42	48
Coefficient of uniformity, C_u	16	7.5	12.5	10.47	5	8.46	18
Coefficient of curvature, C_c	1.2	1.12	1.28	2.61	1.3	1.54	2.34
Soil Classification (USCS)	SM/ML	SM	SM	SM	SM	SM	SM
Bulk density, ρ (g/cm^3)	1.50 – 1.66	1.55 – 1.65	1.81	1.63	1.33	1.75	1.93
Relative density, %	60 – 65	40 - 60	60	55	70	65	75
Maximum density, ρ_{max} (g/cm^3)	1.51 – 1.93	1.80	2.02	1.86	1.57	2.05	2.10
Minimum density, ρ_{min} (g/cm^3)	0.87 – 1.36	1.33	1.58	1.43	0.98	1.36	1.41
Maximum Void Ratio, e_{max}	1.21 – 2.37	1.18	0.980	3.20	1.76	1.004	1.002
Minimum Void Ratio, e_{min}	0.67 – 0.94	0.61	0.460	1.10	0.72	0.332	0.420
Maximum dry density, ρ_{dmax} (g/cm^3)	NIL	NIL	NIL	NIL	NIL	1.87	NIL
Optimum moisture content, %	NIL	NIL	NIL	NIL	NIL	15.2	NIL
Average porosity, n (%)	52 – 46	49	40	64	55	37	40
Cohesion stress, c (kPa)	0.1 – 1	1.00	1.85	2	0	0.1	0
Angle of internal friction, ϕ (deg)	30 – 50	45	44.9	45	44 – 47	38.5	46.6
Compression Index, C_c	0.01 – 0.11	0.26	0.29	0.042	0.224	0.060	NIL
Recompression Index, C_r or Swelling Index, C_s	0.000 – 0.013	NIL	0.004	0.006	0.013	0.001	NIL

Figure 3.5: NU-LHT-2M geotechnical properties among other lunar simulants [63].

Two different stocks of NU-LHT-2M, coming from two different suppliers, have been used for the testing activity. The first simulant stock was supplied by the USGS, while the second one has been more recently supplied by Zybek Advanced Products. Although these two materials are theoretically supposed to be equivalent, they show significant differences in terms of density, appearance and cohesiveness.
In particular:

- Density results to be approximately 10% higher for the Zybek material

- Cohesiveness properties result to be significantly poorer for the Zybek material, especially in dry conditions.

For the tests both materials have been used, especially with respect to the dry-soil condition.

Testing session results and comments

Analyzing the experimental results of Leonardo testing session, reported in Figure 3.6, different conclusions can be made [1][2]:

- The required force, torque and power are not sensitive to the different chamber lengths of the micro corers, so the lengths of the drilling tools can be chosen according to the customer requirements. Moreover, generally the thrust increases by increasing the coring depth, but this effect has been seen to be negligible in the aforementioned bulk and dry materials. In fact, the reported results have been obtained with different choke lengths of the corers reaching also depths few times higher the nominal chamber length to develop oversampling. While, the increasing of the thrust with the drilling depth becomes evident when solid materials are taken into account.
- The required force, torque and power are independent of the corers external diameter.
- The required force, torque and power have not shown influences from different values of the vertical and rotational speeds.
- The required force, torque and power are similar for the two lunar regolith simulants even tough they have slightly different characteristics and for the two testing conditions at ambient and low temperature.

[1] Vertical speeds are influenced by Test Equipment limitations rather than on corer performances. Vertical speeds up to 50 mm/min are feasible with similar level of thrust and torque.

[2] Experimental results showing very high values with respect to the others of the same testing sessions are wrong and can be traced back to human or Test Equipment errors. These kinds of values will be ignored.

AMBIENT - USGS	1/4"	3/16"	1/8"	SD2	1/4"	3/16"	1/8"	SD2
date	02/12/2015	02/12/2015	02/12/2015	02/12/2015	02/12/2015	02/12/2015	02/12/2015	02/12/2015
chamber length	20	20	20	20	10	10	10	10
start time	11:30:00	12:11:00	14:07:30	14:49:00	16:17:45	16:29:50	16:42:20	15:03:30
end time	11:31:00	12:12:00	14:08:00	14:49:30	16:18:00	16:30:00	16:42:30	15:03:40
TU speed [mm/min]	17.61	17.637	17.721	17.763	17.743	17.801	17.8486	17.7521
TU force [N]	0.5366	0.6592	0.45549	0.57025	0.5847	0.15839	0.1335	0.4378
TU power [W]	0.000157492	0.00019377	0.00013453	0.000168823	0.00017291	4,70E-01	3,97E-01	0.00012953
DU speed [rpm]	49.528	49.687	49.719	5.001	49.865	49.914	4.894	50.218
DU torque [Nm]	0.036942	0.03567	0.011801	0.0105	0.00223	0.0031	0.0102	0.01528

(a) USGS simulant - Dry - Ambient temperature.

LOW TEMPERATURE (-170°C) - USGS	1/4"	3/16"	1/8"	SD2	1/4"	3/16"	1/8"	SD2
date	03/12/2015	03/12/2015	03/12/2015	03/12/2015	03/12/2015	03/12/2015	03/12/2015	03/12/2015
chamber length	20	20	20	20	10	10	10	10
start time	15:25:30	15:34:15	15:45:20	16:12:00	15:52:10	15:58:15	16:05:15	16:20:30
end time	15:26:00	15:34:30	15:45:30	16:12:30	15:52:20	15:58:30	16:05:30	16:20:40
TU speed [mm/min]	18.009	18.01	18.0693	18.1077	18.0458	18.0676	18.1266	18.127
TU force [N]	128.054	45.083	3.087	0.2908	0.9223	0.26653	0.07644	0.0648
TU power [W]	0.00384354	0.00135324	0.00092967	8,78E-01	0.00027739	8,03E-01	2,31E-01	1,96E-01
DU speed [rpm]	49.886	49.873	50.021	49.794	49.933	5.021	49.485	50.083
DU torque [Nm]	0.02875	0.022438	0.019565	0.011615	0.011366	0.018099	0.01698	0.019259

(b) USGS simulant - Dry - Low temperature.

AMBIENT - ZYBEK	1/4"	3/16"	1/8"	SD2	1/4"	3/16"	1/8"	SD2
date	30/11/2015	30/11/2015	02/12/2015	02/12/2015	02/12/2015	02/12/2015	02/12/2015	02/12/2015
chamber length	20	20	20	20	10	10	10	10
start time	13:18:00	14:05:30	10:09:00	18:11:30	17:15:00	17:37:30	17:58:15	18:19:15
end time	13:18:30	14:05:40	10:09:30	18:12:00	17:15:15	17:37:45	17:58:30	18:19:30
TU speed [mm/min]	17.6272	17.6131	17.647	17.9475	17.867	17.8746	17.8632	17.9532
TU force [N]	16.677	0.7006	0.8781	0.91839	0.72934	0.4876	0.4465	0.53527
TU power [W]	0.00048995	0.00020566	0.00025826	0.00027471	0.00021719	0.00014526	0.00013293	0.00016016
DU speed [rpm]	49.625	49.734	49.418	50.128	49.997	49.085	49.812	49.868
DU torque [Nm]	0.025466	0.02926	0.021508	0.0049587	0.032603	0.048595	0.045309	0.0014938

(c) Zybek simulant - Dry - Low temperature.

LOW TEMPERATURE (-170°C) - ZYBEK	1/4"	3/16"	1/8"	SD2	1/4"	3/16"	1/8"	SD2
date	03/12/2015	03/12/2015	03/12/2015	03/12/2015	03/12/2015	03/12/2015	03/12/2015	03/12/2015
chamber length	20	20	20	20	10	10	10	10
start time	11:39:30	11:48:30	11:58:00	12:24:00	12:05:20	12:11:00	12:17:40	12:32:25
end time	11:40:20	11:49:20	11:58:30	12:24:30	12:05:40	12:11:20	12:18:00	12:32:30
TU speed [mm/min]	17.85	17.9467	17.937	18.052	17.95	17.963	17.951	18.018
TU force [N]	4.9	22.968	0.946	0.389	2.25	0.308	0.2445	0.9812
TU power [W]	0.00145775	0.000687	0.000282807	0.000117037	0.000673125	9,22E+00	7,32E+00	0.000294654
DU speed [rpm]	4.956	49.735	49.568	4.952	49.636	4.901	4.932	4.904
DU torque [Nm]	0.032	0.0274	0.0309	0.0223	0.1101	0.01969	0.0256	0.0165

(d) Zybek simulant - Dry - Ambient temperature.

Figure 3.6: Results of Leonardo testing activity [36] - *Courtesy of Leonardo.*

The experimental values of thrust, torque and power obtained during Leonardo testing campaign, reported in Figure 3.6, have been considered to lead the Surface Samples Analyzer mechanisms and subsystems design. This because the adopted lunar highland soil

simulants during the testing activity presents similar geotechnical properties to Deimos soil, as can be noticed comparing Figure 3.5 and Table 1. The drilling depths reached by the micro corers during the test sessions respect the idea of sampling and acquiring soil samples few centimeters below the soil surface of Deimos. Moreover, also the vertical and rotational speeds of the drilling tools during the testing activity can be used as operating references values for the Surface Sample Analyzer drill bit. Eventually, since the quantity of soil sampled and delivered into the experimental chamber for the analysis has to be of few grams, the external diameter dimensions of UKAM micro corers seem to satisfy this requirement. As already mentioned, the sampled material has to be transported upwards into the drill bit and directly delivered into the experimental chamber and this can not be possible implying the UKAM micro corers. This because, in order to have the soil samples reaching the chamber, more of the length of the drill tool and, as a consequence, part of the 1U box containing all the components of the Surface Sample Analyzer, should penetrate Deimos soil. In order to overcome the aforementioned problem, a small enclosed vertical screw conveyor has been preliminarily designed as described in the next section.

3.1.2. Enclosed vertical screw conveyor design

The design of a vertical enclosed screw conveyor is fundamental in order to allow the direct rising of the sampled material from the soil surface to the experimental chamber through the penetration of only a part of the total length of the conveyor. This minimum penetration depth is called choke length. For the purpose of the design, it's important to point out the fact that the screw conveyor has been considered to be attached to the conveyor shell, designed as the UKAM micro corers. Thus, differently from standards enclosed screw conveyors, the screw and the conveyor shell form a single entity.

Characteristic dimensions definition

The architecture and the characteristic dimensions of an enclosed screw conveyor are depicted in Figure 3.7.

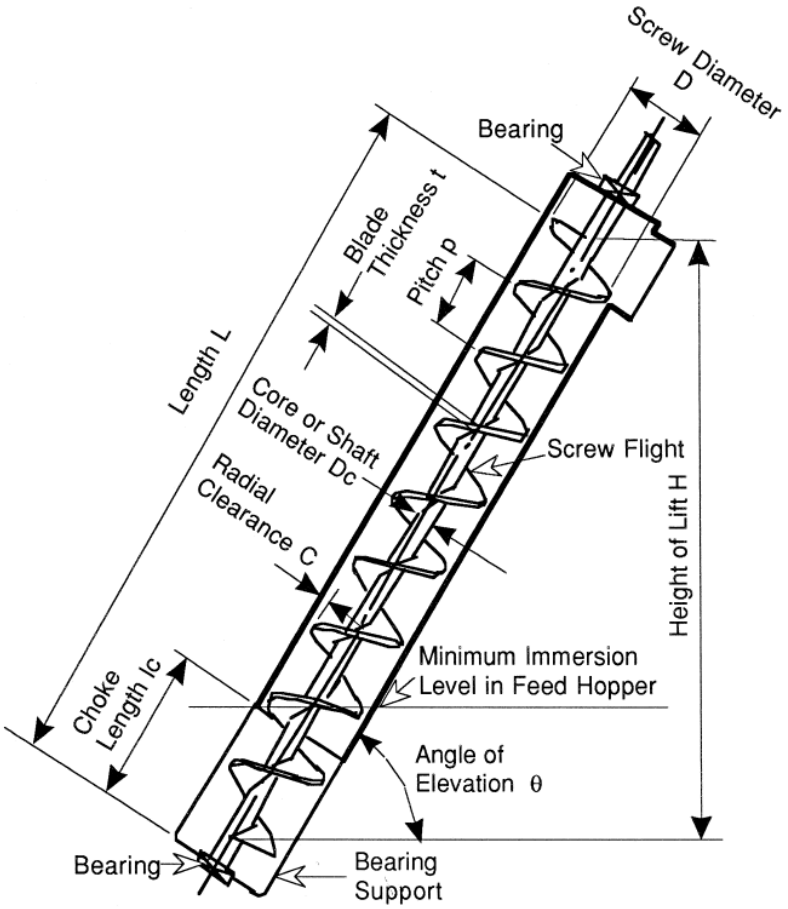

Figure 3.7: Enclosed screw or auger conveyor variables [53]

The goal is to design an enclosed vertical screw conveyor capable of conveying the necessary mass of soil inside the experimental chamber, in particular to the Lab-on-Chip, in order to be studied. As already mentioned, the LoC required only few grams of sampled soil to develop its analysis.
The design has been performed, according to [53], taking into account the expression of the volumetric maximum theoretical throughput of the screw conveyor:

$$Q_t = \frac{\pi}{4}((D + 2C)^2 - {D_c}^2)(p - t)n_L \tag{3.1}$$

Q_t is expressed in m^3/s and considers the conveyor running 100% full and the bulk material moving axially without rotation. This assumption has been made because for low values of the rotational speed of the conveyor, as in this application, the actual throughput can be replaced by the maximum theoretical one is shown in Figure 3.8.

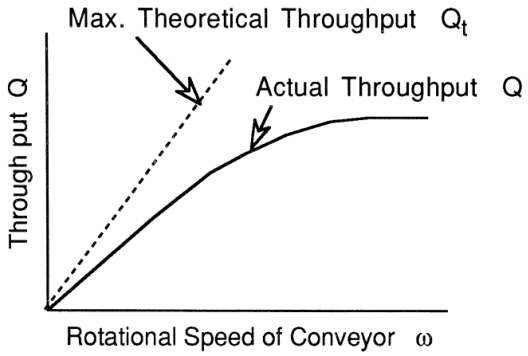

Figure 3.8: Throughput of an enclosed screw conveyor with respect to rotational speed of conveyor [53]

The maximum theoretical throughput of the enclosed auger conveyor have been evaluated considering the following inputs:

- D: the values of external diameters of drilling tools presented in Leonardo testing activity [36]: 6.35 mm (1/4"), 4.76 mm (3/16"), 3.5 mm, 3.17 mm (1/8").
- C: has supposed to be zero since the screw flight and the external shell of the conveyor are one single entity.
- D_c: varying between 1 mm and D/2. These values have been chosen according to reasonable shaft dimensions values for manufacturing.
- p: varying between 1/2D and D. This because usually standardized screw conveyors for bulk materials present a standard pitch equal to D, a short pitch equal to 2/3D, a half pitch equal to 1/2D or a long pitch equal to 1-1/2D [9]. The aforementioned values have been taken as references even tough the dimensions of the actual screw conveyor are not the standardized ones since it is smaller.
- t: 1 mm. As before, this value has been chosen according to a reasonable blade thickness value for manufacturing.
- n_L: the rotational speed of the screw conveyor: 50 rpm. This is also the rotational speed at load taken as the maximum value from Leonardo testing activity [36].

It's important to point out the fact that all these values are reasonable guesses of the characteristic dimensions to realize a small screw conveyor, but an effective design of the tool has to be developed exploiting both a mechanical and thermal analysis of the components which make up the conveyor itself.
After the computation of the volumetric throughput for the different variables listed above,

Q_m, which is the throughput value in kg/s, has been obtained as follows:

$$Q_m = \rho Q_t \tag{3.2}$$

where ρ: 1.705 kg/m^3. This is the medium density of soil simulant NU-LHT-2M, exploited in Leonardo testing activity [36], obtained through the maximum and minimum density values reported in Figure 3.5.
The preliminary design of the screw conveyor has been developed in order to obtain a small tool capable of giving the minimum mass quantity required by the LoC in a reasonable amount of time. Thus, the time required to convey different mass quantities M_{min} of material, varying from 0.1 and 5 grams, according to the maximum throughput of different screw conveyors, having different dimensions, has been computed as follows:

$$t_{min} = \frac{M_{min}}{Q_m} \tag{3.3}$$

The obtained results have been depicted as isolines representing the required time to convey the desired mass depending on the shaft diameter, the pitch and the screw diameter. Some observations can be made:

- For constant D, D_c and p, increasing M_{min}, t_{min} increases as well. This can be noticed looking at Figure 3.9.
- For constant M_{min}, D_c and p, increasing D, t_{min} decreases. This can be noticed looking at Figure 3.10.

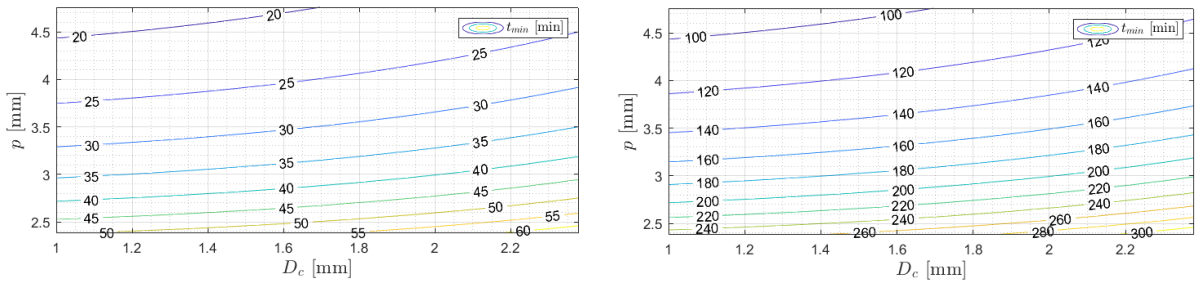

(a) $D = 4.76$ mm, $M_{min} = 0.1$ g. (b) $D = 4.76$ mm, $M_{min} = 0.5$ g.

Figure 3.9: Time at constant screw diameter and variable minimum mass.

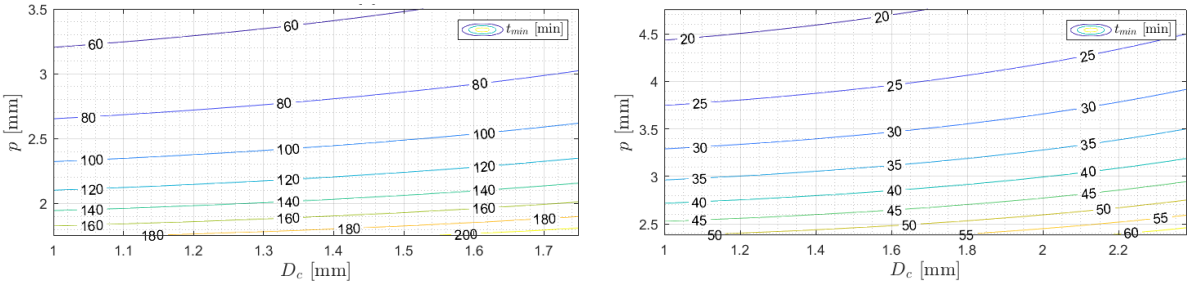

(a) $D = 3.5$ mm, $M_{min} = 0.1$ g. (b) $D = 4.76$ mm, $M_{min} = 0.1$ g.

Figure 3.10: Time at constant minimum mass and variable screw diameter.

Eventually, also the blade thickness has been changed around the aforementioned value of 1 mm, but it seems to be a non-influential parameter, especially when the screw diameter increases.

The time t_{min} needed to convey the minimum required mass along a screw conveyor has been evaluated considering different screw diameter D, 3.17 mm, 3.5 mm, 4.76 mm and 6.35 mm referring to Leonardo testing activity [36], pitch p equal to screw diameter and the shaft diameter D_c, equal to 1.5 mm for the first three screws and 2 mm for the last one. The obtained values are highlighted in Figure 3.11. The results are shown only for M_{min}= 1 because they vary linearly with it.

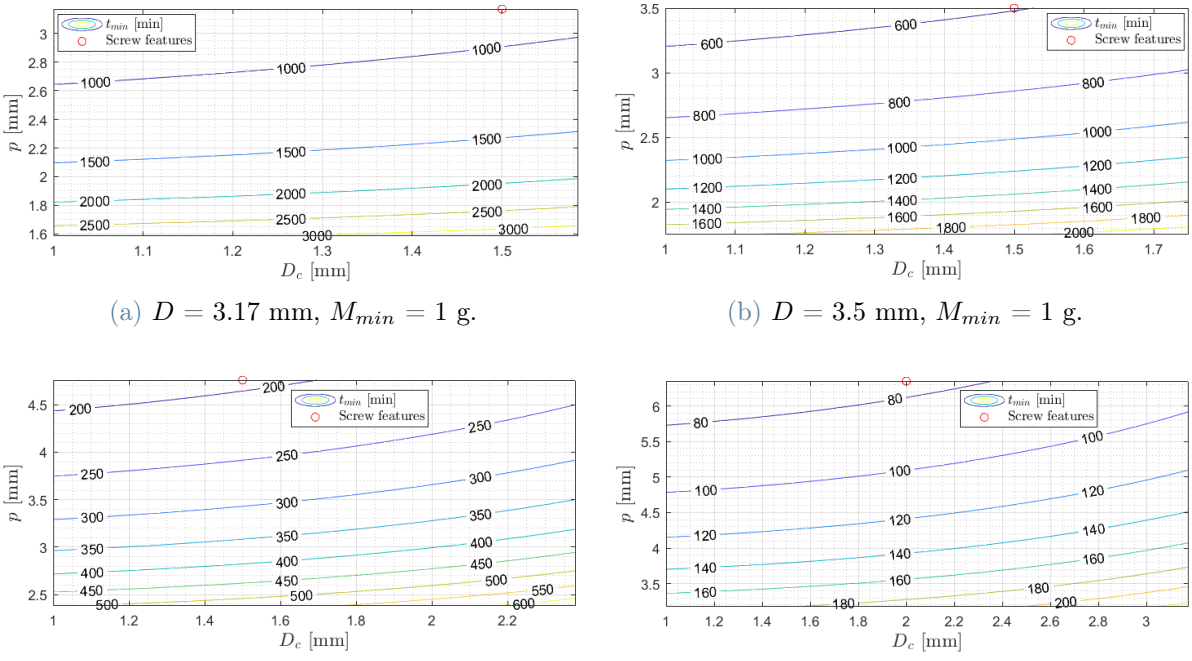

(a) $D = 3.17$ mm, $M_{min} = 1$ g. (b) $D = 3.5$ mm, $M_{min} = 1$ g.

(c) $D = 4.76$ mm, $M_{min} = 1$ g. (d) $D = 6.35$ mm, $M_{min} = 1$ g.

Figure 3.11: Time required to convey 1 g of soil through different conveyor configurations.

The choke length l_c, for each screw configuration, has been assumed equal to one time the obtained pitch. This because, according to [54], at very slow speeds, as in the considered case, a choke length of one screw pitch is sufficient to convey the required amount of grain. The obtained results are reported in Table 3.2.

	D [mm]			
	3.17	3.5	4.76	6.35
p [mm]	3.17	3.50	4.76	6.35
D_c [mm]	1.50	1.50	1.50	2.00
l_c [mm]	3.17	3.50	4.76	6.35
t_{min} [min]	882.52	597.41	194.67	76.86

Table 3.2: Time required to convey 1 g of soil through different conveyor configurations.

It's important to point out the fact that the preliminary design of the enclosed screw conveyor is independent of the total length, L, of the screw conveyor itself. The length of the screw conveyor, needed to allow a safe sampling and acquisition process, will be selected later in the design process.

Thrust, torque and power definition

Introducing an enclosed vertical screw conveyor, the thrust and torque caused by its motion as well as the required power for the drilling process have to be evaluated according to [53].
The forces acting on particles in a screw conveyor and the velocity components are both shown in Figure 3.12. As the screw rotates, a particle of bulk solid moves in a helical path of opposite hand to that of the screw. Referring to Figure 3.13, V_S is the tangential velocity of the screw at the radius considered, V_R is the relative velocity of the particle with respect to the screw surface and V_A is the absolute velocity of the considered particle. The angle α is the helix angle of the screw at a generic radius r as:

$$\alpha = \arctan\left(\frac{p}{2\pi r}\right) \tag{3.4}$$

where p is, again, the pitch.
The angle λ defines the direction of the absolute velocity and thus, the helix angle of the

path followed by the particles at a generic radius r; it is defines as:

$$\lambda < 90° - (\alpha + \phi_s) \tag{3.5}$$

where ϕ_s is the friction angle between the bulk solid and the screw surface [53].

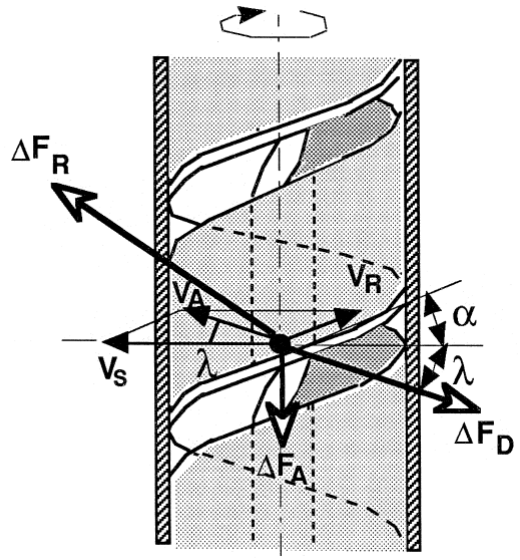

Figure 3.12: Conveying action [53].

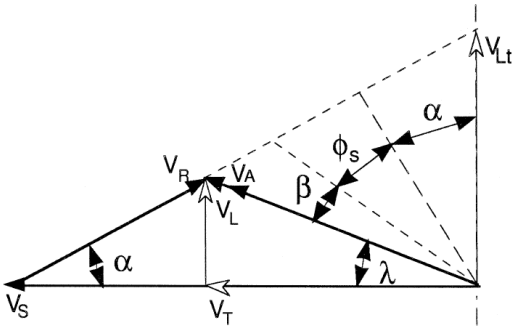

Figure 3.13: Velocity diagram [53].

The tangential velocity of the screw conveyor V_S at a radius r is defined by:

$$V_S = \omega_L r \tag{3.6}$$

where ω_L is the rotational speed of the screw conveyor.
As can be noticed from Figure 3.13, the relative motion of a particle with respect to the screw conveyor is represented by V_R which is given by:

$$V_R = \frac{V_S \sin\lambda}{\sin(\alpha + \lambda)} \tag{3.7}$$

The absolute velocity of a particle is the vector addition of V_S and V_R and its magnitude is given by:

$$V_A = \frac{V_S \sin\alpha}{\sin(\alpha + \lambda)} \tag{3.8}$$

Eventually, the absolute velocity V_A has two components: the useful conveying component

V_L and the wasteful rotational component V_T and they are respectively given by:

$$V_L = \frac{V_S \sin\alpha \sin\lambda}{\sin(\alpha+\lambda)} \quad V_T = \frac{V_S \sin\alpha \cos\lambda}{\sin(\alpha+\lambda)} \tag{3.9}$$

The forces acting on a single particle in a vertical screw conveyor are depicted in Figure 3.12 and in Figure 3.14. In the latter, the absolute velocity of a particle is also shown. As indicated in Figure 3.14, at an arbitrary radius r, a drag force ΔF_D acts in a direction opposite to the absolute velocity V_A and is expressed as:

$$\Delta F_D = \mu \Delta F_N \tag{3.10}$$

where μ is equal to the internal friction coefficient of bulk solid if the particle is at radius minor then the outer screw radius while is equal to the casing friction coefficient if the particle is at the outer screw radius, hence, in contact with the conveyor shell [53].
The aforementioned drag force ΔF_D has two components:

- ΔF_{DT}: the tangential component, which when combined with the radius and integrated over the screw surface provides the resistance torque.
- ΔF_{DA}: the axial component, which is the component required to slide the material along the conveyor casing and represents the axial force along the screw.

ΔF_A is the axial component of the particle weight of bulk material on the screw surface but, since $g \sim 0$ m/s^2, in this specific case $\Delta F_A = 0$. As a consequence, ΔF_R which is the resultant force due to sliding on the screw surface has two components, tangential and axial, which are function of the tangential and axial components of ΔF_D respectively [53]. Moreover, the helix angle λ can be stated as:

$$\lambda = 90° - (\alpha + \phi_s) \tag{3.11}$$

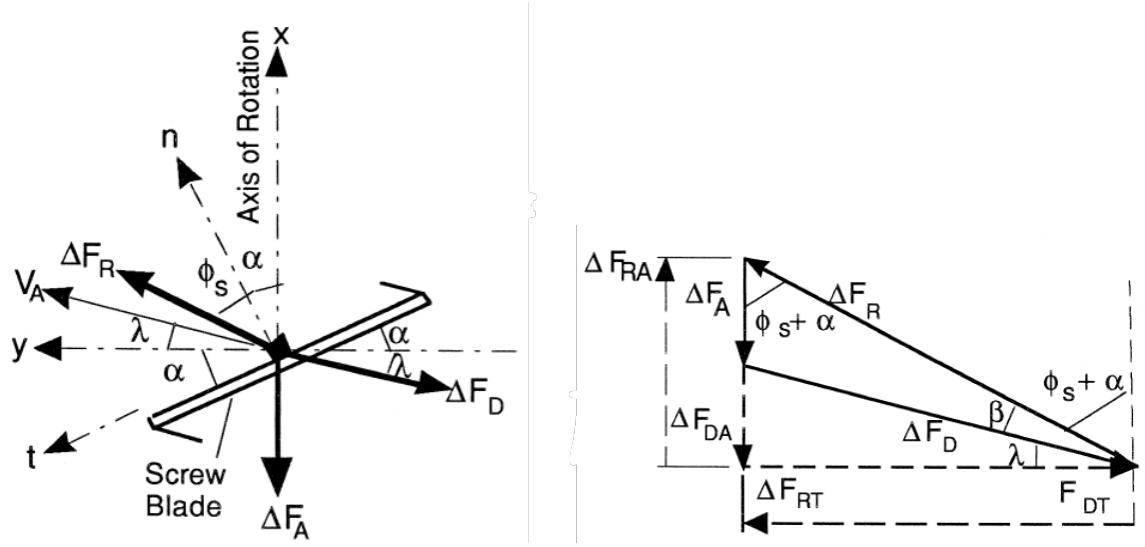

(a) Force on a particle. (b) Force diagram.

Figure 3.14: Forces acting on a granular particle [53].

According to [53]:

$$\Delta F_N = \Delta F_{Na} + \Delta F_{Nc} \tag{3.12}$$

where ΔF_{Na} is the lateral normal force which depends on the particle weight, which is negligible in this case, and ΔF_{Nc} which is the contribution due to the centrifugal force on a particle with mass ΔM situated at a generic radius r, hence:

$$\Delta F_N = \Delta M r \omega_L^2 \left(\frac{\tan\alpha}{\tan\alpha + \tan\lambda} \right)^2 \tag{3.13}$$

Recalling Equation 3.10, the drag force has been obtained as stated:

$$\Delta F_D = \mu \Delta M r \omega_L^2 \left(\frac{\tan\alpha}{\tan\alpha + \tan\lambda} \right)^2 \tag{3.14}$$

Eventually, the medium axial force and torque have been computed, respectively, as follows:

$$F_L = \mu M_{min} \omega_L^2 R_M \left(\frac{\tan\alpha_M}{\tan\alpha_M + \tan\lambda_M} \right)^2 \sin\lambda_M \tag{3.15}$$

$$T_L = \mu M_{min} \omega_L^2 R_M^2 \left(\frac{\tan\alpha_M}{\tan\alpha_M + \tan\lambda_M} \right)^2 \cos\lambda_M \tag{3.16}$$

where:

- $\mu = \tan\phi_i$, where ϕ_i is the angle of internal friction of the chosen soil simulant. The latter is $\phi_i = 38.5°$, referring to Figure 3.5, hence, the internal friction coefficient

of the bulk material is $\mu_i = \tan\phi_i = 0.8$. While, the friction coefficient between particles and screw usually varies between 0.1 and 1. Thus, it has been decided to consider $\mu = \mu_i = \tan\phi_i = 0.8$. As a consequence, $\phi_s = \phi_i = 38.5°$.

- M_{min}: varying between 0.1 and 5 grams. As before, it is the minimum mass quantity of material which have to be conveyed into the experimental chamber.
- $\omega_L = \frac{2\pi n_L}{60}$, where, as before, $n_L = 50$ rpm.
- R_M: the mean screw radius: $R_M = \frac{D/2+D_C/2}{2}$.
- α_M: at the mean screw radius: $\alpha_M = \arctan\left(\frac{p}{2\pi R_M}\right)$.
- λ_M: at the mean screw radius and with $\phi_s = \phi_i$: $\lambda_M = 90° - (\alpha_M + \phi_i)$.

As already done in subsubsection 3.1.2, axial force F_L and thrust T_L computations have been developed for four screw conveyors having different screw diameters D, 3.17 mm, 3.5 mm, 4.76 mm and 6.35 mm referring to Leonardo testing campaign [36], pitch p equal to screw diameter and the shaft diameter D_c equal to 1.5 mm for the first three screws and 2 mm for the last one. The results are highlighted in Figure 3.15 and Figure 3.16 respectively. As before, the results are shown only for M_{min}= 1 because they vary linearly with it.

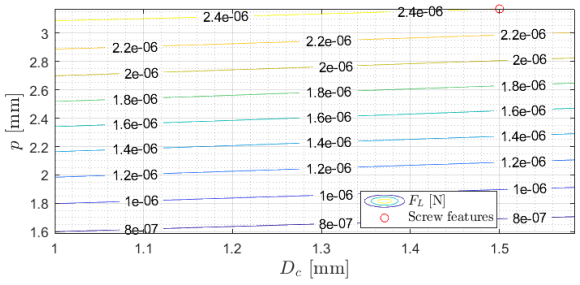

(a) $D = 3.17$ mm, $M_{min} = 1$ g.

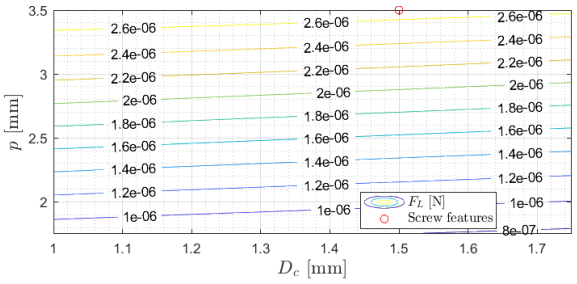

(b) $D = 3.5$ mm, $M_{min} = 1$ g.

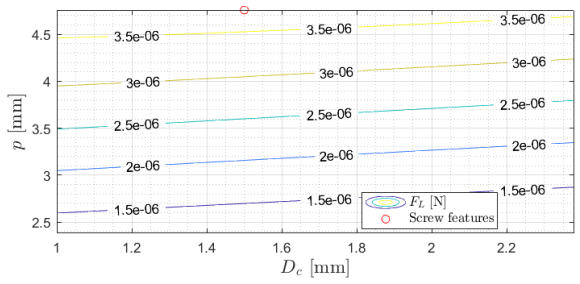

(c) $D = 4.76$ mm, $M_{min} = 1$ g.

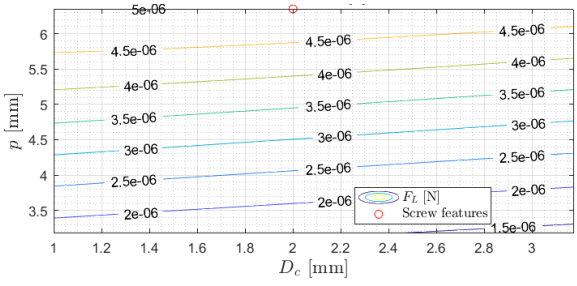

(d) $D = 6.35$ mm, $M_{min} = 1$ g.

Figure 3.15: Thrust required to convey 1 g of soil through different conveyor configurations.

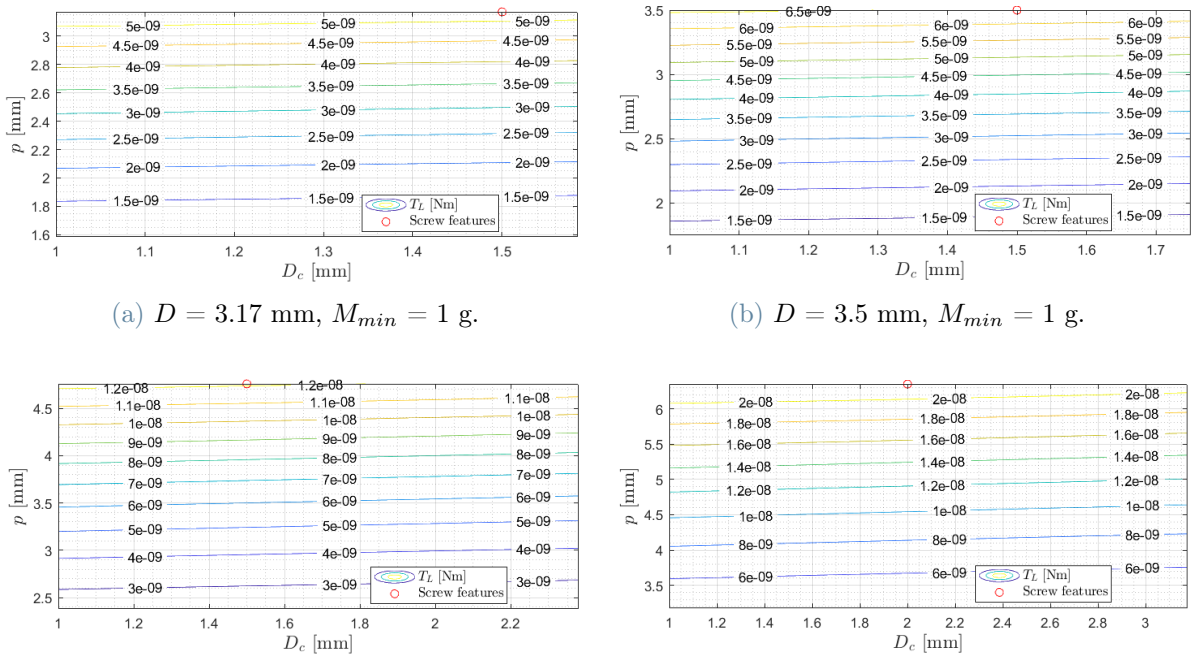

(a) $D = 3.17$ mm, $M_{min} = 1$ g.

(b) $D = 3.5$ mm, $M_{min} = 1$ g.

(c) $D = 4.76$ mm, $M_{min} = 1$ g.

(d) $D = 6.35$ mm, $M_{min} = 1$ g.

Figure 3.16: Torque required to convey 1 g of soil through different conveyor configurations.

Eventually, P_L, the power required by each micro corer to sample a minimum mass quantity equal to 1 g has been computed as follows:

$$P_L = T_L \omega_L \tag{3.17}$$

The obtained power values P_L have been computed considering different screw diameters D, 3.17 mm, 3.5 mm, 4.76 mm and 6.35 mm referring to Leonardo testing campaign [36], pitch p equal to screw diameter and the shaft diameter D_c equal to 1.5 mm for the first three screws and 2 mm for the last one. The results are indicated in Figure 3.17. As before, the results are shown only for M_{min}=1 because they vary linearly with it.

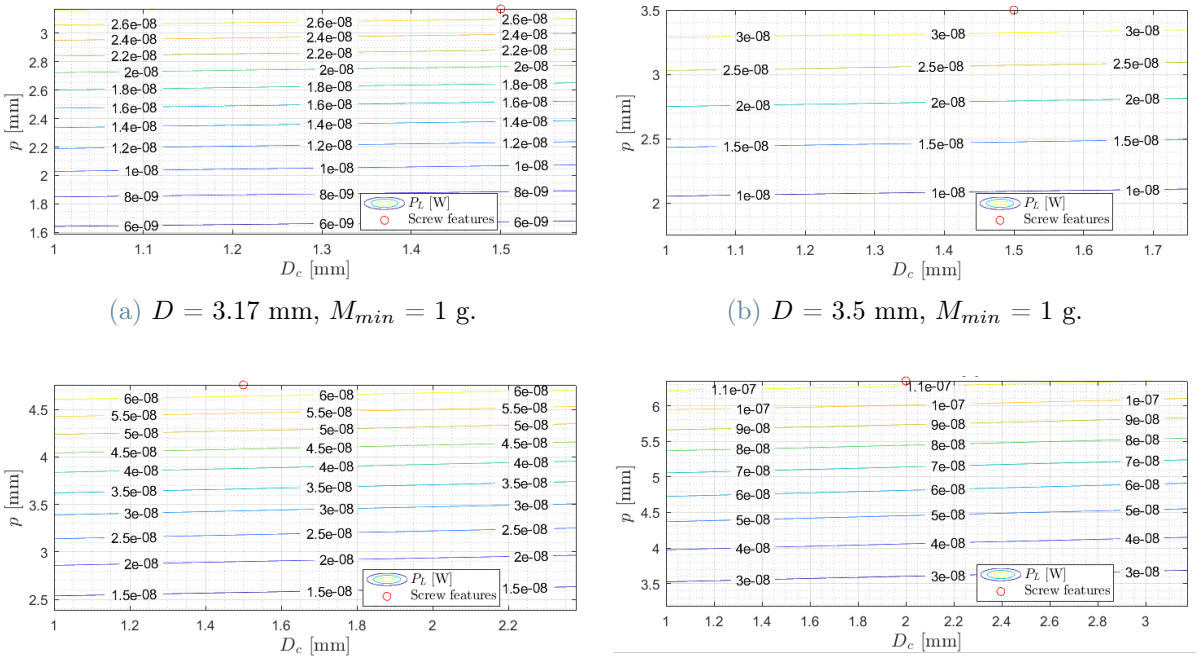

(a) $D = 3.17$ mm, $M_{min} = 1$ g.

(b) $D = 3.5$ mm, $M_{min} = 1$ g.

(c) $D = 4.76$ mm, $M_{min} = 1$ g.

(d) $D = 6.35$ mm, $M_{min} = 1$ g.

Figure 3.17: Power required to convey 1 g of soil through different conveyor configurations.

The obtained values of thrust, torque and power are reported in Table 3.3.

	***D* [mm]**			
	3.17	3.5	4.76	6.35
***p* [mm]**	3.17	3.5	4.76	6.35
***D_c* [mm]**	1.5	1.5	1.5	2
***F_L* [mm]**	2.40e-06	2.68e-06	3.72e-06	4.97e-06
***T_L* [min]**	5.24e-06	6.44e-06	1.21e-08	2.16e-08
***P_L* [min]**	2.72e-08	3.37e-08	6.35e-08	1.13e-07

Table 3.3: Thrust, torque and power required to convey 1 g of soil through different conveyor configurations.

The obtained values of required thrust, torque and power by the designed enclosed vertical screw conveyor are negligible with respect to the results of the testing activity developed by Leonardo [36]. This because the aforementioned quantities have been computed for an ideal theoretical case where all the losses have been ignored. Thus, the maximum values of vertical force, torque and power, listed in Table 3.4, have been extrapolated

from Leonardo testing activity and are summarized in Figure 3.6. These values have been taken as reference to design the mechanisms allowing the drilling process performed by the Surface Sample Analyzer. As already mentioned, experimental values of thrust, torque and power showing very high values with respect to the others of the same testing sessions are wrong and can be traced back to human or Test Equipment errors. For this reason, they have been ignored.

v_L [mm/min]	F_L [N]	P_L [W]	n_L [rpm]	T_L [Nm]
18	5	0.3	50	0.05

Table 3.4: Maximum results values from Leonardo testing activity [36]

.

Notice that P_L has been evaluated through the power definition $P_L = \frac{T_L 2\pi n_L}{60}$. Since the maximum values of T_L and n_L, from Leonardo testing activity results [36], have been taken into account, also P_L represents the maximum value of the obtained powers from Leonardo testing activity [36], excluding the very high values considered to be wrong.

Selected configuration and future developments

An enclosed vertical screw conveyor with features deriving from subsubsection 3.1.2, and summarized in Table 3.5, has been assumed as the Surface Sample Analyzer drill bit. As can be noticed from Table 3.5, the external diameter refers to the biggest UKAM micro corers which have been involved in Leonardo testing campaign [36]. This allows to convey a higher soil quantity in minor time with respect to the others micro corers.

D [mm]	p [mm]	D_c [mm]
6.35	6.35	2

Table 3.5: Surface Sample Analyzer drill bit dimensions

.

A specific configuration of the enclosed screw conveyor, involved in the sampling and acquisition activity of the SSA, was fundamental to be selected. This because the design of some SSA mechanisms depended on some features of the drill bit.
Further studies have to be conducted on the preliminarily designed enclosed screw conveyor. This because the selected configuration refers to features which have been established through manufacturing assumptions. However, as already mentioned, it has to

be verified that the designed conveyor is able to withstand both mechanical and thermal stresses during the whole drilling activity. Thus, analytical studies also taking into account all the possible sources of losses influencing the sampling activity have to be developed. This could provide also more accurate values of thrust, torque and power which the screw conveyor has to provide while drilling. Moreover, numerical simulations and testing activities have to be performed to ensure the effective conveyance of the required soil's quantity within the experimental chamber. This has to be verified even considering unexpected scenarios such as the encounter of bigger soil's grains or harder soil's areas with respect to the analyzed ones.

3.2. Surface Sample Analyzer design

In this section is going to be presented the preliminary design of the Surface Sample Analyzed. The latter has been conducted to satisfy the High Level Requirements of the system. Hence, not only mechanisms able to achieve the functional goals of the system has been preliminarily designed, but also systems to protect the mechanisms' components from the external environment and to provide them the required power have been analyzed.

3.2.1. Configuration

A preliminary configuration of the Surface Sample Analyzer has been developed in SolidWorks after the design of the components belonging to each of the three mechanisms involved in the payload activity. The components have been arranged inside the 1U external structure of the SSA compatibly with their dimensions. Further analysis have to be developed in order to ensure smooth movements of the components during the sampling and acquisition activity. This, especially during the downwards and upwards translation of the experimental chamber to avoid any risk of tilting of the latter.
The configurations of the Surface Sample Analyzer in two different Mission Phases are shown in Figure 3.18. About 15% of the total 1U volume is the occupied percentage by the preliminary designed components which have been implied to provide a possible SSA configuration.

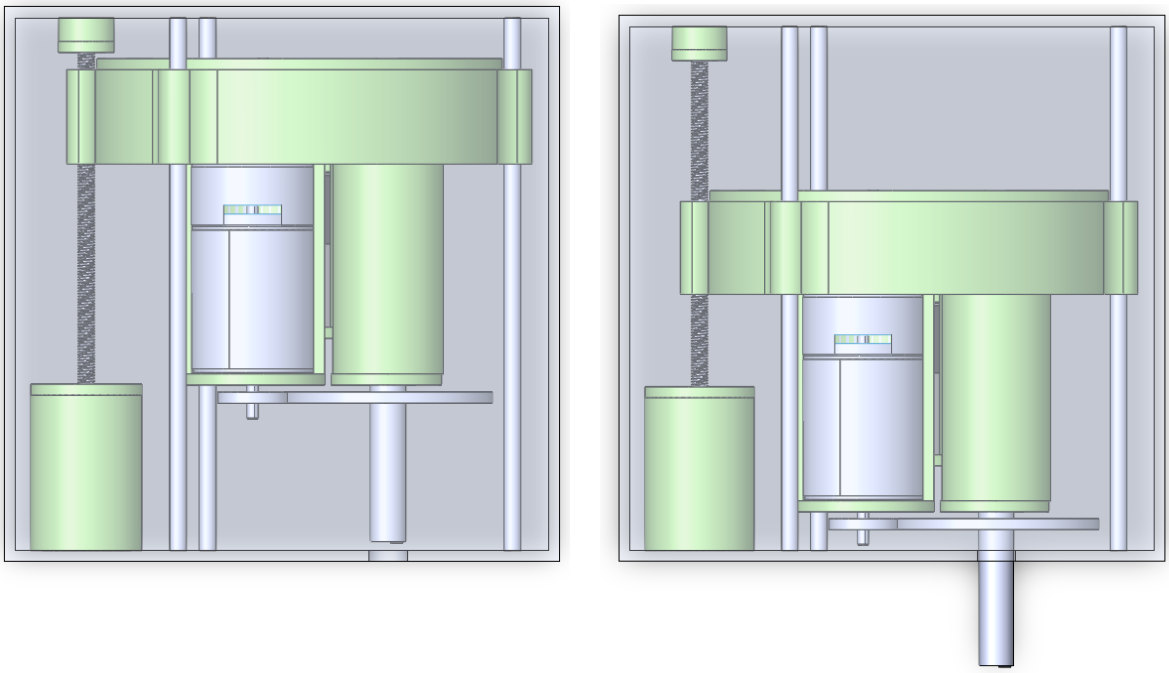

(a) SSA during Resting Phase.

(b) Maximum admissible translation of chamber and drill bit.

Figure 3.18: Different configurations of the Surface Sample Analyzer.

To identify each component of the Surface Sample Analyzer, reported in Figure 3.19, two exploded views of the payload are shown in Figure 3.20. As can be noticed from the latter, there are still missing items which have not been designed yet, and consequently, included in this preliminary SSA configuration. These components are drivers/controllers, the discharge apparatus, the two tanks housing the solvent and the inert gas, the pressure/depression valve and the cables required by each SSA component. This because the design of the cited components and their specific position within the 1U structure strictly depends on the position of the SSA inside the 3U lander and also on the relative position between the SSA analyzer components and the lander subsystems.

#	Component	Mechanism	Quantity
1	Experimental chamber (bottom)	Chamber translation	1
2	Selector	Selector rotation	1
3	Column	Chamber translation	3
4	Experimental chamber (disc)	Chamber translation	1
5	Stpper Motor AM1524RC + Encoder AE23B8	Chamber translation	2
6	Lead screw M3x0.5xL1	Chamber translation	1
7	AM1524RC + AE23B8 Case	Selector rotation	1
8	AM1524RC + AE23B8 Case (bottom)	Chamber translation	1
9	AM1524RC + AE23B8 Case (disc)	Chamber translation	1
10	Bearing 6502.00103	Chamber translation	1
11	Bearing 6502.00103 Case (bottom)	Chamber translation	1
12	Bearing 6502.00103 Case (disc)	Chamber translation	1
13	Stepper Motor AM2224RC + Encoder PE22-120	Drill rotation	1
14	Bearings + Spacers Case (bottom)	Drill rotation	1
15	AM2224RC + PE22-120 Case (bottom)	Drill rotation	1
16	Pinion	Drill rotation	1
17	AM2224RC + PE22-120 Case (disc)	Drill rotation	1
18	Bearing R4LZZC3-HMST4	Drill rotation	2
19	Belleville dsc spring	Drill rotation	1
20	Bearings + Spacers Case (disc)	Drill rotation	1
21	Outer ring spacer	Drill rotation	1
22	Inner ring spacer	Drill rotation	1
23	Enclosed screw conveyor	Drill rotation	1
24	Gear	Drill rotation	1
25	LoC	Selector rotation	1

Figure 3.19: SSA components list with relative labels.

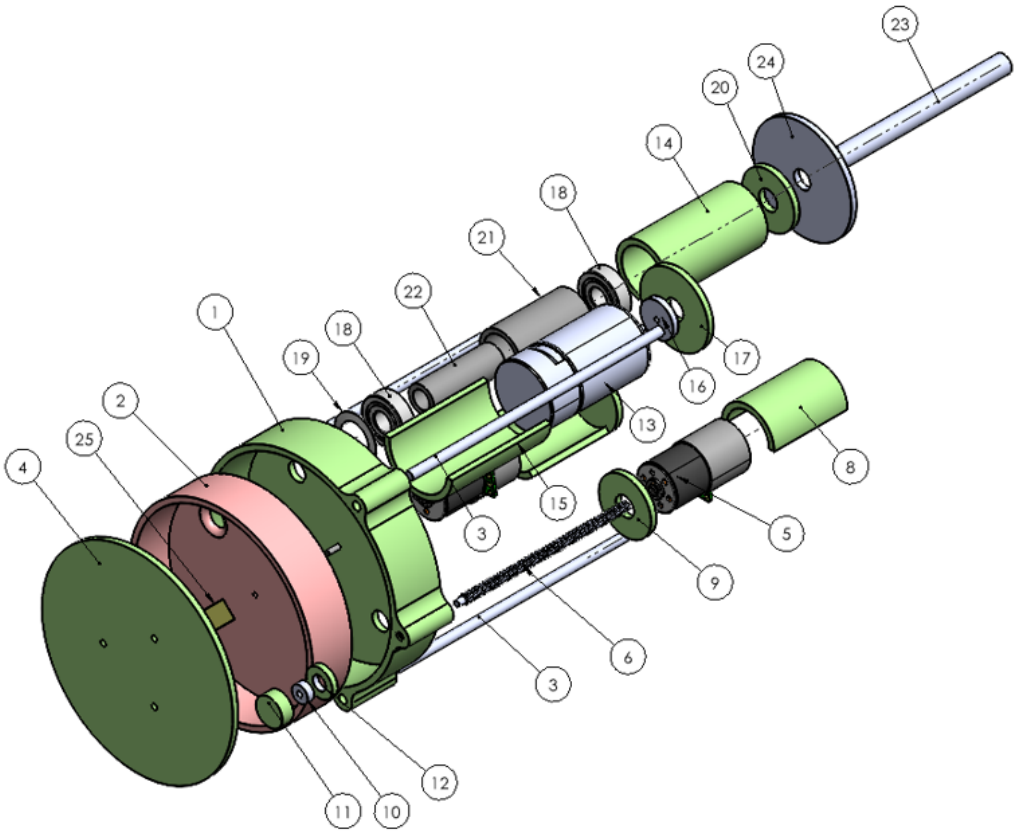

(a) Exploded view of the SSA (1/2).

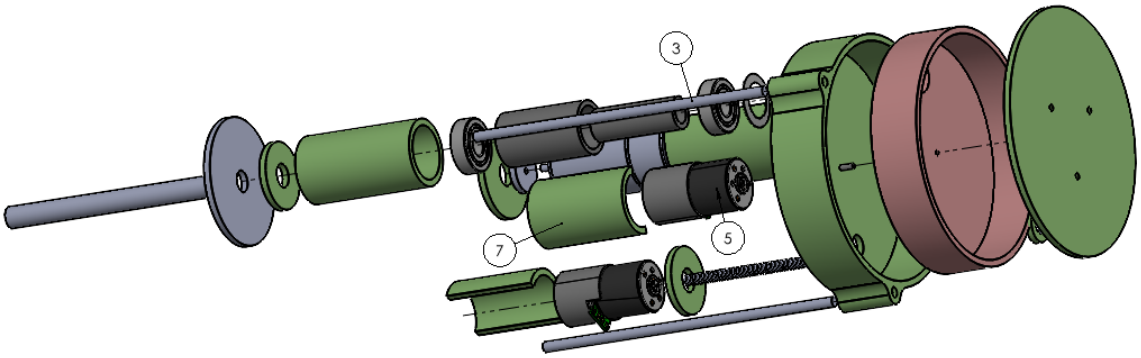

(b) Exploded view of the SSA (2/2).

Figure 3.20: Exploded views of the Surface Sample Analyzer with components labels.

A sectional view of the enclosed vertical screw conveyor is shown in Figure 3.21 to display how it has been preliminarily designed.

Figure 3.21: Sectional view of the enclosed screw conveyor.

3.2.2. Mechanisms design

The components belonging to the three Surface Sample Analyzer mechanisms are going to be designed considering their dimensions constrained by the fixed 1U size of the whole Surface Sample Analyzer. The external structure of the SSA has been assumed made of aluminum ISO AL 99.5 and has been preliminarily designed with 2 mm thicknesses [58]. Eventually, the components design has the scope of leading to the choice of COTS products when possible.

Selector rotation mechanism design

The design of the selector rotation mechanism components has been developed focusing on the friction torque generated during the selector rotation. The friction torque is caused by three main contributes:

- P: the pressure inside the chamber which is the one reached thanks to the pressure/depression valve. This pressure has been hypothesized as uniformly distributed and constant in each point of selector internal surfaces as shown in Figure 3.22.

- Fc: the centrifugal force due to the uniform circular motion of the selector. Notice that for very low angular speeds this contribution can be negligible.
- Fg: the weight force of the selector. This has been neglected since on Deimos the acceleration of gravity is very low, $g = 0.003$ m/s^2.

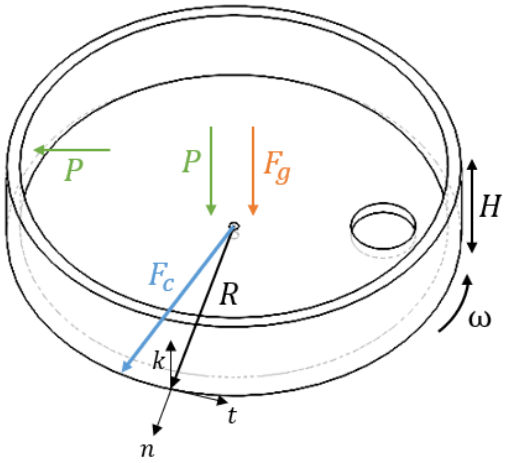

Figure 3.22: Forces acting on the selector.

The friction force, and consequently the friction torque, acting between the external surfaces of the selector and the internal ones of the external shell has been investigated recalling the definition of friction force:

$$F_F = \mu F_N \tag{3.18}$$

where F_N is the resultant of the forces acting normal to the surface.
The friction torque acting on the lateral surface of the selector results from the contributions of the pressure and the centrifugal force as they both act perpendicularly on it. This can be noticed from Figure 3.22 and leads to the following expression:

$$\boldsymbol{T_{F_L}} = \mu(PA_L + Fc)\boldsymbol{t} \wedge R\boldsymbol{n} = -\mu(P2\pi R^2 H + M\omega^2 R^2)\boldsymbol{k} \tag{3.19}$$

While, referring again to Figure 3.22, the friction torque acting on the base of the selector derives only from the contribution of the pressure because the centrifugal force acts parallel on it:

$$\boldsymbol{T_{F_B}} = \int_0^R \mu P \Delta A_B \boldsymbol{t} \wedge R\boldsymbol{n} = -\mu P 2\pi \frac{R^3}{3}\boldsymbol{k} \tag{3.20}$$

The total friction torque has been derived from Equation 3.19 and Equation 3.20 as

follows:

$$\boldsymbol{T_{F_{TOT}}} = \boldsymbol{T_{F_L}} + \boldsymbol{T_{F_B}} = -\mu(P2\pi R^2 H + M\omega^2 R^2 + P2\pi\frac{R^3}{3})\boldsymbol{k} \tag{3.21}$$

The evaluated friction torque defines the torque which the motor has to provide in order to allow the relative rotation of the selector with respect to the fixed external shell. In fact, the motor has to provide a torque equal and opposite to the obtained one due to friction contributions. The choice of the motor has been conducted applying a minimum uncertainty factor according to ESA ECSS [59]:

$$T_M = 2 \cdot 3 \cdot T_{F_{TOT}} = \mu(P2\pi R^2 H + M\omega^2 R^2 + P2\pi\frac{R^3}{3}) \tag{3.22}$$

where T_M is the torque provided by the stepper motor.
The reduced size of the Sample Surface Analyzer represents a constraint for the length of the motor which can be housed inside it. The different stepper motors which have been taken into consideration thanks to their sizes, from the Faulhaber online catalog [25], are listed in Table 3.6 with their dimensions: diameter d_M and length L_M.

Motor	$\boldsymbol{d_M}$ **[mm]**	$\boldsymbol{L_M}$ **[mm]**
DM0620	6	9.5
AM0820	8	13.8
AM1020	10	15.9
DM1220	12	17.6
AM1524	15	16.4
AM2224	22	27.7
AM2224R3	22	30.9

Table 3.6: Dimensions of suitable motors [24][19][20][21][27][28][22].

In Figure 3.23 are reported the motor curves of suitable stepper motors listed in Table 3.6.

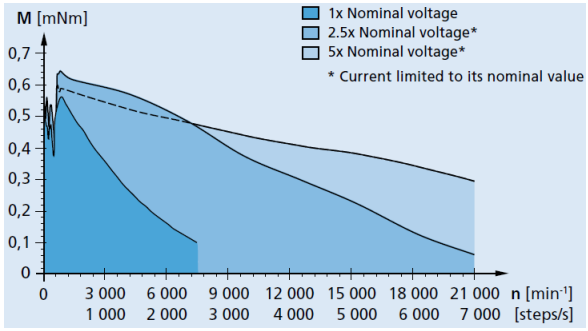

(a) DM0620 operation areas [24].

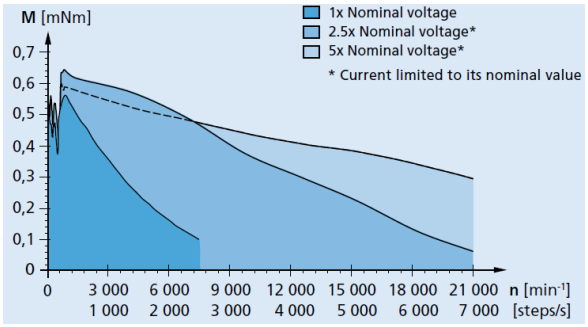

(b) AM0820 operation areas [19].

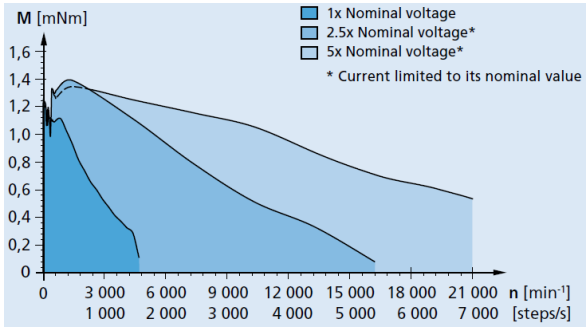

(c) AM1020 operation areas [20].

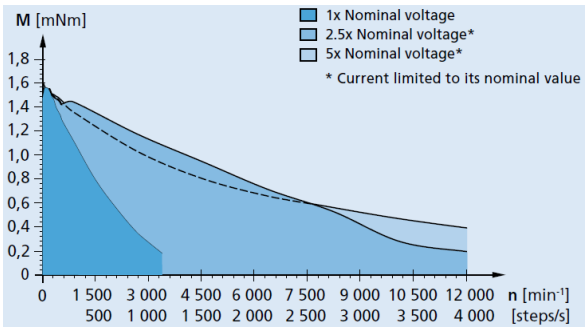

(d) DM1220 operation areas [21].

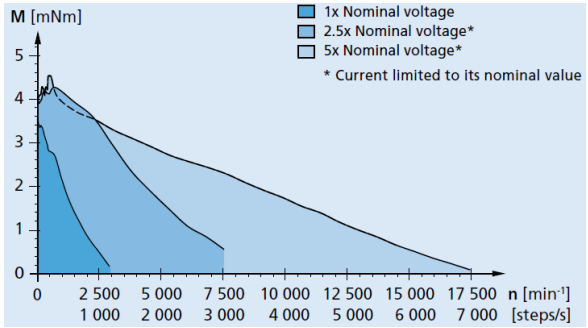

(e) AM1524 operation areas [27].

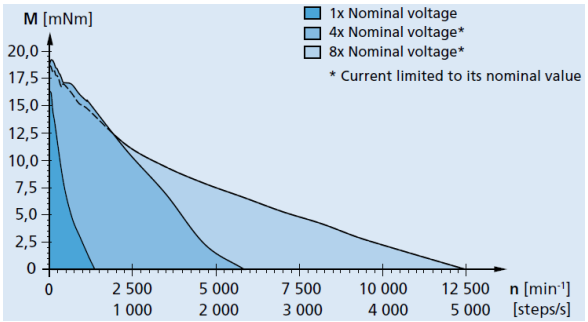

(f) AM2224 operation areas [28].

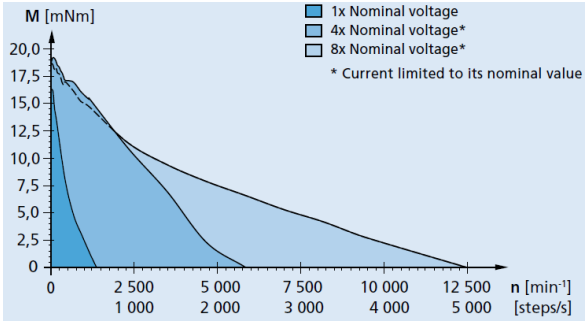

(g) AM2224R3 operation areas [22].

Figure 3.23: Operation areas of suitable motors - *Courtesy of Faulhaber*.

As can be noticed from Figure 3.23, all the available stepper motors are capable of working at high angular velocities which is not a requirement for the selector rotation mechanism. Thus, the maximum angular velocity which each motor can reach has not been considered as a relevant factor in the selection of the stepper motor.
The list of suitable stepper motors has been further reduced to have a motor with a TRL $\geq$ 3, which mean having an already space proven item, and compatible with an encoder with the same TRL. According to this, the stepper motors AM1524 and AM0820 have turned out to be two possible candidates. Moreover, these two stepper motors have been chosen in their configuration equipped with two preloaded ball bearings (RC) to be suitable for vacuum/low temperature [19][27] and to withstand the mechanical environment during launch and throughout the mission [59].
The possible couples of stepper motor and encoder are listed in Table 3.7.

Motor + Encoder	d_{M+E} **[mm]**	L_{M+E} **[mm]**	L_{CABLES} **[mm]**
AM0820RC+IEM3-1024	8	24.1	80 (not adjustable)
AM1524RC+AE23B8-01	16	28	adjustable

Table 3.7: Dimensions of stepper motors coupled with respective encoders [23][25].

As can be noticed from Table 3.7, the first couple has a too long not adjustable length of cables. For this reason the second couple, AM1524RC+AE23B8-01, has been chosen. Furthermore, the encoder has been chosen with the -01 option: PTFE cables (instead of PVC) for out gassing reasons [27].
Having identified a suitable stepper motor, the goal is to define at which pressure ranges the depression valve has to work in order to allow the selector rotation against the friction torque:

$$P = \frac{T_M}{2 \cdot 3 \cdot \mu(2\pi R^2 H + M\omega^2 R^2 + 2\pi\frac{R^3}{3})} \tag{3.23}$$

The pressure values P, at which the valve has to operate, have been evaluated considering the following inputs:

- μ: varying between 0.1 and 2.2. This because different materials which are usually exploited as sealants in space applications have been investigated[3], and their specific friction coefficients are reported in Table 3.8, Table 3.9 and Table 3.10. An important note is about the fact that due to a lack of specific friction coefficients

[3]Materials having fair or limited space applications have been excluded.

for each material, the friction coefficients have been associated to materials focusing on their type and composition reported in [58]. Moreover, another relevant aspect for the identification of the sealants friction coefficients has been the fact that the external shell of the experimental chamber has been assumed to be made of aluminum, specifically ISO AL 99.5, in order to be light and resistant to corrosion and stress corrosion [58].

Rubbers and elastomers	
Material	**μ [-]**
VHDS	$0.5 - 2.2$
Viton B910	$0.25 - 0.3$

Table 3.8: Rubbers and elastomers friction coefficients [3][50][32][65].

Potting compounds, sealants and foams	
Material	**μ [-]**
CV-1142	$0.9 - 1.1$
CV-2566	$0.8 - 1.7$
D.C. 6-1104	$0.5 - 2.2$
RTU 566	$0.9 - 1.1$

Table 3.9: Potting compounds, sealants and foams friction coefficients [30][35][3][50][32].

Thermoplastics	
Material	**μ [-]**
PTFE	$0.16 - 0.25$

Table 3.10: Thermoplastics friction coefficients [5][7].

- R: varying between 25 and 45 mm due to size constraints on the selector radius.
- H: varying between 10 and 30 mm due to size constraints on the selector height.
- ω: about 15 rpm. Since when the selector rotates from feeding to neutral configuration has to cover 90° and then the same angle has to be covered from neutral to

discharge position, no high angular velocities have been considered. For this reason, the contribution of friction torque caused by the centrifugal force is quite absent.

- M: has been supposed to be the selector mass considering PTFE density which is the material with the higher density among the others reported above, as can be noticed from [58], even though up to now the effective type of selector material is unknown. The selector volume has been computed considering the aforementioned values of radius and height, R and H respectively, and assuming 2 mm of thickness. As a consequence of the chosen ω, the mass contribution is quite negligible.
- T_M: varying between 0.5 and 3 mNm. These are all the possible torque values which AM1524RC can provide considering a maximum angular velocity of 250 rpm as can be seen from 3.23e.

Different isolines representing different pressure values for different selector sizes, different friction coefficients and available motor torques have been shown plotting the obtained results. As can be expected:

- For constant μ and T_M, increasing R and H, P decreases. This can be noticed in each subplot of Figure 3.24 and Figure 3.25.
- For constant T_M, R and H, increasing μ, P decreases. This can be noticed looking at Figure 3.24.
- For constant μ, R and H, increasing T_M, P increases. This can be noticed looking at Figure 3.25.

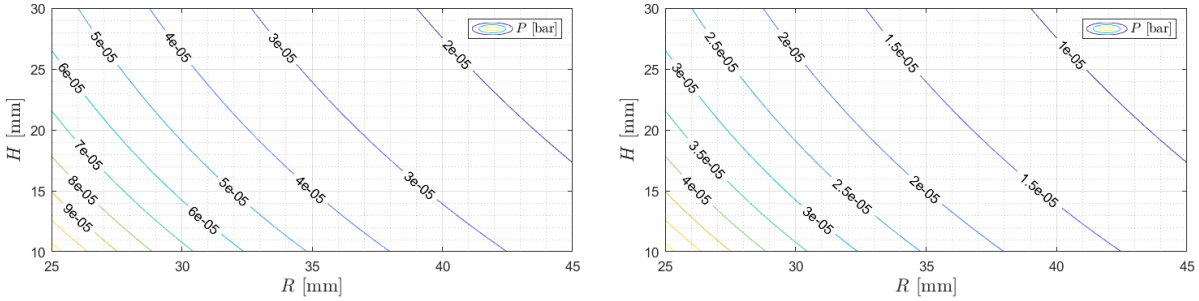

(a) $T_M = 0.5$ Nmm, $\mu = 0.1$.

(b) $T_M = 0.5$ Nmm, $\mu = 0.2$.

Figure 3.24: Pressure at constant motor torque and variable friction coefficient.

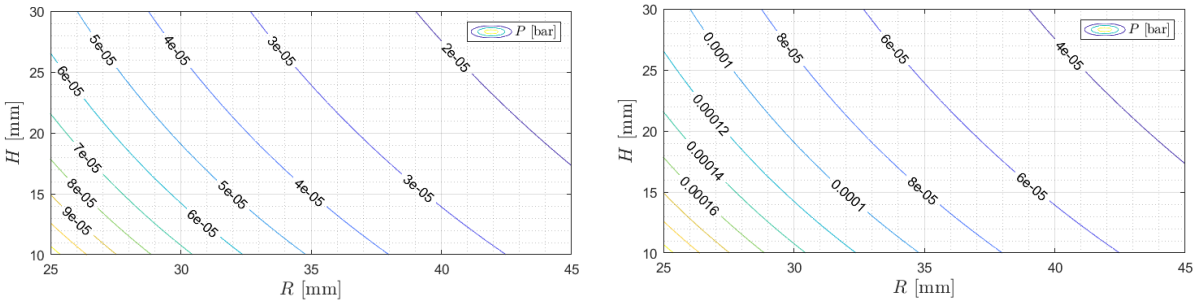

(a) $T_M = 0.5$ Nmm, $\mu = 0.1$.

(b) $T_M = 1$ Nmm, $\mu = 0.1$.

Figure 3.25: Pressure at constant friction coefficient and variable motor torque.

The proper selector material has been selected taking into account two aspects. The first one refers to the out gassing requirements, in particular RML $< 1\%$ and CVCM $< 0.1\%$ according to ESA ECSS [57]. The other one involves the thermal expansion coefficient which has to be as similar as possible to the one of the material of the external shell: ISO Al 99.5 (CTE = 24x10^{-6}°C^{-1}). The CTE of the investigated materials are reported in Table 3.11, Table 3.12 and Table 3.13. As for the friction coefficients, the missing CTE in [58] have been chosen to refer to material type and composition.

Rubbers and elastomers	
Material	**CTE [10^{-6}°C^{-1}]**
VHDS	342
Viton B910	160

Table 3.11: Rubbers and elastomers thermal expansion coefficients [13][65].

Potting compounds, sealants and foams	
Material	**CTE [10^{-6}°C^{-1}]**
CV-1142	200
CV-2566	310
D.C. 6-1104	387
RTU 566	200

Table 3.12: Potting compounds, sealants and foams thermal expansion coefficient [58][29].

Thermoplastics	
Material	**CTE [10^{-6}°C^{-1}]**
PTFE	100

Table 3.13: Thermoplastics thermal expansion coefficient [58].

PTFE results to be the best material for both thermal expansion coefficient, as shown in Table 3.11, Table 3.12, Table 3.10, and out gassing properties, as reported in [58].
The evaluated pressure ranges, at which the chamber has to be depressurized, considering selector dimensions as $R = 35$ mm and $H = 15$ mm, selector material as PTFE and ω= 15 rpm at the aforementioned different values of T_M are depicted in Figure 3.26 and Figure 3.27 and summarized in Table 3.14.

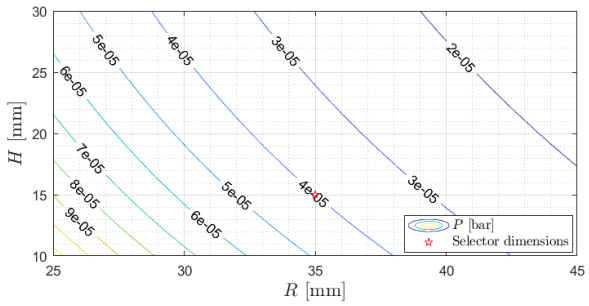

(a) $T_M = 0.5$ Nmm, $\mu = 0.1$.

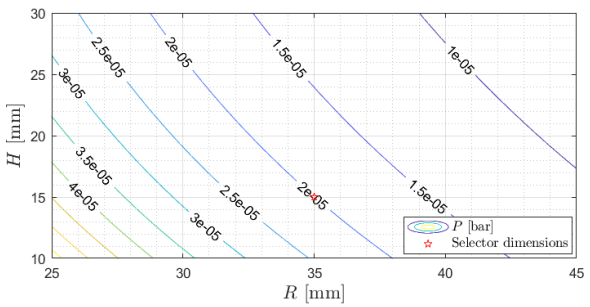

(b) $T_M = 0.5$ Nmm, $\mu = 0.2$.

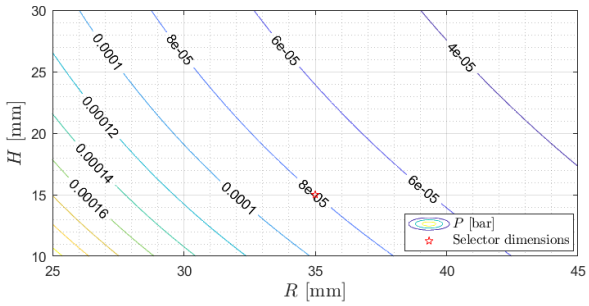

(c) $T_M = 1$ Nmm, $\mu = 0.1$.

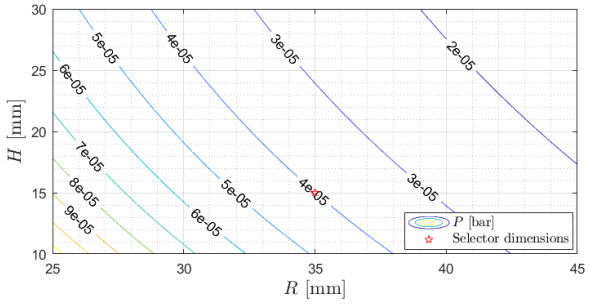

(d) $T_M = 1$ Nmm, $\mu = 0.2$.

Figure 3.26: Pressure considering different motor torque and PTFE friction coefficient (1/2).

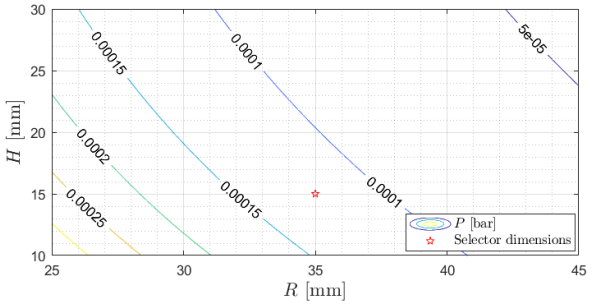

(e) $T_M = 1.5$ Nmm, $\mu = 0.1$.

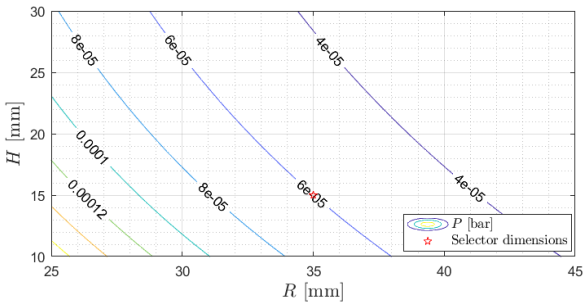

(f) $T_M = 1.5$ Nmm, $\mu = 0.2$.

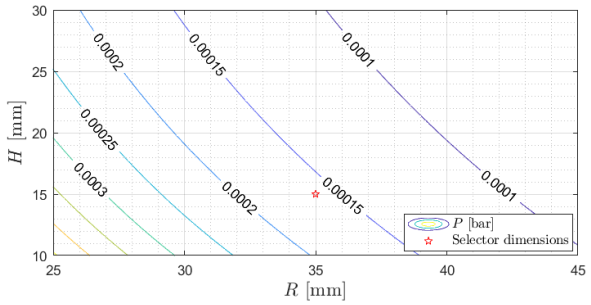

(g) $T_M = 2$ Nmm, $\mu = 0.1$.

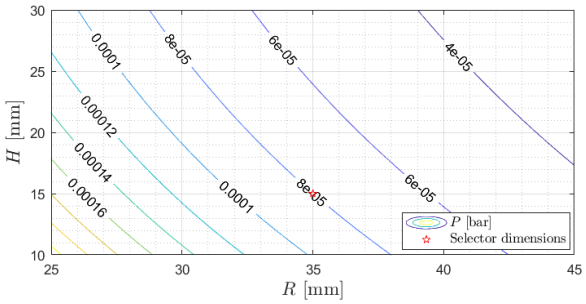

(h) $T_M = 2$ Nmm, $\mu = 0.2$.

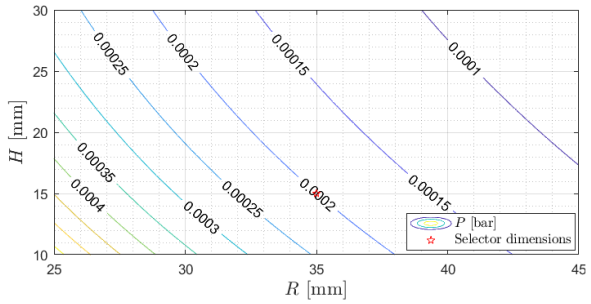

(i) $T_M = 2.5$ Nmm, $\mu = 0.1$.

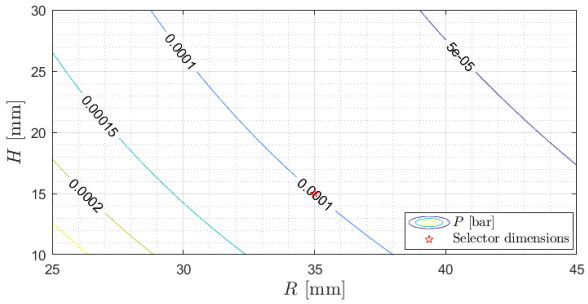

(l) $T_M = 2.5$ Nmm, $\mu = 0.2$.

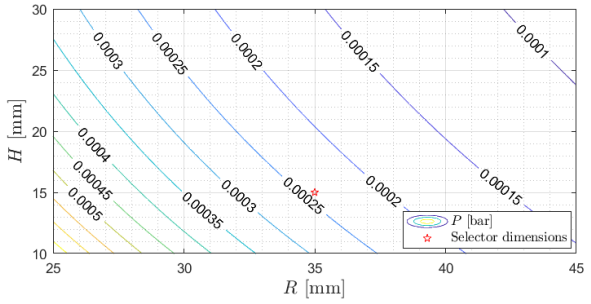

(m) $T_M = 3$ Nmm, $\mu = 0.1$.

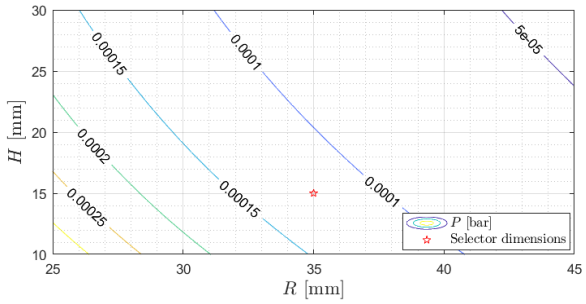

(n) $T_M = 3$ Nmm, $\mu = 0.2$.

Figure 3.27: Pressure considering different motor torque and PTFE friction coefficient (2/2).

T_M [Nmm]	P [bar]
0.5	$2x10^{-5}$–$4x10^{-5}$
1	$4x10^{-5}$–$8x10^{-5}$
1.5	$6x10^{-5}$–0.00012
2	$8x10^{-5}$–0.00016
2.5	0.0001-0.0002
3	0.000125-0.00024

Table 3.14: Pressure inside the chamber at different motor torques.

In order to reduce the difference between the chamber pressurized condition during analysis around 1 atm and when its depressurized, the last couple of values in Table 3.14 have been chosen. The operating point of stepper motor AM1524 is depicted in Figure 3.28.

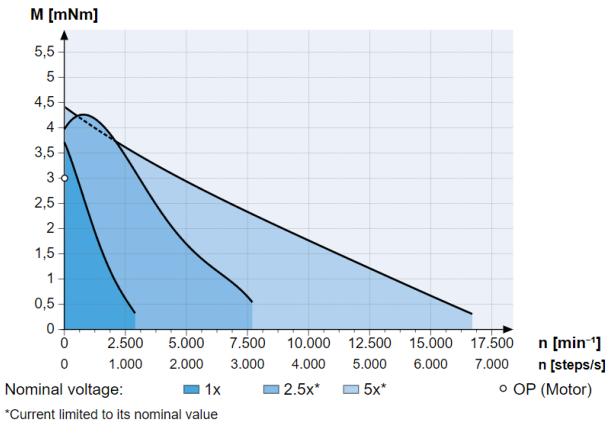

Figure 3.28: AM1524 OP [27] - *Courtesy of Faulhaber.*

The chosen selector dimensions, especially the assumed thickness, have been identified as admissible values from a manufacturing point of view, but they have to be confirmed through mechanical analysis. Moreover, the sealing capability of PTFE selector has to be tested in order to ensure that nothing can enter of exit through it during the soil samples analysis. As already pointed out, the selector has been preliminarily designed as an open on top cylinder with a hole on the base. This to allow the entrance or the exit of the samples soil. Thus, to permit a safe soil acquisition, the hole has been designed with a diameter of 6.35 mm, equal to the external diameter of the preliminarily designed Surface Sample Analyzer screw conveyor.
As already pointed out, a driver able of reducing the step size of the chosen stepper

motor, AM1524RC, through micro-stepping could be useful to ensure a smooth selector rotation at the selected angular velocity of 15 rpm. Also, it's fundamental to have a driver/controller to guide and control the stepper motor motion. For this reason, the 1-axis driver/controller MCST 3601, compatible with AM1524RC stepper motor, has been exploited even though it has to be tested for space application. The identified driver/controller presents compatible dimensions with respect to the 1U external structure of the SSA. MCST 3601 results to be a sort of rectangular solid and its dimensions are summarized in Table 3.15.

Base [mmxmm]	**Height [mm]**
68x47.5	13

Table 3.15: MCST 3601 dimensions [26].

Once the suitable stepper motor, coupled with its encoder, has been identified, a cylindrical shaped case housing both of them has been preliminarily designed taking into account the diameter and length obtained by the coupling of the two, reported in Table 3.7 and assuming thicknesses equal to 2 mm. Moreover, the case has been considered made of the same material of which is made the external shell of the experimental chamber, ISO AL 99.5.

Drill rotation mechanism design

The rotation of the drill bit has been ensured by the exploitation of single stage spur gears driven by a stepper motor. Moreover, the independent rotation of the drill bit with respect to the external shell of the experimental chamber has been permitted by rolling bearings.

A brief dissertation about how the bearings have been chosen and about their features and characteristic dimensions is fundamental before proceeding with the spur gears design. The selection of bearings type has been lead by the application in which the bearings are involved. In fact, bearings for space applications have to be made of materials resistant to the extreme mission environment, such as vacuum, high temperatures and corrosion. These conditions allow only the use of bearings with solid lubricants while usually oil or grease lubricants are employed. Among all the available bearings types from SPACEA online catalog [48], developed by NSK, the ones belonging to YS high temperature bearings with spacer joints have been selected. This family of bearings has been chosen thanks to its specifications, reported in 3.29b and operating features listed below.

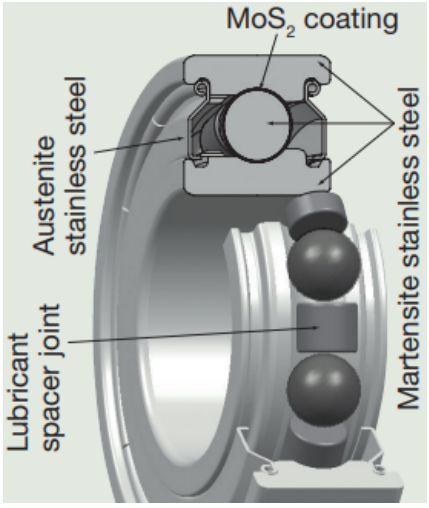

(a) YS high temperature bearings drawing - *Courtesy of NSK.*

Components	Material
Outer/Inner rings	Martensite stainless steel
Balls	Martensite stainless steel and MoS_2 coating
Cage	Lubricating spacer joints (sintered alloy)
Lubricant	MoS_2 soil lubricant
Shields	Austenite stainless steel

(b) YS high temperature bearings materials.

Figure 3.29: YS high temperature bearings specifications [48].

The operating features of YS high temperature bearings with spacer joints [48]:

- Grease-free, MoS2 solid lubrication.
- Usable in vacuum up to 10^{-8} Pa and temperature up to 350°C.
- Operating life is 10 times longer than conventional high-temperature solid-lubricant bearings.

Another important aspect for the bearings choice has been the dimension of the external diameter of the drill bit which has to be equal to the internal diameter of the bearing to ensure a correct working of the latter. As discussed in subsubsection 3.1.2, the drill bit has been preliminarily designed as an enclosed screw conveyor with the external diameter equal to 6.35 mm. As a consequence, bearings named R4LZZC3-HMST4, belonging to YS high temperature bearings with spacer joints family, and with dimensions reported in

Table 3.16 have been identified. The bearing dimensions symbols refer to Figure 3.30.

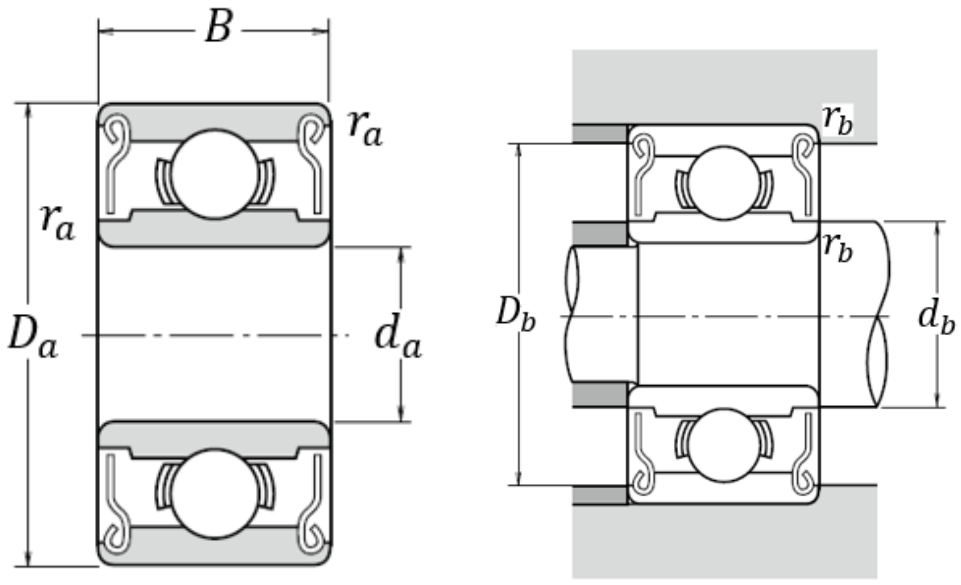

(a) Drawing of bearing in free configuration.

(b) Drawing of bearing in mounted configuration.

Figure 3.30: Bearing drawing in its free and mounted configuration [49] - *Courtesy of NSK*.

d_a [mm]	D_a [mm]	B [mm]	r_a min [mm]	d_b max [mm]	D_b min [mm]	r_b max [mm]
6.350	15.875	4.978	0.3	8.4	13.8	0.3

Table 3.16: Bearing dimensions when free and when mounted [49].

The basic load rating C_r and the basic static load rating C_{0r} of bearing named R4LZZC3-HMST4 are reported in Table 3.17.

C_r [N]	C_{0r} [N]
1258	493

Table 3.17: Basic load rating and basic static load rating of R4LZZC3-HMST4 [48].

Once the dimensions and loads rating of bearings involved in the mechanism were known, the design of single stage spur gears have developed as described in [56]. The torque and

angular speed values required by the drill, deriving from subsubsection 3.1.2, are reported in Table 3.18. These parameters have led the design of the drill rotation mechanism.

n_L [rpm]	T_L [Nmm]
50	50

Table 3.18: Drill motor design parameters

The first thing to consider, while designing the power transmission devices is the fact that, only a part of the power provided by the motor reaches the load due to spur gears efficiency η as follows:

$$\eta = \frac{P_L}{P_M} = \frac{T_L \omega_L}{T_M \omega_M} \tag{3.24}$$

where:

- P_L: the required power at load.
- P_M: power provided by the stepper motor.
- T_L: the required torque at load, reported in Table 3.18.
- $\omega_L = 2\pi n_L$: the required angular velocity at load, where n_L is reported in Table 3.18.
- T_M: the required torque at motor.
- $\omega_M = 2\pi n_M$: the required angular velocity at motor.

The spur gear ratio u is stated as:

$$u = \frac{\omega_M}{\omega_L} \tag{3.25}$$

Thus, Equation 3.24 and Equation 3.25 leads to the torque and angular velocity at motor as follows:

$$T_M = \frac{T_L}{u\eta} \quad \omega_M = u\omega_L \tag{3.26}$$

where:

- u: varying between 1:1 and 1:10. This because gear ratio values up to 1:10 are suitable for single stage spur gears while double stage spur gears are implied when a gear ratio higher than 1:12 is required.
- η: 95%. This is due to non-perfect alignment of the parallel axis spur gears and friction contributions between gears [56].

The following observation has lead to a preliminary definition of only few suitable stepper motors among the available ones presenting compatible dimensions with the 1U size of the Surface Sample Analyzer. Considering a maximum admissible value of gear ratio of 1:10 can be translated into the need of having a motor capable of working at $T_M = 5.3$ mNm and $n_M = 500$ rpm. Only the stepper motor AM2224 and AM2224, from the available motors list in Table 3.6 are able to satisfy the aforementioned requirements as can be noticed looking at Figure 3.23.
Single stage spur gears have been designed exploiting synthetic stress factors, as described in [8], which are useful to have a preliminary idea about gears design. These factors are simple indicators which depends on only few parameters and from which the gears dimensions can be obtained depending on the power transmitted by gears, the gear ratio and the material of gears. Moreover, synthetic stress factors have limit values, depending on the chosen material, which gives information about the project feasibility.
The synthetic stress factors are:

- Tooth root synthetic factor U_L, and it deals with the bending strength:

$$U_L = \frac{F_t}{bm} \tag{3.27}$$

  where:

  - $F_t = F_{t_M} = F_{t_L} = \frac{2T_M}{d_{p_1}} = \frac{2T_L}{\eta d_{p_2}}$: tangential force at teeth contact.
  - b: wheel band width.
  - m: module.

- Surface synthetic factor K, and it deals with the contact fatigue strength:

$$K = \frac{F_t}{dp_1 b}\left(1 + \frac{z_1}{z_2}\right) = \frac{F_t}{dp_1 b}\left(\frac{u+1}{u}\right) \tag{3.28}$$

  where:

  - dp_1: pinion reference diameter.
  - z_1, z_2: pinion and gear teeth number respectively.

The design of single stage spur gears with synthetic stress factors has been developed going through the following steps:

1. Definition of the torque and angular speed required by the load, T_L and ω_L.
2. Definition of the efficiency of spur gears η.

3. Choice of a guess value for single stage spur gears ratio u up to 10:1, according the reason explained above.

4. Computation of the torque and angular velocities which have to be provided by the stepper motor, T_M and ω_M as stated in Equation 3.26.

5. Definition of the minimum inter-axis of spur gears a. This value is dictated by the external diameter of the case where the chosen stepper motor coupled with its encoder is housed and the external diameter of the case containing the two bearings. In fact, a minimum distance between two parallel axis of the drill motor and the drill itself is required to avoid interference between the two aforementioned cases. For this reason, the bearings choice as well as a preliminary study about a suitable stepper motor have to precede the spur gears design or have to be performed together with it.

6. Choice of the guess values of the two synthetic stress factors U_L and K respecting their limit values indicating them as U_L^* and K^*.

7. Computation of the reference diameters of pinion and gear, dp_1 and dp_2 respectively, as follows:
$$dp_1 = \frac{2a}{u} \quad dp_2 = u dp_1 \tag{3.29}$$

8. Computation of the band width b from Equation 3.28.
If $b \geq b_{min}$ it can be taken, otherwise it has to be replaced with b_{min}.
$$b = \frac{1}{K^*}\frac{2T_M}{dp_1^2}\left(\frac{u+1}{u}\right) \quad b_{min} = \frac{dp_1}{10} \tag{3.30}$$

9. Computation of the module m from Equation 3.27 as follows:
$$m = \frac{2T_M}{dp_1 b U_L^*} \tag{3.31}$$
The obtained module must be as near as possible to one of the standard module values.

10. Computation of the teeth number of pinion and gear, z_1 and z_2 respectively.
$$z_1 = \frac{dp_1}{m} \quad z_2 = u z_1 \tag{3.32}$$

- The teeth number has to be an entire value.

- z_1 and z_2 are preferred to be relative prime numbers.
- $z_1 \geq z_{min}$ is the minimum number of teeth of pinion free of undercutting.

$$z_{min} = \frac{2}{\sin^2 \alpha_P} \tag{3.33}$$

where α_P is the pressure angle and usually $\alpha_P = 20°$, hence, $z_{min} = 17$.

The aforementioned steps have been repeated changing the guess values cited in item 3 and item 6 until:

- Manufacturer feasibility of pinion and gear in terms of dp_1 and dp_2 has been obtained.
- The value of module m was very similar to one among the standardized module values.
- $z_1 \geq 17$.

Eventually, the output of the steps procedure, reported above, have lead to the computation of the missing quantities for the complete spur gears design as stated:

$$h_a = m \quad h_f = 1.25m \quad h = h_a + h_f = 2.25m \tag{3.34}$$

$$p_f = 0.2m \quad p = \pi m \quad p_b = p \cos \alpha_P = \pi m \cos \alpha_P \tag{3.35}$$

$$d_{b_i} = m z_i \cos \alpha_P \quad d_{a_i} = (z_i + 2)m \quad d_{f_i} = (z_i - 2.5)m \tag{3.36}$$

$$g_{\alpha_P} = \tfrac{1}{2} m \left[\sqrt{(z_1 + 2)^2 - (z_1 \cos \alpha_P)^2} + \sqrt{(z_2 + 2)^2 - (z_2 \cos \alpha_P)^2} - (z_1 + z_2) \sin \alpha_P \right] \tag{3.37}$$

$$\epsilon_{\alpha_P} = \tfrac{g_{\alpha_P}}{p_b} = \tfrac{1}{2\pi \cos \alpha_P} \left[\sqrt{(z_1 + 2)^2 - (z_1 \cos \alpha_P)^2} + \sqrt{(z_2 + 2)^2 - (z_2 \cos \alpha_P)^2} - (z_1 + z_2) \sin \alpha_P \right] \tag{3.38}$$

For a regular gearing, hence, a continuous and not intermittent gearing, ϵ_{α_P} must be greater than 1 and it's usually between 1 and 2.

To design single stage spur gears of SSA, the imposed limit values of U_L and K are reported in Table 3.19.

U_L [MPa]	K [MPa]
50 - 70	2.8 - 5

Table 3.19: Limit values of synthetic stress factors U_L and K [8].

The reasons why these specific values have been taken into account are justified below and refer to Figure 3.31.

- Indicative values of U_L range from 50 up to 70 MPa when surface hardened materials are considered.
- Guide values which can be assumed by K are summarized in Figure 3.31. In space applications it's common to employ stainless steels. Among these, only martensitic stainless steels can be hardened with induction which have lead to consider K varying between 2.8 and 5 MPa.

Thus, from the aforementioned observations, spur gears have been considered made of martensitic stainless steel which has been hardened with induction and which passed stress corrosion cracking test. The latter qualifies the material specifically for space applications.

Mat. pignone	Mat. ruota	Finitura pignone	Finitura ruota	K [MPa]	UL [MPa]
Cementato HRC 62	Cementato HRC 62	rettifica	rettifica	5.6-10	50-70
Cementato HRC 62	Temprato HRC 55	rettifica	fresatura	3.6-6.3	50-70
Temprato HRC 55	Temprato HRC 55	fresatura	fresatura	2.8-5	50-70
Cementato HRC 62	Cementato HRC 62	rettifica	rettifica	2-6.3	50-70

Figure 3.31: Indicative values of K and U_L for different materials [8].

Then, the values of standard module according to DIN-780 Part 1 [10], reported in Fig-

ure 3.32[4], and the input values, listed in Table 3.20, have been exploited.
These values of module and inputs have been set, after different iterations of the design process described above, since they allow to achieve the best results and consequently the aforementioned goals, about manufacturer feasibility, module and minimum number of pinion teeth, which permit to design spur gears in accordance with the standards.

Modules m in mm	
Series I	Series II
0,05	
	0,055
0,06	
	0,07
0,08	
	0,09
0,1	
	0,11
0,12	
	0,14
0,16	
	0,18
0,2	
	0,22
0,25	
	0,28
0,3	
	0,35
0,4	
	0,45

Modules m in mm	
Series I	Series II
0,5	
	0,55
0,6	
	0,65
0,7	
	0,75
0,8	
	0,85
0,9	
	0,95
1	
	1,125
1,25	
	1,375
1,5	
	1,75
2	
	2,25
2,5	
	2,75

Modules m in mm	
Series I	Series II
3	
	(3,25)
	3,5
	(3,75)
4	
	(4,25)
	4,5
	(4,75)
5	
	(5,25)
	5,5
	(5,75)
6	
	(6,5)
	7
8	
	9
10	
	11
12	

Modules m in mm	
Series I	Series II
	14
16	
	18
20	
	22
25	
	(27)
	28
	(30)
32	
	36
	(39)
40	
	(42)
	45
50	
	55
60	
	70

Figure 3.32: Standard module values [10] - *Courtesy of DIN.*

T_L [Nmm]	n_L [rpm]	u [-]	η [%]	T_M [Nmm]	n_M [rpm]	a [mm]	U_L^* [MPa]	K^* [MPa]	α_P [deg]
50	50	3	95	17.5	150	25	55	3	20

Table 3.20: Inputs of single stage spur gears design.

Having performed rounding and adjustments, the power transmission chain results to be characterized by the parameters reported in Table 3.21, which have been defined by spur gears design. The results refer to features reported in Figure 3.33.

[4]The modules of series I should be preferred to the modules of series II. The modules in brackets of series II are intended for special purposes [10].

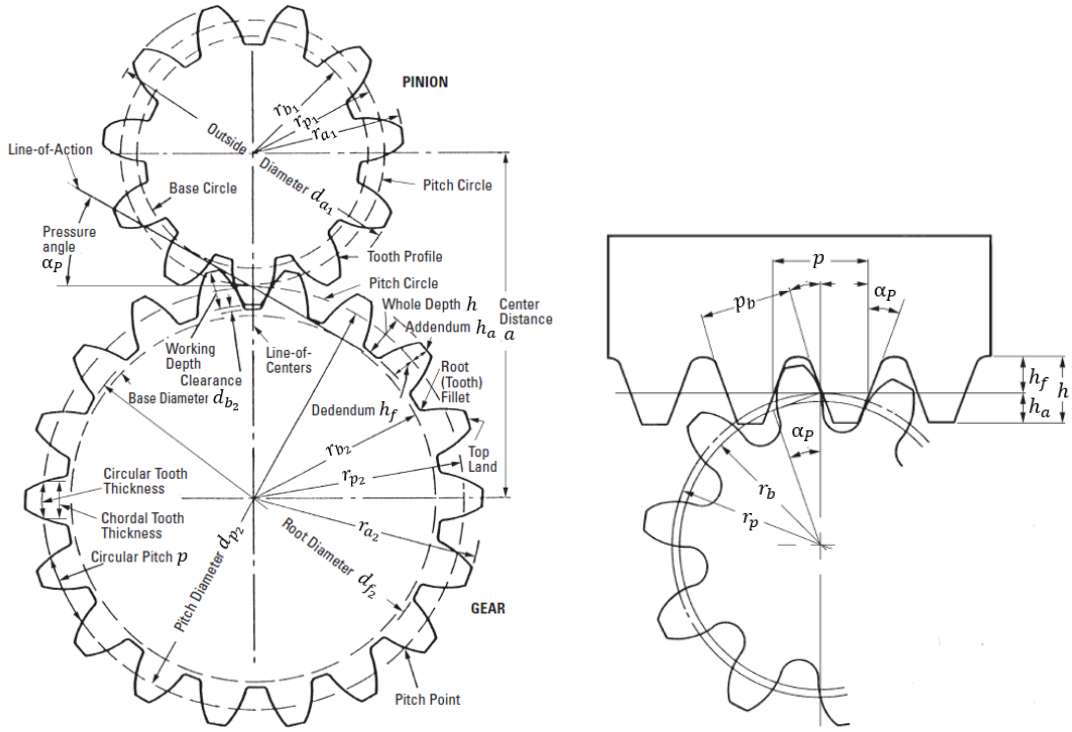

(a) Single stage spur gears drawing.

(b) Gear drawing.

Figure 3.33: Spur gears features [56] - *Courtesy of SDP/SI.*

u_{eff} [-]	a_{eff} [mm]	m_{eff} [mm]	b_{eff} [mm]	$dp_{1_{eff}}$ [mm]	$dp_{2_{eff}}$ [mm]	$z_{1_{eff}}$ [-]	$z_{2_{eff}}$ [-]
3.00	25.03	0.05	1.25	12.50	37.55	250	751

Table 3.21: Outputs of single stage spur gears design.

From parameters in Table 3.21, the parameters reported in Table 3.22 have been computed.

h_a [mm]	h_f [mm]	h [mm]	p [mm]	p_b [mm]	p_f [mm]
0.05	0.063	0.11	0.16	0.15	0.010

(a) Additional outputs of single stage spur gears design (1/2).

d_{b_1} [mm]	d_{b_2} [mm]	d_{a_1} [mm]	d_{a_2} [mm]	d_{f_1} [mm]	d_{f_2} [mm]	g_{α_P} [mm]	ϵ_{α_P} [-]
11.75	35.29	12.60	37.65	12.38	37.43	0.29	1.94

(b) Additional outputs of single stage spur gears design (2/2).

Table 3.22: Additional outputs of single stage spur gears design.

As can be noticed from Table 3.20, a gear ratio equal to 3:1 has been chosen requiring T_M = 17.5 mNm and n_M = 150 rpm. This has been assumed even tough it requires having motors AM2224 or AM2224R3 supplied with higher values of their nominal voltage, as shown in 3.34a and 3.34b. Alternatively, a stepper motor bigger than AM2224 or even AM2224R3 should have been taken in consideration. This couldn't be an option since the motor diameter would have been too big to be placed on the bottom part of the external shell of the experimental chamber and between the other needed components. It's important to remind that the stepper motor allowing the drill rotation will be placed, as already said, on the bottom part of the chamber and with its axis parallel to the drill one. Thus, the stepper motor length, increased by the coupling of the motor with a compatible encoder, has to be such as to enable the translation of the experimental chamber coupled with the drill. In particular, the stepper motor must remain inside the SSA structure for the whole duration of the chamber translation.
There would be also another possibility to avoid the exploitation of AM2224 and AM2224R3 supplied with their non-nominal voltage. The gear ratio u can be incremented up to 10:1 but having a minimum value of the inter-axis a, due to the dimensions of the two admissible stepper motors previously identified, AM2224 and AM2224R3, and the dimensions of selected bearings named R4LZZC3-HMST4, the pinion reference diameter would reach unfeasible or at least difficult value to be manufactured. For the same reason, the standard modules belonging to DIN-780 Part 1 [10] have been investigated as they are lower values with respect to others standardized modules.
Thus, both of the two aforementioned alternatives has resulted to be less advantageous with respect to the exploitation of AM2224 and AM2224R3 supplied with higher voltage with respect to their nominal values. Of course, between AM2224 and AM2224R3, the stepper motor AM2224 has been chosen since it's the smallest one for the same performances as can be noticed from 3.34a and 3.34b.

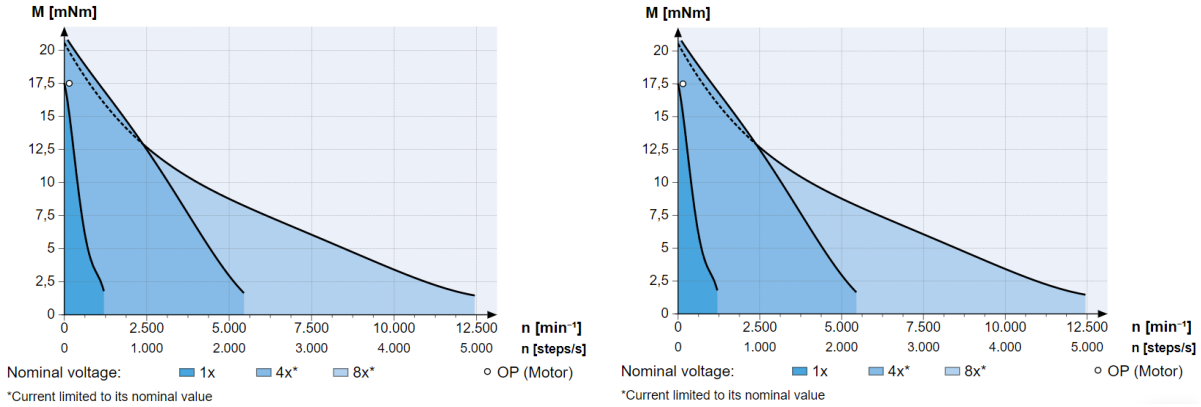

(a) AM2224 OP [28]. (b) AM2224R3 OP [22].

Figure 3.34: Operating point of AM2224 and AM2224R3 - *Courtesy of Faulhaber*.

The chosen stepper motor, AM2224, presents the positive aspects that it can be coupled with an encoder still obtaining compatible dimensions with SSA size constraint, as reported in Table 3.23, and that it is available also in the option AM2224RC equipped with preloaded ball bearings named RC. While, the negative aspect is that both the motor and the encoder don't satisfy the TRL requirement, and they have to be modified for space applications. Moreover, the motion of the selected stepper motor can be controlled through the 1-axis driver/controller MCST 3601. The latter has to be tested for space application because, as the selected stepper motor and encoder, it doesn't fulfill the required TRL.

Motor + Encoder	d_{M+E} **[mm]**	L_{M+E} **[mm]**	L_{CABLES} **[mm]**
AM2224RC+PE22-120	22	38	adjustable

Table 3.23: Dimensions of AM2224RC coupled PE22-120 [17].

As already pointed out, the diameter d_{M+E}, reported in Table 3.23, has contributed to determine the minimum inter-axis a exploited in the spur gears design and reported in Table 3.20.

The pinion and gear tangential and separating force at the gear meshing point, F_{t_M}, F_{s_M} and F_{t_L}, F_{s_L}, have been calculated as follows [44]:

$$F_{t_M} = F_{t_L} = \frac{9550000 P_M}{n_M\left(\frac{dp_1}{2}\right)} = \frac{9550000 P_L}{\eta n_L\left(\frac{dp_2}{2}\right)} \tag{3.39}$$

$$F_{s_M} = F_{s_L} = F_{t_M} \tan \alpha_P \tag{3.40}$$

where:

- $P_M = T_M\omega_M$, $P_L = T_L\omega_L$: transmitted power in kW, with $\omega = 2\pi n$, from Table 3.20.
- n_M, n_L: angular speed at motor and at load respectively, from Table 3.20.
- dp_1, dp_2: pinion and gear reference diameter respectively, from Table 3.20.
- α_P: gear pressure angle, from Table 3.20.

Exploiting the same inputs implied in single stage spur gears design, reported in Table 3.20 and the obtained results reported in Table 3.21, the pinion and gear tangential and separating force at gear meshing point have been obtained. The results are summarized in Table 3.24

$\boldsymbol{F_{t_M} = F_{t_L}}$ [N]	$\boldsymbol{F_{s_M} = F_{s_L}}$ [N]
2.81	1.022

Table 3.24: Pinion and gear tangential and separating force at gear meshing point.

The tangential and separating forces at gear mashing point act as depicted in Figure 3.35.

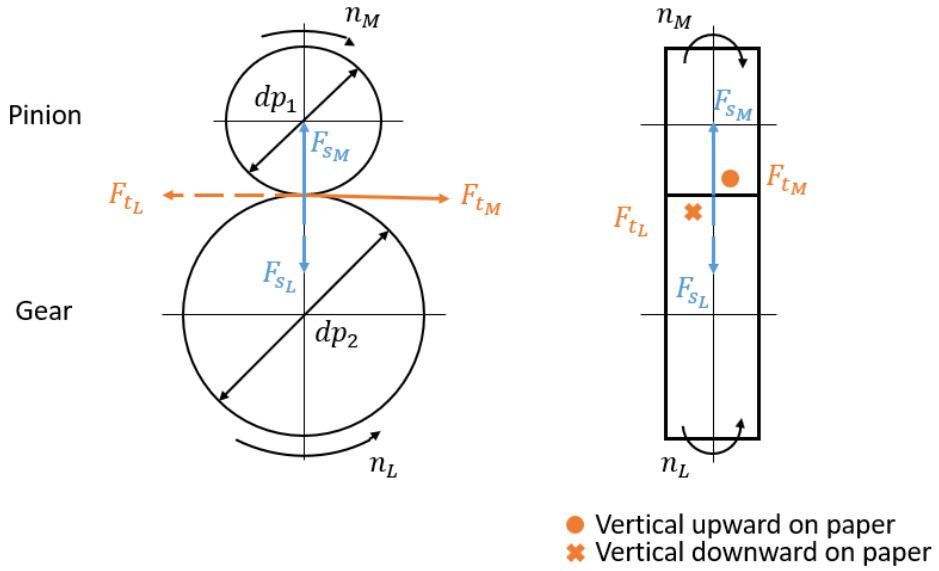

Figure 3.35: Tangential and separating forces at gear meshing point [44] - *Courtesy of NSK*.

The axial and radial loads acting on bearings have been derived from the tangential

and separating forces at gear meshing point as reported in Table 3.25 and referring to Figure 3.36.

Load classification	Bearing A	Bearing B	Bearing C	Bearing D
Radial load from F_t	$F_{t_A} = \frac{dA+dB}{dB} F_{t_M}$	$F_{t_B} = \frac{dA}{dB} F_{t_M}$	$F_{t_C} = \frac{dC+dD}{dD} F_{t_L}$	$F_{t_D} = \frac{dC}{dD} F_{t_L}$
Radial load from F_s	$F_{s_A} = \frac{dA+dB}{dB} F_{s_M}$	$F_{s_B} = \frac{dA}{dB} F_{s_M}$	$F_{s_C} = \frac{dC+dD}{dD} F_{s_L}$	$F_{s_D} = \frac{dC}{dD} F_{s_L}$
Radial load	$F_{r_A} = \sqrt{F_{t_A}^2 + F_{s_A}^2}$	$F_{r_B} = \sqrt{F_{t_B}^2 + F_{s_B}^2}$	$F_{r_C} = \sqrt{F_{t_C}^2 + F_{s_C}^2}$	$F_{r_D} = \sqrt{F_{t_D}^2 + F_{s_D}^2}$
Axial load	$F_{a_A} = 0$	$F_{a_B} = 0$	$F_{a_C} = 0$	$F_{a_D} = 0$

Table 3.25: Radial and axial loads from the tangential and separating forces [44].

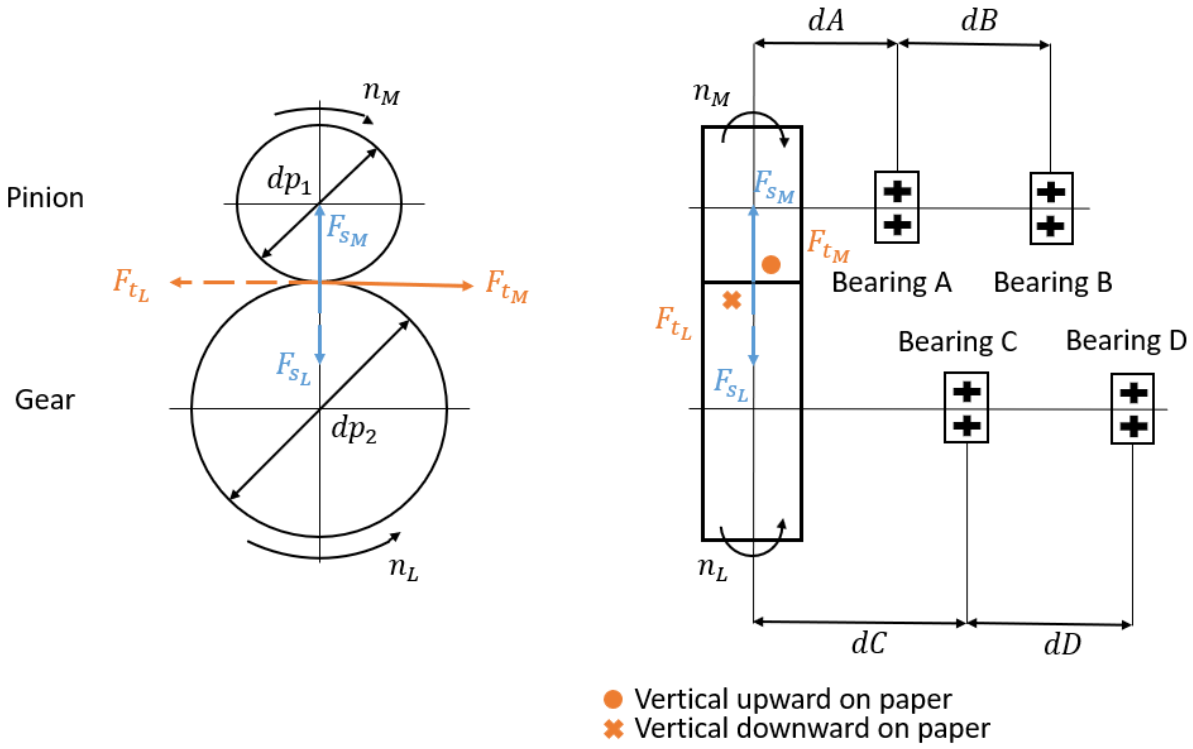

Figure 3.36: Tangential and separating forces at gear meshing point with respect to bearings [44] - *Courtesy of NSK*.

Bearings A and B are RC bearings and are situated on the pinion axis and are housed in the chosen stepper motor AM2224. While, bearings C and D are R4LZZC3-HMST4 bearings and are situated on the gear axis, which is also the same axis of the drill bit. Distances, reported in Table 3.26, between gears and bearings have been considered for the computation of radial and axial loads.

***dA* [mm]**	***dB* [mm]**	***dC* [mm]**	***dD* [mm]**
3	27.7	6	33

Table 3.26: Distances between bearings and spur gears.

Distances reported in Table 3.26 have been chosen as follows:

- dA is a fixed value reported in [28] and depends on how the chosen motor is structured internally.
- dB depends on the motor length since it has been considered that the two bearings A and B, placed inside AM2224, are located to the extremities of the motor case.
- dC has been chosen in order to have aligned bearings named C and A.
- dD has been selected considering that bearing D has one side attached to the external shell of the experimental chamber.

The aforementioned arrangements of bearings C and D, guiding the definition of dC and dD respectively, allow to have these two bearings as far as possible one from the other to improve their capabilities. In order to not exceed the length of the couple composed by the motor and the encoder, the maximum relative distance between the two has been constrained by the just mentioned couple length.
Thus, through Equation 3.40 and the equations reported in Table 3.25, the results listed in Table 3.27 have been computed.

Load classification	**Bearing A**	**Bearing B**	**Bearing C**	**Bearing D**
Radial load [N]	F_{r_A}=3.31	F_{r_B}=0.32	F_{r_C}=3.53	F_{r_D}=0.54
Axial load [N]	$F_{a_A} = 0$	$F_{a_B} = 0$	$F_{a_C} = 0$	$F_{a_D} = 0$

Table 3.27: Radial and axial loads from the tangential and separating forces.

As already mentioned, bearings named A and B, placed along the pinion axis, are the ones housed inside the stepper motor AM2224 which has been chosen to command the rotation of the drill. Thus, the obtained radial and axial load of these specific bearings must be lower than the maximum radial and axial loads which can be withstood by the bearings themselves, the referring values are reported in Table 3.28.

Load classification	Bearing RC
Radial load [N]	$F_{r_{RC}}$=8
Axial load [N]	$F_{a_{RC}}$=4

Table 3.28: Maximum radial and axial loads RC bearings can withstand [28].

Preloaded ball bearings, with bearing code RC, can successfully withstand loads caused by spur gears as can be noticed comparing Table 3.27 and Table 3.28.
Differently from bearings A and B, bearings named C and D, which are placed along the rotation axis of drill, have to withstand not only loads due to spur gears but also radial and axial forces caused by drill during drilling activity, identified by F_{r_L} and F_{a_L}. The axial force is the one required by the drill and derives from subsubsection 3.1.2 while the radial force has been oversized by considering it equal to the axial one as shown in Table 3.29.

F_{r_L} [N]	F_{a_L} [N]
5	5

Table 3.29: Radial and axial loads caused by drilling activity.

The axial and radial components reported in Table 3.29 must be added to the ones of bearings named C and D previously computed and listed in Table 3.27. Doing this, the total axial and radial loads acting on bearings named C and D are the ones in Table 3.30.

Load classification	Bearing C	Bearing D
Radial load with drill contribution [N]	F_{r_C}=8.53	F_{r_D}=5.54
Axial load with drill contribution [N]	$F_{a_C} = 5$	$F_{a_D} = 5$

Table 3.30: Total radial and axial loads on bearings named C and D.

Knowing the total radial and axial loads acting on bearings named C and D, the bearing load (equivalent load) P_{EQ} of each bearing, C and D, can be evaluated as follows [43]:

$$P_{EQ} = XF_r + YF_a \tag{3.41}$$

where:

- X: radial load factor.
- Y: axial load factor.
- F_r: radial load, from Table 3.30.
- F_a: axial load, from Table 3.30.

The radial and axial load factors of each bearing, C and D, have been computed exploiting Figure 3.37 [43].

C_{0r}/F_a	$F_a/F_r \leq e$		$F_a/F_r > e$		e
	X	Y	X	Y	
5	1	0	0.56	1.26	0.35
10	1	0	0.56	1.49	0.29
15	1	0	0.56	1.64	0.27
20	1	0	0.56	1.76	0.25
25	1	0	0.56	1.85	0.24
30	1	0	0.56	1.92	0.23
50	1	0	0.56	2.13	0.20

Figure 3.37: Radial and axial load factors computation [43] - *Courtesy of NSK*.

Noticed that C_{0r} refers to the basic static load rating of the chosen bearing, hence, is the one reported in Table 3.17.
The obtained equivalent loads of bearings named C and D are reported in Table 3.31.

P_{EQ_C} [N]	P_{EQ_D} [N]
15.43	13.75

Table 3.31: Equivalent loads of bearings named C and D.

Dealing with ball bearings which have to withstand small values of axial and radial loads has also its drawbacks. In fact, the balls housed in the bearing can crawl instead of rolling if the equivalent load is much lower than the basic load rating. Usually, $P_{EQ} \geq 2\%\ C_r$ is considered sufficient to avoid sliding. Considering the basic static load rating of the chosen bearings series, reported in Table 3.17, $P_{EQ} \geq 25.16$ N.

As can be seen, the obtained equivalent loads of bearings named C and D, reported in Table 3.31, are lower with respect to the threshold needed to avoid balls sliding inside bearing cages, hence, a preload has to be applied. The simplest way of doing this is to use a spring, or bearing preload washer, which mainly acts on the outer ring of one of the two bearings as shown in Figure 3.38. This outer ring must be able to be axially displaced by $H_0 - H_1$ as shown in Figure 3.39. The preload force is considered to remain practically constant, even when there is an axial displacement of the bearing as a result of thermal elongation [60].

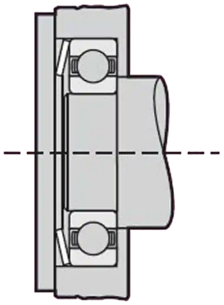

Figure 3.38: Ball bearing disc spring location [62] - *Courtesy of TFC.*

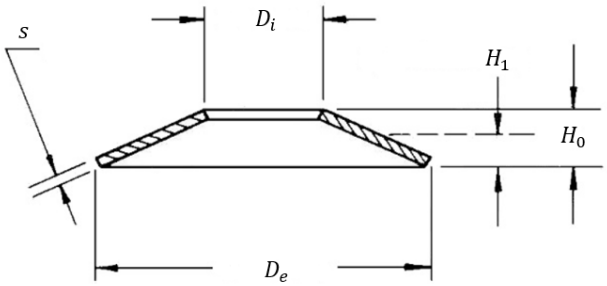

Figure 3.39: Belleville disc spring drawing [51] - *Courtesy of PIC.*

The disc spring has been chosen among all the available ones reported in McMaster-Carr online catalog [38]. The choice was led by searching for a spring compatible with the selected bearings type, R4LZZC3-HMST4, and which can provide the minimum preload force needed to avoid balls sliding phenomenon. The features of the selected ball bearings washer are listed in Table 3.32 and refer to Figure 3.39.

D_i [mm]	D_e [mm]	s [mm]	H_0 [mm]	H_1 [mm]	F_1 [N]
10.31	15.79	0.25	0.56	0.33	31.14

Table 3.32: Belleville disc spring features [38].

Once the suitable spring has been selected, the radial and axial load has been computed again considering that distance dC remain equal as before while dD changes. The latter is modified due to the introduction of the spring. In fact, it is reduced by the free height needed by the chosen disc spring as dD with preload = dD-H_0. The distances which have been considered for the new calculations are reported in Table 3.33.

***dC* with preload [mm]**	***dD* with preload [mm]**
6	32.45

Table 3.33: Distances between bearings and spur gears with preload.

Then, the load due to the disc spring has been added as an axial load as reported in Table 3.34.

Load classification	**Bearing C**	**Bearing D**
Radial load with preload [N]	F_{r_C}=8.54	F_{r_D}=5.55
Axial load with preload [N]	F_{a_C} = 36.14	F_{a_D} = 36.14

Table 3.34: Total radial and axial loads on bearings named C and D.

Eventually, the total radial and axial loads acting on bearings named C and D have been evaluated and exploited for the computation of the new equivalent load. The final results are reported in Table 3.35.

P_{EQ_C} **with preload [N]**	P_{EQ_D} **with preload [N]**
58.63	56.96

Table 3.35: Equivalent loads of preloaded bearings named C and D.

As can be noticed from Table 3.35, after the addition of the wave spring as preload, the equivalent loads of C and D bearings is now higher than 2% C_r ensuring a correct functioning of bearings.
It's important to point out the fact that the equivalent load of C and D bearings is only equal to the preload, provided by the spring, when no drilling activity is performed. This because, during this phase, the drill is not rotating and as a consequence also the spur gears are still. The presence of a constant preload during the whole mission is a positive thing because it contributes to withstand the mechanical environment during launch and through each mission phase.
Eventually, the basic rating life of bearings named C and D, expressed in hours L_h, has

been computed as reported in [43]:

$$L_h = \frac{10^6}{60 n_L} \left(\frac{C_r}{P_{EQ}} \right)^3 \tag{3.42}$$

where:

- n_L: angular speed required at load, from Table 3.18.
- C_r: basic load rating, from Table 3.17.
- P_{EQ}: equivalent load, from Table 3.35.

The obtained basic rating life of bearings C and D, converted from hours to years L_y, are reported in Table 3.36.

L_{yC} [years]	L_{yD} [years]
375	409

Table 3.36: Basic rating life of bearings named C and D in years.

The basic rating life has been computed taking into account the bearing load while drilling which is higher with respect to the one present in the other mission phases in order to consider the worst case of P_{EQ}.
Moreover, the permissible static load factor, f_s, has been evaluated for both bearings C and D as stated:

$$f_s = \frac{C_{0r}}{P_{EQ_0}} \tag{3.43}$$

where:

- C_{0r}: basic static load rating the chosen bearing type, reported in Table 3.17.
- P_{EQ_0}: static equivalent load.
  According to [43], the latter has been evaluated through the following computations:

$$\frac{F_a}{F_r} > 0.8 \quad P_{EQ_0} = 0.6F_r + 0.5F_a \tag{3.44}$$

$$\frac{F_a}{F_r} \leq 0.8 \quad P_{EQ_0} = F_r \tag{3.45}$$

The obtained permissible static load factors of bearings C and D are reported in Table 3.37.

f_{s_C} [-]	f_{s_D} [-]
21.26	23.036

Table 3.37: Permissible static load factor of bearings named C and D.

According to [43], the lower limit of f_s is equal to 1.5 for ball bearings subjected to vibration and shock loads, as the case study. Thus, the obtained results ensure a correct functioning of the chosen bearings also in a stationary condition.
Other two fundamental components are the bearing spacers, for bearing inner and outer race, which have to maintain bearings C and D in their position for the whole mission. As depicted in Figure 3.38, the disc spring has to be placed between the external shell of the experimental chamber and bearing D. Moving away from the external shell, between bearings C and D are placed the two bearings spacers. The bearing spacers diameters have been chosen from Misumi online catalogs [41] [42] according to the bearings type they can be coupled with. While, bearing spacers lengths have been constrained by the distance between bearings C and D. The bearing spacers for bearing outer and inner race dimensions are listed in Table 3.38 and Table 3.39 respectively and refers to Figure 3.40 and Figure 3.41 respectively. Moreover, the bearing spacers have been chosen of type U-CLBU which are made of 5052 Aluminum to be lighter than the ones made of 1018 Steel.

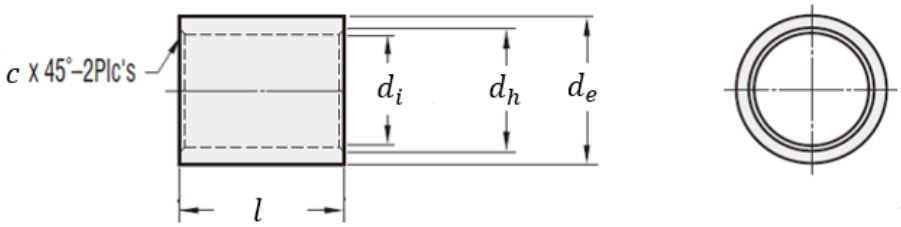

Figure 3.40: Outer race bearing spacer drawing [42] - *Courtesy of Misumi.*

Outer race bearing spacer					
d_e [mm]		l [mm]	d_i [mm]	c [mm]	d_h [mm]
Callout	**Actual**	**Actual**	**Actual**	**Actual**	**Actual**
16.002	15.875	27.290	12.700	0.635	13.970

Table 3.38: Outer race bearings spacer dimensions [42].

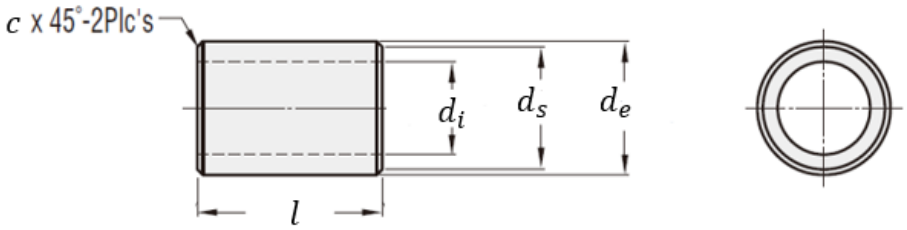

Figure 3.41: Inner race bearing spacer drawing [41] - *Courtesy of Misumi.*

Inner race bearing spacer						
d_i [mm]		d_e [mm]		l [mm]	c [mm]	d_s [mm]
Callout	**Actual**	**Callout**	**Actual**	**Actual**	**Actual**	**Actual**
6.350	6.350	9.652	9.525	27.290	0.635	8.255

Table 3.39: Inner race bearings spacer dimensions [41].

Two cylindrical shaped cases have been preliminarily designed. One to house the stepper motor AM2224RC coupled with its encoder PE22-120. This one has been designed according to the diameter and length, resulting from the coupling of the two components, which are reported in Table 3.23, and considering thicknesses of 2 mm. Another one has been designed to cover the disc spring coupled with the two bearings which are divided by the bearing spacers. The diameter of this case has been constrained by the external diameter of the selected bearings while the length is equal to the one of the other case. The latter because, has already pointed out, bearing D has been positioned far from the external shell by a length equal to the length of the motor coupled with the encoder. Also, the thicknesses of the bearings' case have been assumed of 2 mm. Both of the two cases have been assumed made of the same material of the external shell of the experimental chamber, ISO AL 99.5 and have been considered to be attached to the bottom part of the external shell.

Chamber translation design

The linear actuator has been the first component to be designed in order to develop the mechanism dedicated to the motion of the experimental chamber.
A stepper motor has to be coupled with a screw in order to allow the penetration of the drill bit at a minimum depth equal to the computed choke length and has to provide the torque and the angular velocity to achieve the mechanism goal. Moreover, the linear motor has to provide the required force and speed at the load.

Two alternatives have been investigated for the design of this specific mechanism. The first one, which has been identified as option A, has been developed considering that the chamber moves downwards with the maximum allowed vertical velocity according to Leonardo testing activity [36] and discussed in subsubsection 3.1.2. Considering option A, the distance covered by the chamber allows the screw conveyor to penetrate the Deimos soil for a depth equal to the required choke length. Once the latter is reached, the chamber remains still and the drill continues its rotation for the time needed to acquire the needed soil quantity. While, the option B, has been performed considering that the experimental chamber moves downwards allowing the drill to reach the required choke length in the time needed to convey the needed mass along the screw conveyor. Thus, in option B, the experimental chamber moves for the whole duration of the filling phase. For this second option, the velocity at which the chamber has to translate axially has been computed as:

$$v_L = \frac{l_c}{t_{min}} \tag{3.46}$$

where, considering the screw conveyor having an external diameter of 6.35 mm (1/4"):

- l_c: 6.35 mm, from subsubsection 3.1.2.
- t_{min}: 76.86 min, from subsubsection 3.1.2.

According to the just mentioned options A and B, and considering for both options the maximum value of the axial force obtained from Leonardo testing campaign [36] and discussed in subsubsection 3.1.2, the values reported in Table 3.40 have to be satisfied by the linear motor.

v_L [mm/min]		F_L [N]
Option A	Option B	
18	0.0826	5

Table 3.40: Linear actuator design parameters.

The lead screw series M3x0.5xL1, having features reported in Table 3.41, has been chosen among all the available lead screws in Faulhaber online catalog [25]. This because when lead screw M3x0.5xL1 is coupled to three different stepper motors, as shown in Figure 3.42, it can provide the force and speed values at load required by the mechanism for both option A and B, reported in Table 3.40.

L1 [mm]	Nominal diameter [mm]	Pitch [mm]
15-25-50 or custom	3	0.5

Table 3.41: Features of lead screw M3x0.5xL1 [18].

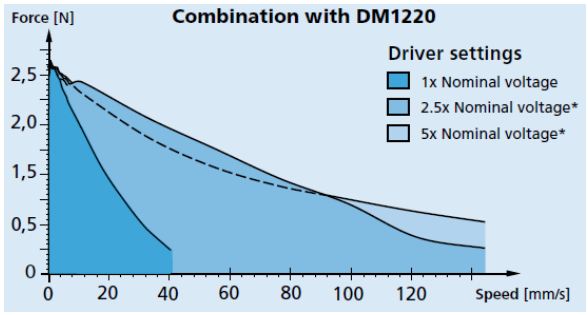

(a) M3x0.5xL1 + DM1220.

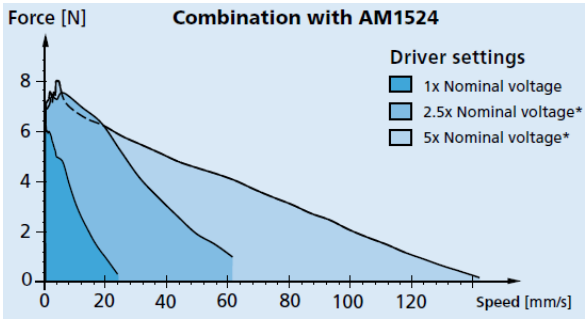

(b) M3x0.5xL1 + AM1524.

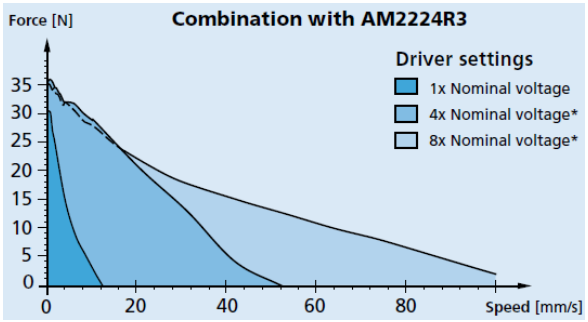

(c) M3x0.5xL1 + AM2224R3.

Figure 3.42: Possible operating curves of different linear actuators [18] - *Courtesy of Faulhaber*.

As can be noticed from Figure 3.42, only the last two stepper motors, AM1524 and AM2224R3, can achieve the required parameters for both options A and B. Of course, among these two, the smaller stepper motor has to be preferred, but it has also to be able of providing the required torque T_M and angular velocity n_M, for both phases A and B, which can be calculated as follows [25]:

$$T_M = \frac{F_L p}{2\pi\eta} \quad n_M = \frac{F_L v_L}{T_M \eta} \frac{1}{2\pi} \tag{3.47}$$

where

- F_L: required force at load, reported in Table 3.40.

- p: lead screw pitch, reported in Table 3.41.
- η: efficiency of the lead screw: 20%. This is due to the coupling male-female, M3x0.5xL1 and a filleted hole in the external shell of the experimental chamber respectively. Lead screws efficiency generally varies from 20% to 80%, in accordance with different manufacturers. The worst value has been taken into account for the design.
- v_L: required speed at load, reported in Table 3.40.

The obtained results for the two considered options, A and B, are shown in Table 3.42.

T_M [Nmm]	n_M [rpm]	
	Option A	Option B
1.99	36	0.17

Table 3.42: Linear actuator design results.

The required torque and angular speed, for each option, can be provided by stepper motors series AM1524 at nominal voltage, as can be noticed from Figure 3.43.

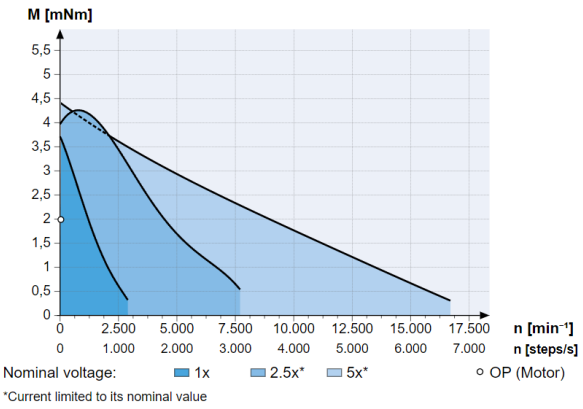

(a) AM1524 OP - Option A.

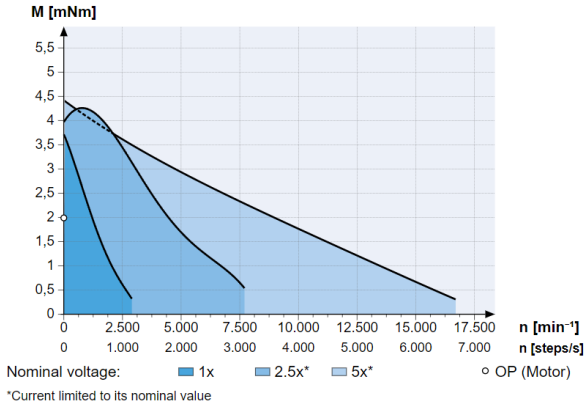

(b) AM1524 OP - Option B.

Figure 3.43: Operating point of AM1524RC considering Option A and Option B [27] - *Courtesy of Faulhaber.*

Stepper motor AM1524 has a TRL ≥ 3. Moreover, as already pointed out in section 2.1, this model of the stepper motor has been chosen with two preloaded ball bearings (RC) and can be coupled with encoder AE23B8-01 which has been chosen with the -01 option: PTFE cables (instead of PVC)[27].

The dimensions of the coupled formed by the chosen stepper motor and its relative encoder are reported in Table 3.43.

Motor + Encoder	d_{M+E} [mm]	L_{M+E} [mm]	L_{CABLES} [mm]
AM1524RC+AE23B8-01	16	28	adjustable

Table 3.43: Dimensions of AM1524RC coupled with AE23B8-01 [25].

The experimental chamber has to be moved downwards during the drilling activity and upwards in the possibility of moving the whole SSA from one point of Deimos surface to another one. This would bring the ability of sampling different soil areas at different depths. To allow this, the chosen stepper motor has to be able to provide the required torque in both CW and CCW directions. Through the exploitation of the 1-axis driver/controller MCST 3601, which is compatible with the selected stepper motor, the motor can fulfill the requirement of changing the direction of motion of the linear actuator load. The linear actuator comprehending lead screw M3x0.5xL1 has to be coupled also with a bearing. This bearing has to be placed at the lead screw tip and has the role of absorbing forces caused during the linear motor activity. The bearing is identified by number 6502.00103, taken from [18], and its dimensions are reported in Table 3.44 referring to Figure 3.44.

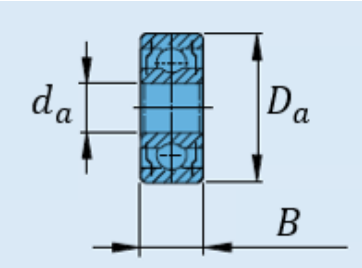

Figure 3.44: Bearing 6502.00103 drawing [18] - *Courtesy of Faulhaber*.

d_a [mm]	D_a [mm]	B [mm]
2.0	6.0	2.5

Table 3.44: Bearing 6502.00103 dimensions [18].

The external shell of the experimental chamber have been preliminarily designed as made of two part: an open on top cylinder covered by a circular disc. Two holes, 180° apart, have

been designed on the base of the cylinder, and they represent the feeding and the discharge hole. Since the drill bit has to be inserted inside the filling hole, it has been designed with a diameter equal to 6.35 mm. Two inlets, pressurizer and solvent respectively, and an outlet for the depressurization have been designed on the disc. The diameter and height of the external shall have been imposed by the selector size, chosen in section 2.1, while the thicknesses have been supposed of 2 mm. The external shell have been assumed made of ISO AL 99.5 to be light but also resistant.
The length L1 of the lead screw has been assumed to be the maximum possible which can be housed inside the payload considering the space occupied by to the motor coupled with the encoder and the bearing. Thus, L1 = 65 mm. On the external shell of the chamber, a female thread has been designed with compatible features to the male one which is represented by the lead screw of the linear actuator. This allows the chamber to be moved by the linear motor.
A cylindrical case has been designed to protect and attach the motor AM1524RC coupled with its encoder AE23B8-01 to one of the internal surfaces of the 1U box containing the SSA. The diameter and length of the case have been constrained by the ones reported in Table 3.43 while thicknesses has been assumed of 2 mm. Another cylindrical case has been developed to forbid movements of the bearing at lead screw tip. To do this, the case has to maintain the bearing attached to the internal surface of 1U structure, opposite to the one where the other case is attached. The reference diameter and length of this case are the ones of the bearing which are indicated in Table 3.16 and, again, thicknesses have been assumed equal to 2 mm. Moreover, both of the two cases have been assumed made of the same material of the external shell of the experimental chamber, ISO AL 99.5.
Three columns have been designed to act as rails during the translational motion of the experimental chamber. All the three columns have been placed at the extremities of the external shell and have been equally displaced. Thus, they can ensure a safe movement of the chamber. The columns have been designed having a diameter of 3 mm and a length equal to 100 mm, the maximum possible, to be attached to the internal structure of 1U box by both ends. Moreover, they have been assumed made of stainless steel.

Enclosed screw conveyor length definition

Once all the components involved in the Surface Sample Analyzer mechanisms have been design, also the design of the enclosed screw conveyor has been concluded by selecting an appropriate length L. The latter has been defined considering that the whole screw conveyor has to be inside the 1U box during all the mission phases except for the ones where the SSA is performing its sampling and acquisition activity. Thus, the total length

has been constrained by the sizes and thicknesses of the SSA box itself and the overall dimensions of the SSA mechanisms components. Taking into account these two aspects: $L = 70$ mm.
As already pointed out, a part of the total length of the drill has to remain always inside the 1U box structure. This length is equal to the total length of the selected drilling motor coupled with its relative encoder plus the external shell of the experimental chamber thickness where the drill is immersed: L_{IN}=48 mm.
The maximum length of the screw conveyor which can exit through the 1U box, containing the SSA, has been obtained considering the just mentioned total and hidden length and 2.5 mm of the hypothesized 1U structure thickness with a distance margin 1U. Thus, $L_{OUT} = 19.5$ mm.
Recalling the micro corer features considered during the design, reported in Table 3.45, and considering that the screw conveyor is able of acquiring different soil samples at different depths by penetrating Deimos soil for a depth equal to the choke length l_c at each time, three acquisitions at most has resulted to be feasible.

D [mm]	p [mm]	D_c [mm]	l_c [mm]	L [mm]	L_{IN} [mm]	L_{OUT} [mm]
6.35	6.35	2	6.35	70	48	19.5

Table 3.45: Features of the vertical enclosed screw conveyor.

Eventually, the enclosed screw conveyor has been preliminarily designed assuming it is made of stainless steel as the micro corers implied in Leonardo testing activity [36].

3.2.3. Mission Phases and Conceptual Operations

The aim of this section is to present the Mission Phases specifically related to the sampling and acquisition activity developed by the Surface Sample Analyzer. The Conceptual Operations, regarding each Mission Phase, are going to be described focusing on which SSA mechanism is involved.

- Resting Phase. This is the phase which precedes the beginning of the sampling and acquisition activity of the Surface Sample Analyzer. During this phase is assumed that the lander, housing the SSA, has safely landed on Deimos and the SSA is lying on Deimos surface with the drill bit perpendicular to it.
  - The selector has a neutral configuration having its hole covered by the external shell of the experimental chamber.

  - The drill is still.
  - The experimental chamber is still.

- Pre-Drilling Phase (1 min). This phase has to prepare the SSA to accept the sampled Deimos soil.

  1. The pressure required inside the experimental chamber is reached thanks to the pressure/depression valve. This, to minimize the friction torques acting during the selector rotation.
  2. - The selector compute a rotation of 90° around its axis of symmetry in order to leave its neutral configuration and assume its filling configuration. At the end of this phase the hole of the selector has to be aligned with the experimental chamber hole where the drill bit is attached.
     - The drill is still.
     - The experimental chamber is still.

Considering Option A:

- Drilling Phase (0.35 min). With this phase starts the drilling activity of the SSA. In particular, the drill bit has to penetrate the soil for a depth equal to the choke length to allow a safe soil acquisition.
  - The selector is still in the filling configuration and ready to acquire the sampled soil from the enclosed screw conveyor.
  - The drill rotates at its nominal angular velocity.
  - The experimental chamber axially moves downwards, guided by the three columns, with the velocity identified in section 2.3 for Option A. Thus, at the end of this phase, the tip of the screw is buried into the soil for a height equal to the required choke length.
- Filling Phase (77 min). During this phase the desired quantity of soil is conveyed along the screw conveyor from the Deimos surface to the experimental chamber.
  - As before, the selector is still in its filling configuration.
  - The screw conveyor rotates at its nominal angular velocity to vertically convey the soil.
  - The chamber is still to maintain the required choke length of the screw for the whole filling phase.

Considering Option B, Drilling Phase and Filling Phase are collapsed together in a single Mission Phase.

- Drilling and Filling Phase (77 min). During this phase starts the drilling activity involving both the rotation of the screw conveyor and the downwards motion of the experimental chamber. Thanks to the latter, the drill reach the required choke length in the time needed to convey the sampled soil through the enclosed screw conveyor.
  - The selector is still in the filling configuration and ready to acquire the sampled soil from the enclosed screw conveyor.
  - The drill rotates at its nominal angular velocity.
  - The experimental chamber axially moves downwards, guided by the three columns, with the velocity identified in section 2.3 for Option B. Thus, at the end of this phase, the tip of the screw is buried into the soil for a height equal to the required choke length.
- Pre-Analysis Phase (1 min). This phase precedes the analysis of the sampled soil.
  - The selector computes a 90° rotation around its axis of symmetry in order to reach its neutral configuration. During this phase the hole of the selector is covered by the external shell of the experimental chamber, thus, no more soil can enter inside the camber.
  - The drill is still.
  - The chamber is still.
- Analysis Phase. During this phase the sampled soil is prepared, and then it is analyzed by the LoC present inside the experimental chamber.
  1. The operating pressure required by the LoC has to be reached through the injection of an inert pressurizer.
  2. The liquid is injected to dilute the soil samples.
  3. The diluted sampled soil is analyzed by the LoC.
  4. After the analysis, the intern of the experimental chamber is depressurized again to reduce friction torques generated during the selector rotation. Also, the depressurization permits the evaporation of the solvent.
  - The selector is still in its neutral configuration.

  - The drill is still.
  - The chamber is still.

- Pre-Discharge Phase (1 min). During this phase the SSA is prepared to discharge the analyzed sampled soil to allow the acquisitions of other samples.
  - The selector computes a 90° rotation around its axis of symmetry in order to assume its discharge configuration having its hole aligned with the discharge hole of the external shell of the chamber.
  - The drill is still.
  - The chamber is still.

- Discharge Phase. During this phase the inert gas is injected to clean the entire experimental chamber from the analyzed soils samples. They are expelled from the chamber and reach the discharge apparatus. Thus, after this phase, The experimental chamber will be ready to house new samples.
  - The selector is still in its discharge phase to allow the sampled soil to exit passing through the discharge hole of the experimental chamber.
  - The drill is still.
  - The chamber is still.

- Pre-Resting Phase (1 min). During this phase the SSA returns in its initial resting configuration.
  - The selector computes a 90° rotation around its axis of symmetry in order to assume its neutral configuration having its hole aligned with the discharge hole of the external shell of the chamber.
  - The drill is still.
  - The chamber is still.

After this phase, there are two possibilities: the SSA has to prepare to sample and acquire another soil at a different depth from the same hole or the SSA has to prepare to be moved to sample and acquire soil from a different location. In the first case, the aforementioned Mission Phases start over. While, in the second case, there is an additional Mission Phase, the Transfer Phase, before starting over with the aforementioned phases.

- Transfer Phase (1 min - Option A, 231 min - Option B). This phase follows the Discharge Phase of the last soil acquisition performed in a specific hole and precedes

the Resting Phase of a new acquisition campaign in a different hole from the previous one.

- The selector is still in a neutral configuration.
- The drill is still.
- The experimental chamber axially moves upwards, guided by the three columns, with the velocity identified in section 2.3 for Option A or for Option B. Thus, the drill from being immersed in soil for a depth equal to three times the choke length will return to be completely inside the 1U box.

The configurations assumed by the selector during the aforementioned Mission Phases are depicted in Figure 3.45.

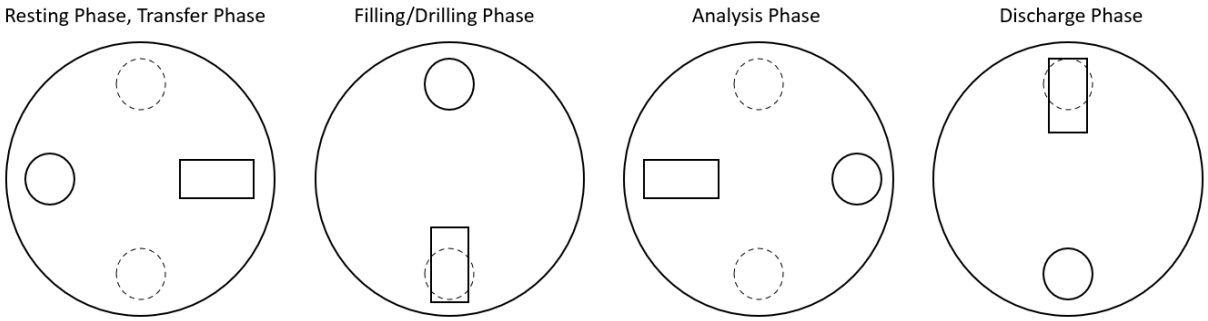

Figure 3.45: Possible selector configurations.

The aforementioned listed Mission Phases for both Option A and B, have been outlined in Figure 3.46 and each mechanism involved in each Mission Phase are highlighted.

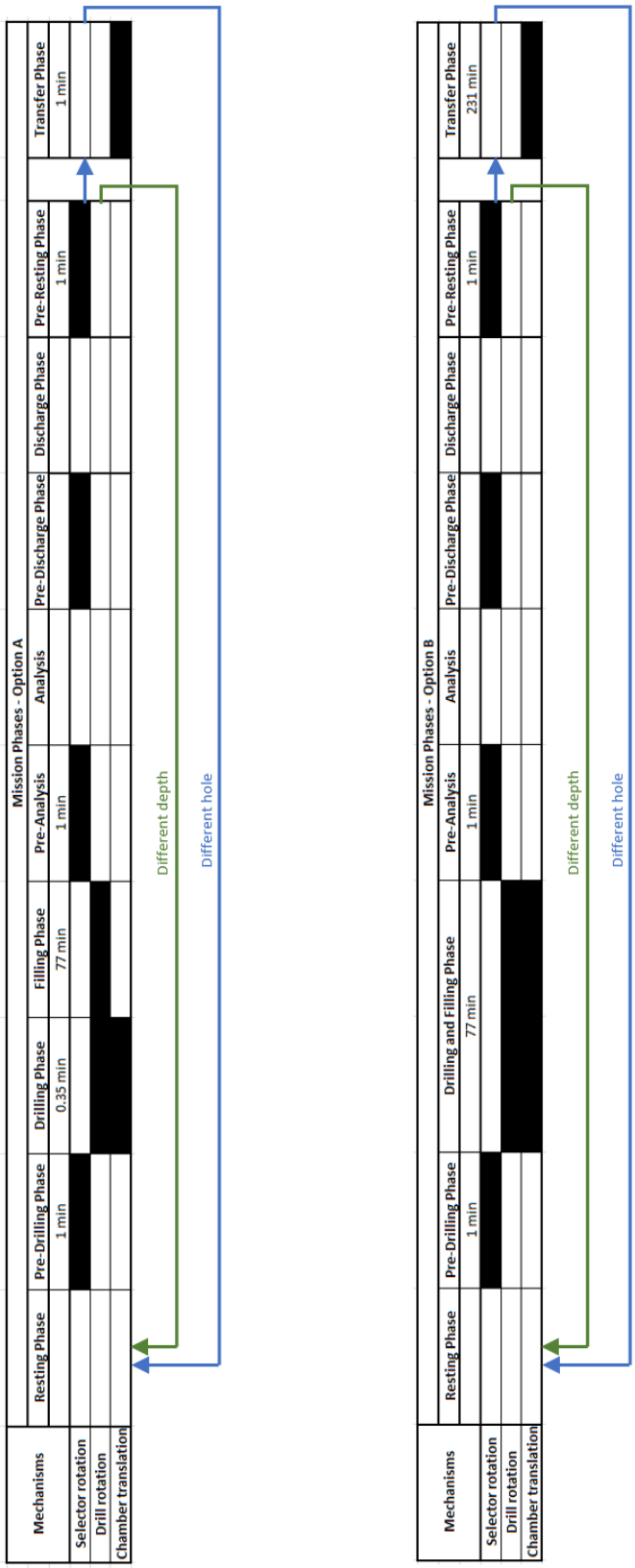

(a) Mission Phases - Option A. (b) Mission Phases - Option B.

Figure 3.46: Mission Phases.

3.2.4. Thermal Control System design

The purpose of the Thermal Control System is to keep the Surface Sample Analyzer and all of its components within a safe operational range. Temperature cannot be controlled directly so the heat fluxes need to be regulated by the TCS.
In order to guarantee the correct operation and highest performances of the system, a preliminary thermal analysis has been conducted. The analysis aims to verify that the system works in the acceptable temperature range. For this reason, the operating minimum and maximum temperature, T_{min} and T_{max} respectively, of each Surface Sample Analyzer component are reported in Table 3.46. As can be noticed from the latter, the device having the most restricted operating temperature range is the LoC. Moreover, the acceptable temperature range has been further restricted: from +9°C to 20°C, applying a safety factor margin of 5°C to both minimum and maximum operative temperature at which the LoC is able to work safely [4].

Component	T_{min} **[°C]**	T_{max} **[°C]**
AM1524RC	-35	+70
AM2224RC	-35	+70
AE23B8	-20	+85
PE22-120	-20	+85
MCST 3601	-30	+70
LoC	+4	+25

Table 3.46: Operating temperature of SSA components [27][28][25][17][26][39].

The study has been performed taking into account the worst case scenario for both hot and cold case. Moreover, to simplify the analysis the following assumptions have been taken:

- SSA is lumped in one single node with a spherical shape and a surface equal to the outer 1U CubeSat surface.
- Steady state conditions: no temperature variations have been considered.
- The area subjected to external radiation is equivalent to the surface area of the sphere. This because, at this level, is unknown the precise position of the SSA within the lander structure.
- The dissipating area is equivalent to the surface area of the sphere. This because,

as before, at this level, is unknown the precise position of the SSA within the lander structure.

- The solar radiation is assumed to be constant along the entire Deimos orbit.
- The radiation is assumed hitting perpendicularly the reference area.
- The Surface Sample Analyzer is housed in a lander which can provide to it or remove from it heat, if necessary, to keep it inside its admissible temperature range.

In the hot case, the total heat comprehending both environmental and internal heat sources has been evaluated as follows [4]:

$$Q_{HOT} = Q_{Sun} + Q_{IR_{Deimos}} + Q_{IR_{Mars}} + Q_{a_{Deimos}} + Q_{a_{Mars}} + Q_{int_{HOT}} \tag{3.48}$$

where

- Q_{Sun}: the heat generated by the Sun radiation:

$$Q_{Sun} = G_S A_S \alpha_S \tag{3.49}$$

  where:

  - G_S: the solar flux at the spacecraft distance: 607.77 W/m^2 [4].
  - A_S: the area subjected to external radiation: 0.06 m^2.
  - α_S: the solar absorptivity of the coating material: 0.06 [4].

- $Q_{IR_{Deimos}}$ and $Q_{IR_{Mars}}$: the heats due to the infrared radiation coming from Deimos and Mars respectively:

$$Q_{IR} = \sigma T_P^4 \frac{(R_P)^2}{(R_P + H_{s/c})^2} A_S \epsilon_{IR} \tag{3.50}$$

  where:

  - σ: Stefan-Boltzmann constant: 5.67x10^{-8} $\frac{W}{m^2 K^4}$.
  - T_P: the average planet temperature: 233 K for Deimos and 208 K for Mars [46].
  - R_P: the planet mean radius: 6.2 km for Deimos and 3389.5 km for Mars [46].
  - $H_{s/c}$: the spacecraft height from the planet surface: 0 km for Deimos, since SSA is on Deimos surface, 20068 km for Mars, since SSA is orbiting around

Mars on Deimos orbit [46].

– ϵ_{IR}: the infrared emissivity of the coating material: 0.8 [4].

- $Q_{a_{Deimos}}$ and $Q_{a_{Mars}}$ are the heats caused by the albedo of Deimos and Mars respectively.

$$Q_a = G_S a \frac{(R_P)^2}{(R_P + H)^2} A_S \alpha_S K_a \tag{3.51}$$

where:

$$K_a = 0.657 + 0.54 \frac{R_P}{R_P + H_{s/c}} - 0.196 \frac{(R_P)^2}{(R_P + H_{s/c})^2} \tag{3.52}$$

where: a: albedo: 0.08 for Deimos and 0.250 for Mars [52][46].

- $Q_{int_{HOT}}$: the internal heat generated by the SSA components during the hot case. It has been assumed that the whole electrical power demanded by a working device is then converted into heat. For the hot case, the Mission Phase presenting the higher power demand required by the Mechanisms Subsystem components has been taken into account. Thus, referring to the system power budget, reported insubsubsection 3.2.6, $Q_{int_{HOT}} = 10.18$W.

Consequently, the heat to be dissipated towards the deep space is Q_{HOT}.
On the other hand, in the cold case the external heat source still reaching the lander, hence the SSA, is assumed to be only the infrared heat coming from Deimos [4]:

$$Q_{COLD} = Q_{IR_{Deimos}} + Q_{int_{COLD}} \tag{3.53}$$

where: $Q_{int_{COLD}}$: the internal heat generated by the SSA components during the cold case. Referring to the system power budget, reported in subsubsection 3.2.6, there are Mission Phases in which there are no working Mechanisms Subsystem components, hence, no power generation, have been taken into account for this case. Thus, $Q_{int_{COLD}} = 0$W.
Therefore, in the cold case the heat to be dissipated is Q_{COLD}.
The obtained heat fluxes are reported in Table 3.47 end it is noticeable that the highest heat source is the power generated by the SSA devices during the hot case.

Q_S [W]	$Q_{IR_{Deimos}}$ [W]	$Q_{IR_{Mars}}$ [W]	$Q_{a_{Deimos}}$ [W]	$Q_{a_{Mars}}$ [W]	$Q_{int_{HOT}}$ [W]	$Q_{int_{COLD}}$ [W]
5.94	8.021	0.10	0.47	0.023	10.18	0

Table 3.47: Thermal contributes on the SSA.

Eventually, from the obtained Q_{HOT} and Q_{COLD} the Surface Sample Analyzer tempera-

tures, in the hot and cold case respectively, have been computed as follows:

$$T = \sqrt[4]{\frac{Q}{\epsilon_{IR}\sigma A_{IR}}} \tag{3.54}$$

where: A_{IR}: the dissipating area: 0.06 m^2.
The results are reported in Table 3.48.

Hot case	**Cold case**
Q_{HOT} = 24.75 W	Q_{COLD} = 8.02 W
T_{HOT} = 35.66°C	T_{COLD} = -40.15°C

Table 3.48: Results of the TCS design.

The preliminary TCS analysis has been performed exploiting a passive thermal control. In fact, all the external surfaces of the SSA have been assumed to be covered by Silverized FEP Teflon which presents low absorptivity and high emissivity when the Teflon is about 0.127 mm (5 mils) thick [4] [31]. However, as can be noticed looking at the TCS analysis results in Table 3.48, the obtained temperature in both hot and cold case exceed the required temperature range. Thus, an active thermal control has been developed.
In the hot case, the heat which have to be removed, named $Q_{radiator}$, has been evaluated assuming the SSA having the maximum admissible temperature imposed by the LoC:

$$Q_{radiator} = Q_{Sun} + Q_{IR_{Deimos}} + Q_{IR_{Mars}} + Q_{a_{Deimos}} + Q_{a_{Mars}} + Q_{int_{HOT}} - \epsilon_{IR}\sigma A_{IR} T^4_{HOT_{max}} \tag{3.55}$$

While, in the cold case, the heat which have to be provided to the SSA, named Q_{heater}, has been computed considering the SSA being at the minimum allowed operating temperature according to the LoC:

$$Q_{heater} = -Q_{a_{Deimos}} - Q_{int_{COLD}} + \epsilon_{IR}\sigma A_{IR} T^4_{COLD_{max}} \tag{3.56}$$

The results deriving from the aforementioned computations are reported in Table 3.49.

$\boldsymbol{Q_{radiator}}$ **[W]**	$\boldsymbol{Q_{heater}}$ **[W]**
3.47	7.61

Table 3.49: Radiator and heater heat for hot and cold case respectively.

The results of the preliminary thermal analysis of the Surface Sample Analyzer lead to the requirements which have to be satisfied by the lander permitting the SSA to safely perform its Mission Phases. In fact, the lander has to remove from the SSA the power amount indicated as $Q_{radiator}$ during the hot case and has to provide to the SSA the power amount named Q_{heater} during the cold case. The latter has been also considered as an input for the development of the power budget of the system reported in subsubsection 3.2.6.

3.2.5. Electrical Power System design

The electrical power system is the subsystem used to supply the electrical power to all the other subsystems and components of a spacecraft. It is of great importance that the EPS is able to grant the required power in all the phases and modes of the mission. In this preliminary phase design of SSA, the system has been designed in a very simple way, further refinements will have to be performed to make sure that all the requirements coming from every other subsystem as well as design consideration are respected. Therefore, at this level, the EPS sizing serves as a baseline to develop correctly the subsystem and have a general idea of what are the power and mass budgets needed for the mission accomplishment.

The constraints of the Surface Sample Analyzer size, and consequently mass, have suggested considering that the power supply required from each SSA device is provided by the 3U lander EPS in which SSA is housed. Thus, the feeding line from the lander EPS to the mechanisms motors and relative components are depicted in Figure 3.47.

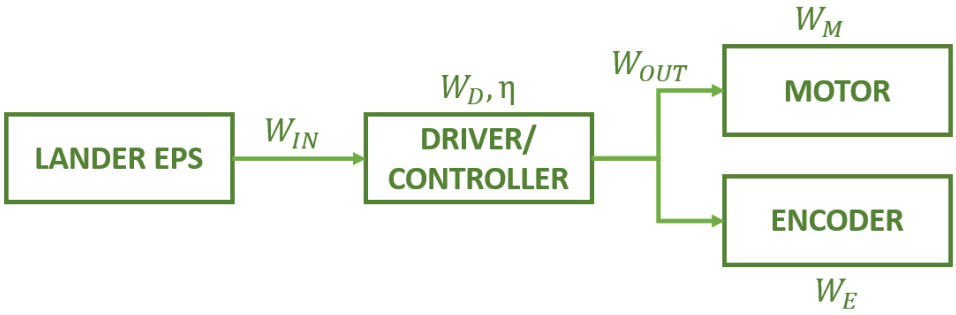

Figure 3.47: Drawing of EPS feeding line.

As can be noticed from Figure 3.47, the power required as well as the range of admissible voltage and current of each component have to be investigated to establish the lander EPS requirements. For this reason in Table 3.50 the different nominal voltage V and current I required by each component have been summarized.

Component	V [V]	I [A]
MCST 3601	9 - 36	0 - 1.1
AM1524RC	2, 3.5, 6, 12	0.45, 0.25, 0.15, 0.075
AM2224RC	1.4, 3, 6, 12	1, 0.5, 0,25, 0.125
AE23B8-01	5 - 15	0.005 (5V)
PE22-120	4.5 - 5.5	0.02 (5V)

Table 3.50: Components nominal voltage and current values [26][27][28][25][17].

To define the power needed by each component of the SSA, the following steps have been followed referring to Figure 3.47.
Firstly, the power required by each motor and its relative encoder has been computed exploiting the power definition:

$$W = VI \tag{3.57}$$

W_M and W_E have been used to indicate the motor and encoder power demand respectively. Then, the total amount of power W_{OUT} which have to provided by the driver/controller has been evaluated as stated:

$$W_{OUT} = W_M + W_E \tag{3.58}$$

The power required by the driver, named W_D, has been evaluated considering that it receives power from the lander EPS, W_{IN}, and has to satisfy the power demand of both motor and encoder, W_{OUT}, but it is effected by a power loss:

$$W_D = W_{IN} - W_{OUT} \quad \eta = \frac{W_{OUT}}{W_{IN}} \tag{3.59}$$

where η: driver efficiency: assumed equal to 90 %.
Accordingly, the driver/controller power supply has been expressed as:

$$W_D = \left(\frac{1}{\eta} - 1\right)(W_M + W_E) \tag{3.60}$$

The aforementioned computations have been developed to identify the power required by the MCST 3601 driver connected to AM1524RC and AE23B8, involved in selector rotation and chamber translation mechanisms, and then to evaluate the power supply for the MCST 3601 driver feeding AM2224RC and PE22-120, involved in the drill rotation mechanism. The obtained results are reported in Table 3.51.

Component	W [W]
AM1524RC	0.9
AE23B8-01	0.025
MCST 3601	0.103

(a) Power supply needed by AM1524RC, AE23B8-01 and MCST 3601.

Component	W [W]
AM2224RC	6
PE22-120	0.1
MCST 3601	0.627

(b) Power supply needed by AM2224RC, PE22-120 and MCST 3601.

Table 3.51: Power supply needed by SSA components.

The obtained results have been evaluated taking into account one of the four possible motor windings for both AM1524RC and AM2224RC and assuming a provided voltage of 12V. The encoders have been considered to be supplied by a voltage of 5V. The chosen driver/controller MCST 3601 is able of providing as output the same amount of voltage received as input and is capable of regulating the output current depending on stepper motor or encoder necessities. This second aspect is relevant to avoid possible power surges which can damage both the stepper motor and the encoder.
As can be noticed from 3.51b, the power required by AM2224RC is equal to four time its nominal power. This because, referring to section 2.2, AM2224RC requires a boosted voltage equal to four times its nominal voltage. Moreover, by comparing the obtained results reported in Table 3.51, the drilling motor has resulted to be the most demanding device in terms of power supply.
The supply power needed by each component has lead the formulation of the power budget of the system as reported in subsubsection 3.2.6. From the latter, the power supply which the lander EPS has to provide, at each Mission Phase, has been established.

3.2.6. System budgets

A marginal philosophy has been adopted for the estimation of the Surface Sample Analyzer mass and power budgets. In general, in successive phases of the design, power and mass tend to increase with respect to the initial phases budgets, because subsystems are better detailed. Margins are applied in this preliminary phase to account for this. Two levels of margins are used: at component and at sub-system level. The component level is referred to the TRL and reliability of the specific component: lower TRL or ground-designed component may require some extra precautions (e.g. add shielding-mass against radiation). The sub-system level depends again on the reliability: not yet proven in flight

systems have lower margin to be accounted. Referring to ESA margin philosophy [15], the following Design Maturity mass/power Margins shall be applied at equipment level:

- 5%: for COTS items [15].
- 10%: for COTS items requiring minor modifications [15].
- 20%: for designed or developed from scratch items, or items requiring major modifications [15].

Then, a 20% overall system margin has been applied to both total power and mass obtained, again, accordingly to ESA margin philosophy [15]. Among all the preliminarily designed components, the pressure/depression valve and the LoC have not been taken into account in both mass and power budget. This because they have not yet been identified precisely, and they have been assumed providing negligible mass and power consumption with respect to the others SSA components.

Power budget

The power budget for the different Mission Phases, considering both options A and B, of the Surface Sample Analyzer has been reported in Figure 3.48 and Figure 3.49. It has been developed taking into account the power required by each working Mechanisms Subsystem components obtained in subsection 3.2.5 and the power required for the cold case analyzed in the TCS design as reported in subsection 3.2.4. The power required by the TCS has been considered equal to the obtained Q_{heater} for the considered cold case, hence, when there are no working Mechanisms Subsystem components. While, the TCS power has been considered up to the obtained Q_{heater} value to ensure SSA works respecting its operating temperatures range also in the other Mission Phases which don't represent the hot or cold case analyzed in the TCS design reported in subsection 3.2.4. Of course, for the considered hot case, hence, when the Mission Phases with the maximum power demand from the working Mechanisms Subsystem components is considered, no additional power is required by the TCS. Moreover, the Mission Phases involving the same mechanisms for both phases A and B have been considered together. The power contributes which have been resulted from the power budget represent the power which the lander EPS has to provide to the SSA during the mission.

Pre-Drilling, Pre-Analysis, Pre-Discharge, Pre-Resting Phase - Option A,B

Subsystems	Components	Vithout Margin [V]	Maturity Level	Margin [%]	Margin [V]	Vith Margin [V]	Quantity	Total with Margin[V]	Subsystems Power [V]
Mechanisms: Selector rotation, Drill rotation, Chamber translation	Stepper Motor AM1524RIC	0,90	certified	5	0,05	0,95	1	0,95	
	Driver MCST 3601	0,10	to be modified	10	0,01	0,11	1	0,11	
	Encoder AE23B8-01	0,03	certified	5	0,00	0,03	1	0,03	
	Stepper Motor AM2224RIC	0	to be modified	10	0	0	1	0	
	Driver MCST 3601	0	to be modified	10	0	0	1	0	
	Encoder PE22-120	0	to be modified	10	0	0	1	0	
	Stepper Motor AM1524RIC	0	certified	5	0	0	1	0	
	Driver MCST 3601	0	certified	10	0	0	1	0	1,08
	Encoder AE23B8-01	0	certified	5	0	0	1	0	
TCS	Heater	up to 7,81	to be developed	20	1,52	9,13	1	9,13	9,13

Total System Power Vithout Margin [V]	10,22
System Margin [%]	20
System Margin [V]	2,04
Total System Power Vith Margin [V]	12,26

Drilling Phase - Option A, Drilling and Filling Phase - Option B

Subsystems	Components	Vithout Margin [V]	Maturity Level	Margin [%]	Margin [V]	Vith Margin [V]	Quantity	Total with Margin[V]	Subsystems Power [V]
Mechanisms: Selector rotation, Drill rotation, Chamber translation	Stepper Motor AM1524RIC	0	certified	5	0	0	1	0	
	Driver MCST 3601	0	to be modified	10	0	0	1	0	
	Encoder AE23B8-01	0	certified	5	0	0	1	0	
	Stepper Motor AM2224RIC	6,00	to be modified	10	0,60	6,60	1	6,60	
	Driver MCST 3601	0,63	to be modified	10	0,06	0,69	1	0,69	
	Encoder PE22-120	0,10	to be modified	10	0,01	0,11	1	0,11	
	Stepper Motor AM1524RIC	0,90	certified	5	0,05	0,95	1	0,95	
	Driver MCST 3601	0,10	to be modified	10	0,01	0,11	1	0,11	8,48
	Encoder AE23B8-01	0,03	certified	5	0,00	0,03	1	0,03	
TCS	Heater	0	to be developed	20	0,20	0	1	0	0

Total System Power Vithout Margin [V]	8,48
System Margin [%]	20
System Margin [V]	1,70
Total System Power Vith Margin [V]	10,18

Filling Phase - Option A

Subsystems	Components	Vithout Margin [V]	Maturity Level	Margin [%]	Margin [V]	Vith Margin [V]	Quantity	Total with Margin[V]	Subsystems Power [V]
Mechanisms: Selector rotation, Drill rotation, Chamber translation	Stepper Motor AM1524RIC	0	certified	5	0	0	1	0	
	Driver MCST 3601	0	to be modified	10	0	0	1	0	
	Encoder AE23B8-01	0	certified	5	0	0	1	0	
	Stepper Motor AM2224RIC	6,00	to be modified	10	0,60	6,60	1	6,60	
	Driver MCST 3601	0,63	to be modified	10	0,06	0,69	1	0,69	
	Encoder PE22-120	0,10	to be modified	10	0,01	0,11	1	0,11	
	Stepper Motor AM1524RIC	0	certified	5	0	0	1	0	
	Driver MCST 3601	0	to be modified	10	0	0	1	0	
	Encoder AE23B8-01	0	certified	5	0	0	1	0	7,40
TCS	Heater	up to 7,81	to be developed	20	1,52	9,13	1	9,13	9,13

Total System Power Vithout Margin [V]	16,53
System Margin [%]	20
System Margin [V]	3,31
Total System Power Vith Margin [V]	19,84

Figure 3.48: EPS budget (1/2).

Transfer Phase - Option A,B

Subsystems	Components	Vithout Margin [W]	Maturity Level	Margin [%]	Margin [W]	Vith Margin [W]	Quantity	Total with Margin[W]	Subsystems Power [W]
Mechanisms: Selector rotation, Drill rotation, Chamber translation	Stepper Motor AM1524PIC	0	certified	5	0	0	1	0	
	Driver MCST 3601	0	to be modified	10	0	0	1	0	
	Encoder AE23B8-01	0	certified	5	0	0	1	0	
	Stepper Motor AM2224PIC	0	to be modified	10	0	0	1	0	
	Driver MCST 3601	0	to be modified	10	0	0	1	0	
	Encoder PE22-120	0	to be modified	10	0	0	1	0	
	Stepper Motor AM1524PIC	0,90	certified	5	0,05	0,95	1,00	0,95	
	Driver MCST 3601	0,10	to be modified	10	0,01	0,11	1,00	0,11	
	Encoder AE23B8-01	0,03	certified	5	0,00	0,03	1,00	0,03	1,08
TCS	Heater	up to 7,61	to be developed	20	1,52	9,13	1	9,13	9,13

Total System Power Vithout Margin [W]	10,22
System Margin [%]	20
System Margin [W]	2,04
Total System Power Vith Margin [W]	12,26

Resting Phase, Analysis Phase, Discharge Phase - Option A,B

Subsystems	Components	Vithout Margin [W]	Maturity Level	Margin [%]	Margin [W]	Vith Margin [W]	Quantity	Total with Margin[W]	Subsystems Power [W]
Mechanisms: Selector rotation, Drill rotation, Chamber translation	Stepper Motor AM1524PIC	0	certified	5	0	0	1	0	
	Driver MCST 3601	0	to be modified	10	0	0	1	0	
	Encoder AE23B8-01	0	certified	5	0	0	1	0	
	Stepper Motor AM2224PIC	0	to be modified	10	0	0	1	0	
	Driver MCST 3601	0	to be modified	10	0	0	1	0	
	Encoder PE22-120	0	to be modified	10	0	0	1	0	
	Stepper Motor AM1524PIC	0	certified	5	0	0	1	0	
	Driver MCST 3601	0	to be modified	10	0	0	1	0	
	Encoder AE23B8-01	0	certified	5	0	0	1	0	0
TCS	Heater	7,61	to be developed	20	1,52	9,13	1	9,13	9,13

Total System Power Vithout Margin [W]	9,13
System Margin [%]	20
System Margin [W]	1,83
Total System Power Vith Margin [W]	10,96

Figure 3.49: EPS budget (2/2).

Mass budget

The mass of each component belonging to each Surface Sample Analyzer subsystem has been reported in Figure 3.50. As can be noticed from the latter, each component has been highlighted with a specific color to indicate if its mass has been taken from the data-sheet or if has been assumed accordingly to its CAD model. There were no indication about the encoders mass, and their available CAD models comprehend also the motors they are coupled with. Thus, the encoders mass has been oversized and assumed equal to the mass of the motors they are related to.
The mass, obtained from the budget, is lower than 1.33 kg which is the usually considered maximum mass for 1U CubeSat. This, even though there are still missing items that will have to be designed once the position of the Surface Sample Analyzer inside the 3U lander is defined. These components are drivers/controllers, the discharge apparatus, the two tanks housing the solvent and the inert gas, and the cables required by each SSA component.

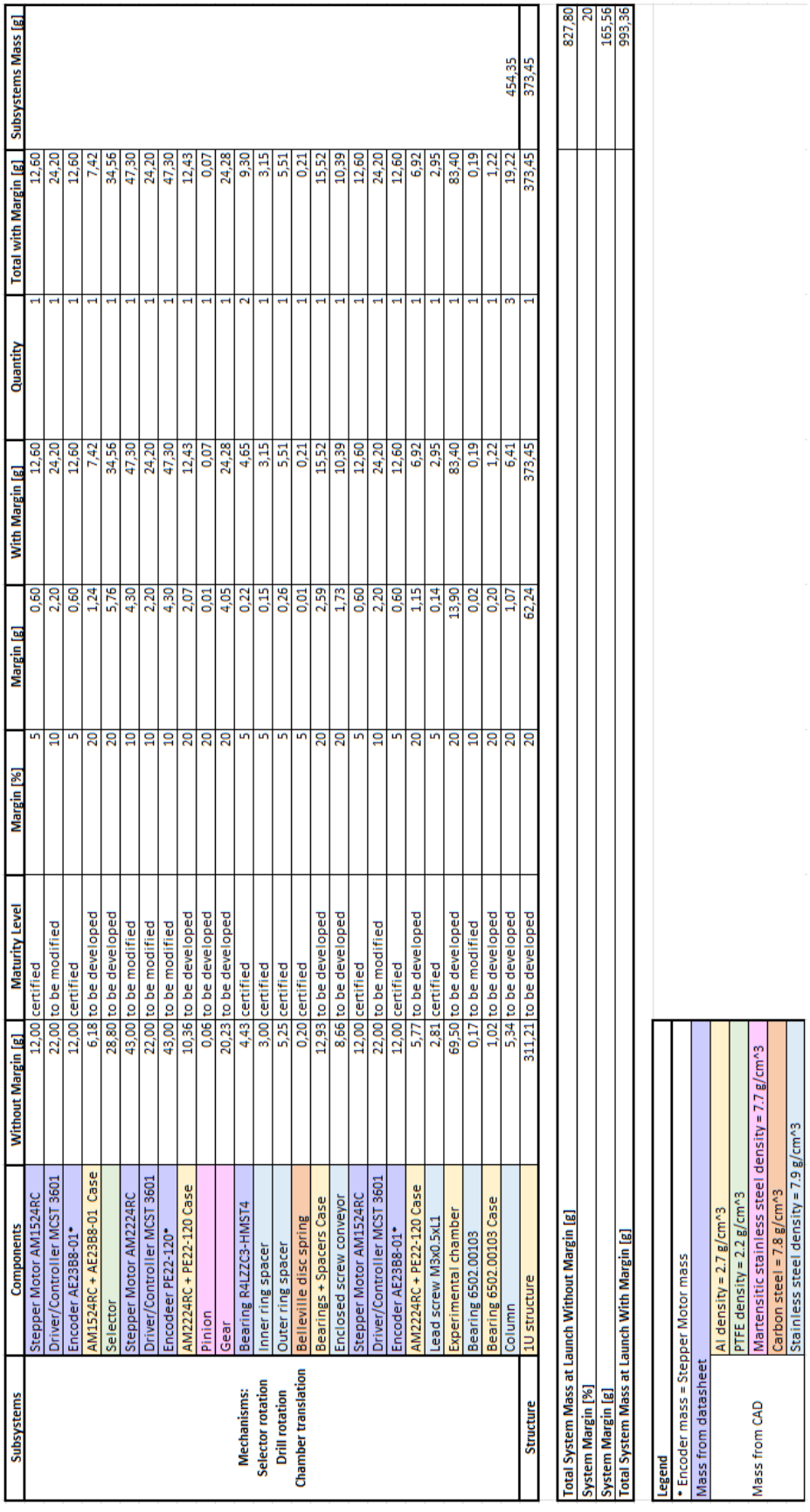

Subsystems	Components	Without Margin [g]	Maturity Level	Margin [%]	Margin [g]	With Margin [g]	Quantity	Total with Margin [g]	Subsystems Mass [g]
Mechanisms: Selector rotation	Stepper Motor AM1524RC	12,00	certified	5	0,60	12,60	1	12,60	
	Driver/Controller MCST 3601	22,00	to be modified	10	2,20	24,20	1	24,20	
	Encoder AE23B8-01*	12,00	certified	5	0,60	12,60	1	12,60	
	AM1524RC + AE23B8-01 Case	6,18	to be developed	20	1,24	7,42	1	7,42	
	Selector	28,80	to be developed	20	5,76	34,56	1	34,56	
Drill rotation	Stepper Motor AM2224RC	43,00	to be modified	10	4,30	47,30	1	47,30	
	Driver/Controller MCST 3601	22,00	to be modified	10	2,20	24,20	1	24,20	
	Encodeer PE22-120*	43,00	to be modified	10	4,30	47,30	1	47,30	
	AM2224RC + PE22-120 Case	10,36	to be developed	20	2,07	12,43	1	12,43	
	Pinion	0,06	to be developed	20	0,01	0,07	1	0,07	
	Gear	20,23	to be developed	20	4,05	24,28	1	24,28	
Chamber translation	Bearing R4LZZC3-HMST4	4,43	certified	5	0,22	4,65	2	9,30	
	Inner ring spacer	3,00	certified	5	0,15	3,15	1	3,15	
	Outer ring spacer	5,25	certified	5	0,26	5,51	1	5,51	
	Belleville disc spring	0,20	certified	5	0,01	0,21	1	0,21	
	Bearings + Spacers Case	12,93	to be developed	20	2,59	15,52	1	15,52	
	Enclosed screw conveyor	8,66	to be developed	20	1,73	10,39	1	10,39	
	Stepper Motor AM1524RC	12,00	certified	5	0,60	12,60	1	12,60	
	Driver/Controller MCST 3601	22,00	to be modified	10	2,20	24,20	1	24,20	
	Encoder AE23B8-01*	12,00	certified	5	0,60	12,60	1	12,60	
	AM2224RC + PE22-120 Case	5,77	to be developed	20	1,15	6,92	1	6,92	
	Lead screw M3x0.5xL1	2,81	certified	5	0,14	2,95	1	2,95	
	Experimental chamber	69,50	to be developed	20	13,90	83,40	1	83,40	
	Bearing 6502.00103	0,17	to be modified	10	0,02	0,19	1	0,19	
	Bearing 6502.00103 Case	1,02	to be developed	20	0,20	1,22	1	1,22	
	Column	5,34	to be developed	20	1,07	6,41	3	19,22	454,35
Structure	1U structure	311,21	to be developed	20	62,24	373,45	1	373,45	373,45

Total System Mass at Launch Without Margin [g]	827,80
System Margin [%]	20
System Margin [g]	165,56
Total System Mass at Launch With Margin [g]	993,36

Legend	
* Encoder mass = Stepper Motor mass	
Mass from datasheet	
Mass from CAD	Al density = 2.7 g/cm^3
	PTFE density = 2.2 g/cm^3
	Martensitic stainless steel density = 7.7 g/cm^3
	Carbon steel = 7.8 g/cm^3
	Stainless steel density = 7.9 g/cm^3

Figure 3.50: Surface Sample Analyzer mass budget.

4 | Surface Sample Analyzer requirements

The most significant Surface Sample Analyzer requirements, derived from the preliminarily conducted design, are going to be presented in this chapter.

4.1. Functional requirements

The functional requirements are listed in Table 4.1 and Table 4.2.

4.1.1. Technological requirements

ID	Importance	Verification	Requirement
SSA-FR-01.1	NH	T	The product components shall have a TRL $\geq$ 3.

Table 4.1: Surface Sample Analyzer technological requirements list.

4.1.2. Performance requirements

ID	Importance	Verification	Requirement
SSA-FR-02.1	M	T	The product shall provide drilling thrust and torque of 5 N and 0.05 Nm respectively.
SSA-FR-02.2	M	T	The product shall provide drilling axial velocity of 18 mm/min - Option A, 0.0826 mm/min - Option B and angular velocity of 50 rpm.

Table 4.2: Surface Sample Analyzer performance requirements list.

4.2. Mission requirements

The mission requirements are listed in Table 4.3, Table 4.4 and Table 4.5.

4.2.1. Launch segment requirements

ID	Importance	Verification	Requirement
SSA-MIR-01.1	M	T	The product shall be launched as a secondary payload.
SSA-MIR-01.2	M	T	The launch mass of 993.36 g shall be considered.
SSA-MIR-01.3	NH	T	The launch date shall be in 2027 (See Appendix A).

Table 4.3: Surface Sample Analyzer launch segment requirements list.

4.2.2. Life requirements

ID	Importance	Verification	Requirement
SSA-MIR-02.1	NH	T	The mission shall last at least 1 year (See Appendix A).

Table 4.4: Surface Sample Analyzer life requirements list.

4.2.3. Touchdown requirements

ID	Importance	Verification	Requirement
SSA-MIR-03.1	M	T	The product shall be placed on Deimos surface with the drill bit perpendicular to it.
SSA-MIR-03.2	M	T	The product shall be anchored to the surface.

Table 4.5: Surface Sample Analyzer touchdown requirements list.

4.3. Interface requirements

The interface requirements are listed in Table 4.6 and Table 4.7.

4.3.1. TCS requirements

ID	Importance	Verification	Requirement
SSA-INR-01.1	M	T	The product shall survive and operate between +9°C and +20°C.
SSA-INR-01.2	M	T	The product shall be covered by Silverized FEP Teflon.
SSA-INR-01.3	M	T	The product shall be able to dissipate 3.47 W, in hot case.
SSA-INR-01.4	M	T	The product shall be able to acquire 7.61 W, in cold case.

Table 4.6: Surface Sample Analyzer TCS requirements list.

4.3.2. EPS requirements

ID	Importance	Verification	Requirement
SSA-INR-02.1	M	T	The product shall be supplied by a power of 12.26 W during Pre-Filling, Pre-Analysis, Pre-Discharge, Pre-Resting Phase - Option A, B and Transfer Phase - Option A, B.
SSA-INR-02.2	M	T	The product shall be supplied by a power of 10.18 W during Drilling Phase - Option A, Drilling/Filling Phase - Option B.
SSA-INR-02.3	M	T	The product shall be supplied by a power of 19.84 W during Filling Phase - Option A.
SSA-INR-02.4	M	T	The product shall be supplied by a power of 10.96 W during Resting, Analysis, Discharge Phase - Option A, B.

Table 4.7: Surface Sample Analyzer EPS requirements list.

4.4. Environmental requirements

The environmental requirements are listed in Table 4.8.

ID	Importance	Verification	Requirement
SSA-ENV-01.1	M	T	The product shall withstand CVCM < 0.1%.
SSA-ENV-01.2	M	T	The product shall withstand RML < 1%.
SSA-ENV-01.3	M	T	The product shall withstand a maximum TID of 30 krad(Si) (See Appendix A).

Table 4.8: Surface Sample Analyzer environmental requirements list.

4.5. Verification requirements

The verification requirements are listed in Table 4.9.

ID	Importance	Verification	Requirement
SSA-VER-01.1	M	T	The product shall undergo structural testing on ground before launch.
SSA-VER-01.2	M	T	The product shall undergo thermal testing on ground before launch.
SSA-VER-01.3	M	T	The product shall undergo microgravity testing on ground before launch.
SSA-VER-01.4	M	T	The product shall undergo out gassing testing on ground before launch.
SSA-VER-01.5	M	T	The product shall undergo radiation testing on ground before launch.
SSA-VER-01.6	M	T	The product shall undergo functional testing on ground before launch.

Table 4.9: Surface Sample Analyzer verification requirements list.

5 | Conclusions and future developments

In this final chapter is going to be reviewed and discussed the conducted thesis' work, comprehending also the critical aspects, and the future improvements to be made.

5.1. Conclusions

The High Level Requirements, hence, the goals of the Surface Sample Analyzer have been achieved through the preliminary design which have been conducted. The requirements have been met through the exploitation of specific COTS items or preliminarily designed components, which have to be developed from scratch. In fact, the preliminarily designed SSA is able of sampling soil at different depths. In particular, the Surface Sample Analyzer, thanks to the preliminarily designed enclosed vertical screw conveyor, can acquire soil samples from the surface up to about 2 cm depth. Moreover, if the lander, where the SSA is housed, can be safely moved from one location on the surface to others, the Surface Sample Analyzer can study soil samples belonging to different areas. Thus, the surface can be somehow mapped highlighting the presence or the absence of particular soil's geological features which can be identified by the LoC markers. There was also another requirement which has been successfully gained: the Surface Sample Analyzer have been designed to fit inside a 1U CubeSat. The preliminarily designed SSA has a mass at launch equal to 993.36 g, the maximum mass considered for 1U CubeSat is about 1.33 kg, and the preliminarily designed components occupy about 15% of the total 1U volume. These values, of course, will change in the next phases of the mission design, when more and more components will be added. However, the fundamental elements, able of providing the required thrust, torque and power to allow a safe drilling process, according to Leonardo testing activity [36], have been arranged inside a 1U structure without interfering with each other. In addition, most of the selected COTS components are suitable for space applications. Thus, the components' requirement of having a minimum TRL value or the requirements related to the environment, in particular involving out

gassing or radiation tolerance properties, have been achieved. While, the others COTS items, which do not comply with the aforementioned requirements, such as stepper motor AM2224RC, encoder PE22-120 and driver/controller MCST 3601, have to be slightly modified. Usually, only the cables materials have to be changed (e.g: from PVC to PTFE) in stepper motors, encoders and drivers/controllers, such as others electronic devices, in order to resist to extreme environments like space. Some reasonable precautions have been adopted while designing all the others components which were not already available on the market. In fact, they have been preliminarily designed following standardized rules and exploiting space proven materials in order to be effectively manufactured and suitable for space applications.
The idea of exploiting the preliminarily designed Surface Sample Analyzer in other missions, distinct from the TASTE mission, hence, sampling and analyzing soils different from the Deimos one, has been realized. This, thanks to the soil simulant NU-LHT-2M, implied in Leonardo testing activity [36], which presents similar composition and geotechnical properties to lunar highlands simulants, Phobos and C-type asteroids regolith in addition to the one of Deimos.
Eventually, also the goal of innovating the extraterrestrial drilling missions, especially asteroid mining, through the exploitation of a compact sampling mechanisms with integrated bio-marker analyzer has been satisfied. Thus, asteroids soils presenting areas difficult to be reached through big satellites or rovers, can be studied thanks to the analysis of their soil's properties performed by small CubeSats.

5.2. Future developments

The preliminary design of the Surface Sample Analyzer has been developed taking into account some assumptions. Some of them derive from the fact that the SSA will be housed inside a lander, but its precise position within the latter is still an open question. This observation involves the design of the missing components such as the discharge apparatus, where the analyzed soil samples are received after being expelled by the experimental chamber during the Discharge Phase, the two tanks housing the solvent and the inert gas, which allows the correct functioning of the LoC, and the pressure/depression valve. For the same reason, also the effective position of each of the three drivers/controllers MCST 3601, capable of controlling the motion of one stepper motor each and regulating the current supply needed by the latter, has to be decided further on. This because, once the position of the Surface Sample Analyzer within the lander and with respect to its subsystems will be decided, the power feeding and input control line from the lander EPS and OBDH respectively to the SSA components, passing through the drivers/controllers,

will be designed as well. Also, the positioning of cables, required by each component, represent an important aspect that will have to be investigated. Moreover, also a more appropriate thermal analysis of the Surface Sample Analyzer will be conducted taking into account the effective SSA surfaces which exchange heat with the lander, with Deimos soil or through the deep space. The thermal analysis might be improved considering a multi-nodes analysis, instead of a single node, and exploiting also the view factors between the Sun, Mars and Deimos and the lander and, more specifically, the SSA.
Once the definitive components and configuration of the Surface Sample Analyzer will be selected, a complete and detailed structural and thermal analysis has to be developed involving both each single components and the payload as a whole and for each Mission Phases. This, to ensure that both the COTS components and the ones designed from scratch are able to withstand structural loads as well as unexpected thermal shocks during the entire mission. Moreover, the system has to be tested on ground to verify it can safely operate in space, thus, in presence of microgravity, out gassing condition and radiations sources. Eventually, the Surface Sample Analyzer functions have to be tested. For example, the developed theoretical design has to be verified through numerical simulations and experimental activities. This to ensure the effective direct conveying of the sampled soil along the preliminarily designed enclosed screw conveyor, from the soil to the experimental chamber. The two different Options A and B, for developing the Drilling and Filling Phases, have to be investigated in order to affirm if they are both feasible or not and if one of the two it's better than the other one. Also, numerical simulations representing the motion of the soil samples within the experimental chamber, during the different Mission Phases, would be useful to assure a safe Analysis Phase. In fact, once the samples reach the experimental chamber, and after the liquid injection, the solution has to converge to the sensitive surface of the LoC. This, revising also the topology and surface properties of the selector. Then, during the Discharge Phase, the analyzed soil samples have to be expelled from the experimental chamber and have to reach the discharge apparatus.
Another important aspect, that will have to be taken into account in further developments, is the design of a sort of anchoring system to permit a safe drilling process. In fact, during drilling activities in microgravity environments, such as on small satellites (e.g: Deimos) or asteroids, it's fundamental to anchor the drilling equipment to the soil to avoid the rotation or the translation of the latter together with the drill bit or the experimental chamber respectively.

Bibliography

[1] V. Badescu. *Asteroids: Prospective energy and material resources*. Springer Science & Business Media, 2013.

[2] Y. Bar-Cohen and K. Zacny. *Drilling in extreme environments: penetration and sampling on earth and other planets*. John Wiley & Sons, 2009.

[3] M. B. Bastrzyk, C. C. Daniels, J. J. Oswald, P. H. Dunlap Jr, and B. M. Steinetz. Material properties of three candidate elastomers for space seals applications. Technical report, 2010.

[4] C. D. Brown. *Elements of spacecraft design*. Aiaa, 2002.

[5] D. H. Buckley. *Friction, wear, and lubrication in vacuum*, volume 277. National Aeronautics and Space Administration, 1971.

[6] B. J. Buratti and P. C. Thomas. Planetary satellites. In *Encyclopedia of the Solar System*, pages 759–777. Elsevier, 2014.

[7] J. Burton, P. Taborek, and J. Rutledge. Temperature dependence of friction under cryogenic conditions in vacuum. *Tribology Letters*, 23(2):131–137, 2006.

[8] F. Concli. Quaderni di progettazione: Ingranaggi i. *Il Progettista industriale*, 7: 048–052, 2018.

[9] Conveyor Equipment Manufacturers Association. Screw Conveyors for Bulk Materials, 2019. URL `https://cemanet.org/wp-content/uploads/2019/06/ANSI-CEMA-350-FinalReview.pdf`.

[10] Deutsches Institut fur Normung E.V. (DIN). DIN 780-Part 1 - Module for spur gears, 1977. URL `https://it.scribd.com/doc/283210267/DIN-780Part-1`.

[11] P. Di Lizia, F. Bernelli-Zazzera, A. Ercoli-Finzi, S. Mottola, C. Fantinati, E. Remetean, and B. Dolives. Planning and implementation of the on-comet operations of the instrument sd2 onboard the lander philae of rosetta mission. *Acta Astronautica*, 125:183–195, 2016.

[12] T. C. Duxbury, A. V. Zakharov, H. Hoffmann, and E. A. Guinness. Spacecraft exploration of phobos and deimos. *Planetary and Space Science*, 102:9–17, 2014.

[13] B. S. Engineering. Coefficient of thermal expansion for various materials at different temperatures. Technical report, Technical Report TR-18 (Rev. F), Bal Seal Engineering Europe, 2004.

[14] ESA. SPace ENVironment Information System. URL `https://www.spenvis.oma.be/`.

[15] ESA. Margin philosophy for science assessment studies, 2012. URL `https://sci.esa.int/documents/34375/36249/1567260131067-Margin_philosophy_for_science_assessment_studies_1.3.pdf`.

[16] FAULHABER. APPLICATIONNOTE004 - When and why using an encoder. URL `https://www.faulhaber.com/fileadmin/user_upload_global/support/MC_Support/Motors/AppNotes/Faulhaber_AN004_EN.pdf`.

[17] FAULHABER. Encoders Series PE22-120, 2020. URL `https://www.faulhaber.com/fileadmin/Import/Media/EN_PE22-120_FPS.pdf`.

[18] FAULHABER. Lead Screw Series M3x0.5xL1, 2020. URL `https://www.faulhaber.com/fileadmin/Import/Media/EN_LSM3-0_FPS.pdf`.

[19] FAULHABER. Stepper Motors Series AM0820, 2020. URL `https://www.faulhaber.com/fileadmin/Import/Media/EN_AM0820_FPS.pdf`.

[20] FAULHABER. Stepper Motors Series AM1020, 2020. URL `https://www.faulhaber.com/fileadmin/Import/Media/EN_AM1020_FPS.pdf`.

[21] FAULHABER. Stepper Motors Series AM1220, 2020. URL `https://www.faulhaber.com/fileadmin/Import/Media/EN_DM1220_FPS.pdf`.

[22] FAULHABER. Stepper Motors Series AM2224R3, 2020. URL `https://www.faulhaber.com/fileadmin/Import/Media/EN_AM2224R3_FPS.pdf`.

[23] FAULHABER. Encoders Series IEM3-1024, 2020. URL `https://www.faulhaber.com/fileadmin/Import/Media/EN_IEM3-1024_DFF.pdf`.

[24] FAULHABER. Stepper Motors Series DM0620, 2022. URL `https://www.faulhaber.com/fileadmin/Import/Media/EN_DM0620_FPS.pdf`.

[25] FAULHABER. FAULHABER online catalog, 2022. URL `https://www.faulhaber.com/it/`.

[26] FAULHABER. Motion Controller Series MCST 3601, 2022. URL `https://www.faulhaber.com/fileadmin/Import/Media/EN_MCST3601_FPS.pdf`.

[27] FAULHABER. Stepper Motors Series AM1524, 2022. URL `https://www.faulhaber.com/fileadmin/Import/Media/EN_AM1524_FPS.pdf`.

[28] FAULHABER. Stepper Motors Series AM2224, 2022. URL `https://www.faulhaber.com/fileadmin/Import/Media/EN_AM2224_FPS.pdf`.

[29] B. Gale, M. Eddings, S. Sundberg, A. Hatch, J. Kim, T. Ho, and S. Karazi. Low-cost mems technologies. In *Reference Module in Materials Science and Materials Engineering*. Elsevier, 2016.

[30] R. Han, X. Quan, Y. Shao, and K. Niu. Tribological properties of phenyl-silicone rubber composites with nano-ceo2 and graphene under thermal-oxidative aging. *Applied Nanoscience*, 10(7):2129–2138, 2020.

[31] R. Hoffman. Spaceflight performance of silver coated fep teflon as a thermal control surface on the imp-1 spacecraft. Technical report, 1973.

[32] N. Khun, H. Zhang, J. Yang, and E. Liu. Tribological performance of silicone composite coatings filled with wax-containing microcapsules. *Wear*, 296(1-2):575–582, 2012.

[33] D. Knez and M. Khalilidermani. A review of different aspects of off-earth drilling. *Energies*, 14(21):7351, 2021.

[34] M. Lavagna, J. Brucato, F. Fiore, M. Bechini, A. Capannolo, T. Fornaro, A. Meneghin, D. Paglialunga, R. Piazzolla, G. Poggiali, et al. Taste mission to deimos: Terrain analyzer and sample tester explorer with smallsat and miniaturized lander. In *52nd Lunar and Planetary Science Conference*, number 2548, page 1991, 2021.

[35] S.-J. Lee, Y.-C. Sohn, and C.-L. Kim. Friction and wear characteristics of polydimethylsiloxane under water-based lubrication conditions. *Materials*, 15(9):3262, 2022.

[36] Leonardo. LDD-TN-TRP-0202, Test Report TN-202 Small sample collection. 2015.

[37] K. Manick, P. Rowley, L. D. N. Koor, H. Schroeven-Deceuninck, and C. L. Smith. Starting a European Space Agency Sample Analogue Collection (ESA^{2}C) and Curation Facility for Exploration Missions: GEOTECHNICAL CHARACTERISATION. URL `https://www.hou.usra.edu/meetings/lpsc2017/eposter/1222.pdf`.

[38] McMaster-Carr. Belleville Disc Springs for Ball Bearings. URL https://www.mcmaster.com/bearing-preload-washers/system-of-measurement~inch/od~0-618/id~0-406/.

[39] A. Meneghin, D. Paglialunga, G. Poggiali, S. Pirrotta, G. Impresario, A. Sabatini, C. Pacelli, A. Nascetti, L. Iannascoli, S. Carletta, et al. Astrobio cubesat: a nanosatellite for space astrobiology experiments. In *European Planetary Science Congress*, pages EPSC2020–943, 2020.

[40] A. Meneghin, J. R. Brucato, D. Paglialunga, A. Nascetti, L. Iannascoli, G. Poggiali, S. Carletta, L. Schirone, S. Pirrotta, G. Impresario, et al. Astrobio cubesat: operational design of a cubesat for astrobiological purposes in radiative environment. Technical report, Copernicus Meetings, 2021.

[41] MiSUMi. Bearing Spacers - For Bearing Inner Race -, . URL https://us.misumi-ec.com/pdf/fa/2009/inch_p277.pdf.

[42] MiSUMi. Bearing Spacers - For Bearing Outer Race -, . URL https://us.misumi-ec.com/pdf/fa/2009/inch_p279.pdf.

[43] Motion and Control NSK. ROLLING BEARINGS, . URL https://www.nsk-literature.com/en/rolling-bearings/offline/download.pdf.

[44] Motion and Control NSK. TECHNICAL REPORT, . URL https://www.nsk-literature.com/en/technical-report/offline/download.pdf.

[45] S. Murugesan. An overview of electric motors for space applications. *IEEE transactions on industrial electronics and control instrumentation*, (4):260–265, 1981.

[46] NASA. Solar System Exploration, . URL https://solarsystem.nasa.gov/.

[47] NASA. Planetary satellites mean elements, . URL https://ssd.jpl.nasa.gov/sats/elem/.

[48] NSK. SPACEA, . URL https://www.nsk.com/ctrg/.

[49] NSK. ROLLING BEARINGS, . URL https://www.nsk-literature.com/en/rolling-bearings/offline/download.pdf.

[50] B. N. Persson. Silicone rubber adhesion and sliding friction. *Tribology letters*, 62(2): 1–5, 2016.

[51] PIC. Belleville spring washers. URL https://www.pic-designcatalog.com/d6-20.html.

[52] K. R. Ramsley and J. W. Head. The origins and geological histories of deimos and phobos: Hypotheses and open questions. *Space Science Reviews*, 217(8):1–35, 2021.

[53] A. W. Roberts. The influence of granular vortex motion on the volumetric performance of enclosed screw conveyors. *Powder Technology*, 104(1):56–67, 1999.

[54] A. W. Roberts and A. Willis. Performance of grain augers. *Proceedings of the Institution of Mechanical Engineers*, 176(1):165–194, 1962.

[55] C. Schrader, D. Rickman, C. McLemore, and J. Fikes. Lunar regolith simulant user's guide. Technical report, 2010.

[56] SDP/SI. ELEMENTS OF METRIC GEAR TECHNOLOGY . URL `https://www.sdp-si.com/PDFS/Elements-of-Metric-Gear-Technology.pdf`.

[57] E. Secretariat. Space product assurance, thermal vacuum outgassing test for the screening of space materials. Technical report, Technical Report ECSS-Q-70-02A, ESA-ESTEC Requirements & Standards, 2000.

[58] E. Secretariat. Space product assurance, data for selection of space materials and processes. Technical report, Technical Report ECSS-Q-70-71A Rev. 1, ESA-ESTEC Requirements & Standards, 2004.

[59] E. Secretariat. Space engineering, mechanisms. Technical report, Technical Report ECSS-E-ST-33-01C Rev. 2, ESA-ESTEC Requirements & Standards, 2019.

[60] SKF. Homepage SKF. URL `https://www.skf.com/it`.

[61] C. L. Smith, K. Manick, C. Mavris, M. S. Rumsey, L. Duvet, and H. Schroeven-Deceuninck. Starting a European Space Agency Sample Analogue Collection (ESA^2C) and Curation Facility for Exploration Missions. URL `https://www.hou.usra.edu/meetings/lpsc2017/eposter/1218.pdf`.

[62] TFC. Ball bearing location disk spring. URL `https://tfc.eu.com/ball-bearings/ball-bearing-location-disc-spring/`.

[63] P. Thannasi, K. Muthukkumaran, V. Indaram, et al. Assessment of geotechnical properties of lunar soil simulant's for lunar missions. *Indian Journal of Engineering and Materials Sciences (IJEMS)*, 28(4):317–329, 2021.

[64] P. Thomas. Surface features of phobos and deimos. *Icarus*, 40(2):223–243, 1979.

[65] G. Wypych. *Handbook of polymers*. Elsevier, 2022.

[66] T. Zhang, W. Zhang, K. Wang, S. Gao, L. Hou, J. Ji, and X. Ding. Drilling, sampling, and sample-handling system for china's asteroid exploration mission. *Acta Astronautica*, 137:192–204, 2017.

A | Appendix

The maximum TID which the Surface Sample Analyzer can withstand is 30 krad(Si) considering the external structure made of ISO AL 99.5 with 2 mm thicknesses. The analysis has been performed exploiting ESA's SPace ENVironment Information System (SPENVIS) [14]. The input parameters were:

- Mars reference system.
- the orbital parameters of the s/c. Thus, the mean orbital parameters of Deimos, taken from NASA Jet Propulsion Laboratory database [47], have been inserted as reported in Figure A.1.
- the date of the beginning of the orbit. It has been supposed starting from 2028.
- the mission duration. It has been considered equal to 1 year.

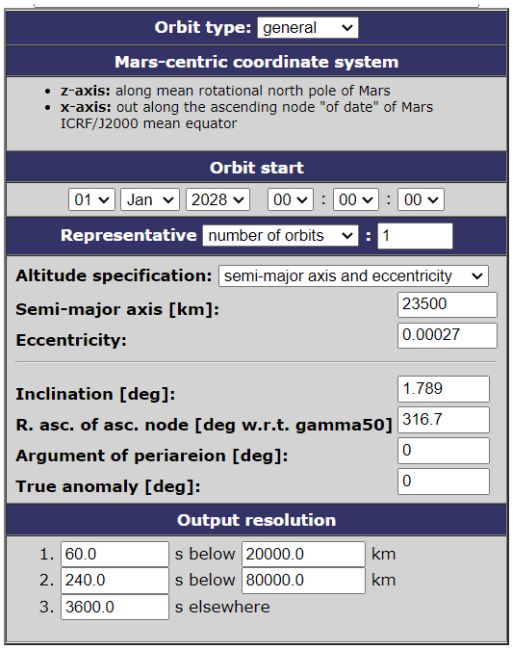

Figure A.1: SPENVIS input parameters - *Courtesy of ESA*.

The obtained result is shown in Figure A.2.

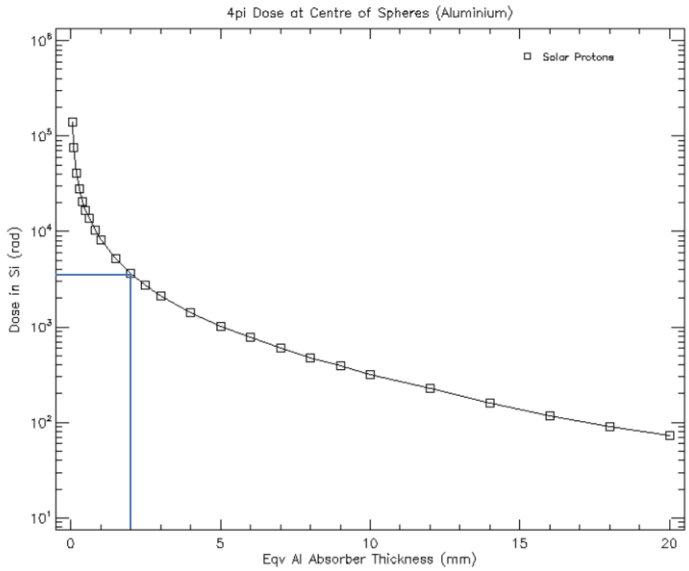

Figure A.2: Total ionizing dose with respect to shielding thickness.

The only contribution of the Total Ionizing Dose on Deimos is due to solar protons.

List of Figures

List of Tables

List of Symbols

Variable	Description	SI unit
$\boldsymbol{A_{IR}}$	dissipating area by radiation	W
$\boldsymbol{A_L}$	lateral area	m^2
$\boldsymbol{A_S}$	area absorbing external radiation	m^2
$\boldsymbol{a}$	gears inter-axis	m
$\boldsymbol{a_{eff}}$	effective gears inter axis	m
$\boldsymbol{b}$	band width	m
$\boldsymbol{b_{eff}}$	effective band width	m
$\boldsymbol{b_{min}}$	minimum band width	m
$\boldsymbol{C}$	radial clearance	m
$\boldsymbol{C_r}$	basic load rating	N
$\boldsymbol{C_{0r}}$	basic static load rating	N
$\boldsymbol{D}$	screw diameter	m
$\boldsymbol{D_A}$	outer diameter of bearing in free configuration	m
$\boldsymbol{D_b}$	outer diameter of bearing in mounted configuration	m
$\boldsymbol{D_C}$	core diameter shaft	m
$\boldsymbol{D_e}$	outer diameter of disc spring	m
$\boldsymbol{D_i}$	inner diameter of disc spring	m
$\boldsymbol{d_a}$	inner diameter of bearing in free configuration	m
$\boldsymbol{dA}$	distance of bearing A	m
$\boldsymbol{d_e}$	outer diameter of bearing spacer	m
$\boldsymbol{d_h}$	hole diameter of outer race bearing spacer	m
$\boldsymbol{d_i}$	inner diameter of bearing in mounted configuration	m
$\boldsymbol{dB}$	distance of bearing B	m
$\boldsymbol{dC}$	distance of bearing C	m

Variable	Description	SI unit
dD	distance of bearing D	m
d_i	inner diameter of bearing spacer	m
d_M	motor diameter	m
d_{M+E}	motor + encoder diameter	m
dp_1	pinion reference diameter	m
$dp_{1_{eff}}$	effective pinion reference diameter	m
dp_2	gear reference diameter	m
$dp_{2_{eff}}$	effective gear reference diameter	m
d_s	hole diameter of inner race bearing spacer	m
F_a	axial force	N
F_{a_A}	axial force at bearing A	N
F_{a_B}	axial force at bearing B	N
F_{a_C}	axial force at bearing C	N
F_{a_D}	axial force at bearing D	N
F_{a_L}	axial force at load	N
$F_{a_{RC}}$	axial force at bearing RC	N
F_C	centrifugal force	N
F_F	friction force	N
F_L	axial force at load	N
F_N	resultant of normal forces	N
F_r	radial force	N
F_{r_A}	radial force at bearing A	N
F_{r_B}	radial force at bearing B	N
F_{r_C}	radial force at bearing C	N
F_{r_D}	radial force at bearing D	N
F_{r_L}	radial force at load	N
$F_{r_{RC}}$	radial force at bearing RC	N
F_{s_A}	separating force at bearing A	N
F_{s_B}	separating force at bearing B	N
F_{s_C}	separating force at bearing C	N
F_{s_D}	separating force at bearing D	N

Variable	Description	SI unit
F_{s_L}	separating force at load	N
F_{s_M}	separating force at motor	N
F_t	tangential force at teeth contact	N
F_{t_A}	tangential force at bearing A	N
F_{t_B}	tangential force at bearing B	N
F_{t_C}	tangential force at bearing C	N
F_{t_D}	tangential force at bearing D	N
F_{t_L}	tangential force at load	N
F_{t_M}	tangential force at motor	N
F_1	force provided by disc spring	N
f_s	permissible static load factor	-
f_{s_C}	permissible static load factor of bearing C	-
f_{s_D}	permissible static load factor of bearing D	-
G_S	solar flux	W/m^2
g	acceleration of gravity	m/s^2
g_{α_P}	length of action	m
H	selector height	m
H_0	free height of disc spring	m
H_1	compressed height of disc spring	m
$H_{s/c}$	s/c height from planet surface	m
h	whole depth	m
h_a	addendum	m
h_f	dedendum	m
I	current	A
K	surface synthetic factor	Pa
K^*	chosen surface synthetic factor	Pa
L	enclosed screw conveyor total length	m
L_{CABLES}	cables length	m
L_h	basic rating life in hours	s
L_{IN}	enclosed screw conveyor length inside 1U box	m
L_{y_C}	basic rating life of bearing C in years	s

Variable	Description	SI unit
L_{y_D}	basic rating life of bearing D in years	s
L_M	motor length	m
L_{M+E}	motor + encoder length	m
L_{OUT}	enclosed screw conveyor length out 1U box	m
l	length of bearing spacer	m
M	selector mass	kg
M_{min}	minimum mass quantity	kg
m	gear module	m
m_{eff}	effective gear module	m
n_L	rotational speed at load	rev/s
n_M	rotational speed at motor	rev/s
P	pressure	Pa
P_{EQ}	equivalent load	N
P_{EQ_C}	equivalent load at bearing C	N
P_{EQ_D}	equivalent load at bearing D	N
P_{EQ_0}	equivalent load	N
P_M	power at motor	W
P_L	power at load	W
p	pitch	m
p_b	base pitch	mm
p_f	fitting at tooth base	mm
Q	heat	W
Q_a	heat due to albedo	W
$Q_{a_{Deimos}}$	heat due to Deimos albedo	W
$Q_{a_{Mars}}$	heat due to Mars albedo	W
Q_{COLD}	total heat in cold case	W
Q_m	theoretical mass flow rate	kg/s
Q_{heater}	heat provided by heater	W
Q_{HOT}	total heat in hot case	W
$Q_{int_{COLD}}$	internal heat in cold case	W
$Q_{int_{HOT}}$	internal heat in hot case	W

Variable	Description	SI unit
$\boldsymbol{Q_{IR}}$	heat due to radiation	W
$\boldsymbol{Q_{IR_{Deimos}}}$	heat due to Deimos radiation	W
$\boldsymbol{Q_{IR_{Mars}}}$	heat due to Mars radiation	W
$\boldsymbol{Q_{radiator}}$	heat subtracted by radiator	W
$\boldsymbol{Q_S}$	heat due to Sun radiation	W
$\boldsymbol{Q_t}$	volumetric theoretical throughput	m^3/s
$\boldsymbol{R}$	selector radius	m
$\boldsymbol{R_M}$	mean radius	m
$\boldsymbol{R_P}$	planet mean radius	m
$\boldsymbol{r}$	generic radius	m
$\boldsymbol{s}$	thickness of disc spring	m
$\boldsymbol{T}$	temperature	K
$\boldsymbol{T_{COLD}}$	temperature in cold case	K
$\boldsymbol{T_{COLD_{max}}}$	maximum admissible temperature in cold case	K
$\boldsymbol{T_{HOT}}$	temperature in hot case	K
$\boldsymbol{T_{HOT_{max}}}$	maximum admissible temperature in hot case	K
$\boldsymbol{T_L}$	torque at load	Nm
$\boldsymbol{T_{F_{TOT}}}$	total friction torque	Nm
$\boldsymbol{T_{F_B}}$	base friction torque	Nm
$\boldsymbol{T_{F_L}}$	lateral friction torque	Nm
$\boldsymbol{T_M}$	torque at motor	Nm
$\boldsymbol{T_{max}}$	maximum admissible temperature	K
$\boldsymbol{T_{min}}$	minimum admissible temperature	K
$\boldsymbol{T_P}$	planet temperature	K
$\boldsymbol{t}$	blade thickness	m
$\boldsymbol{t_s}$	time	s
$\boldsymbol{U_L}$	tooth root synthetic factor	Pa
$\boldsymbol{U_L^*}$	chosen tooth root synthetic factor	Pa
$\boldsymbol{u}$	gear ratio	-
$\boldsymbol{u_{eff}}$	effective gear ratio	-
$\boldsymbol{V}$	voltage	V

Variable	Description	SI unit
$\boldsymbol{V_A}$	absolute velocity of particles	m/s
$\boldsymbol{V_L}$	conveying component of velocity	m/s
$\boldsymbol{V_R}$	relative velocity between particles and screw conveyor	m/s
$\boldsymbol{V_S}$	velocity of screw conveyor	m/s
$\boldsymbol{V_T}$	rotational component of velocity	m/s
$\boldsymbol{v_L}$	velocity at load	m/s
$\boldsymbol{W}$	power supply	W
$\boldsymbol{W_D}$	driver power supply	W
$\boldsymbol{W_E}$	encoder power supply	W
$\boldsymbol{W_M}$	motor power supply	W
$\boldsymbol{X}$	radial load factor	-
$\boldsymbol{Y}$	axial load factor	-
$\boldsymbol{z_1}$	pinion teeth number	-
$\boldsymbol{z_{1_{eff}}}$	effective pinion teeth number	-
$\boldsymbol{z_2}$	crown teeth number	-
$\boldsymbol{z_{2_{eff}}}$	effective crown teeth number	-
$\boldsymbol{z_{min}}$	minimum pinion teeth number	-
$\boldsymbol{\alpha}$	helix angle of screw	deg
$\boldsymbol{\alpha_M}$	mean helix angle of screw	deg
$\boldsymbol{\alpha_P}$	angle of pressure	deg
$\boldsymbol{\alpha_S}$	solar absorptivity	-
$\boldsymbol{\Delta A_B}$	infinitesimal base area	m^2
$\boldsymbol{\Delta F_A}$	infinitesimal axial force	N
$\boldsymbol{\Delta F_D}$	infinitesimal drag force	N
$\boldsymbol{\Delta F_{DA}}$	axial infinitesimal drag force component	N
$\boldsymbol{\Delta F_{DT}}$	tangential infinitesimal drag force component	N
$\boldsymbol{\Delta F_N}$	infinitesimal normal force	N
$\boldsymbol{\Delta F_{Na}}$	infinitesimal lateral normal force	N
$\boldsymbol{\Delta F_{Nc}}$	infinitesimal centrifugal force	N
$\boldsymbol{\Delta F_R}$	infinitesimal resultant force	N
$\boldsymbol{\Delta M}$	infinitesimal mass	kg

Variable	Description	SI unit
ϵ_{α_P}	contact ratio	-
ϵ_{IR}	infrared emissivity	-
η	efficiency	-
λ	helix angle of particle path	deg
λ_M	mean helix angle of particle path	deg
μ	friction coefficient	-
μ_i	internal friction coefficient	-
ϕ_s	friction angle between bulk solid and screw surface	deg
ϕ_i	internal friction angle	deg
ρ	density	kg/m^3
σ	Stefan Boltzmann constant	$\frac{W}{m^2K^4}$
ω	selector angular velocity	rad/s
ω_L	angular velocity at load	rad/s
ω_M	angular velocity at motor	rad/s

List of Abbreviations

Variable	Description
CAD	Computer Aided Design
CCW	Counter Clockwise
COTS	Commercial Off The Shelf
CTE	Coefficient of Thermal Expansion
CVCM	Collected Volatile Condensed Material
CW	Clockwise
EPS	Electric Power System
LoC	Lab-on-Chip
NEOs	Near-Earth Objects
OBDH	On Board Data Handling
RML	Recovered Mass Loss
s/c	Spacecraft
SSA	Surface Sample Analyzer
TBD	To Be Determined
TCS	Thermal Control System
TID	Total Ionizing Dose
TRL	Technology Readiness Level

Acknowledgements

I would like to offer my sincere thanks to my advisor, Prof. Michèle Lavagna, for the opportunity she gave me. I thank you my co-advisor, Jacopo Prinetto, for the suggestions, the precious indications and the sustain he has provided me during these months.
Thank you to Alessandro Fumagalli, Andrea Rusconi and his Robotics team of Leonardo in Nerviano for sharing with me the results of their testing activity and their valuable advices.
Thank you to my mum and dad who have always been with me in this beautiful, but sometimes difficult, university experience. Mum and dad, thank you for making me the person I am today. Thank you to my little sister, Elisa, who has grown up with me and who has always supported me. I have tried to be an example for you even when you yourself were a guide for me. A huge thank you to my grandparents, Anna, Aurelia and Giacomo. Everything I have done is also for you, and I hope you are proud of me.
Thank you to my dearest friend Chiara for always being by my side no matter what. We have shared a lot of important moments together, and I hope we will share many others.
Thank you to my second family, my closest friends, Federico, Gaia, Gioele, Lorenzo and Simone for all the laughs, the confidences, the good nights and days have spent together.
Thank you to my dear friend MariaVittoria who knows how to cheer me up every time I need it. Thanks for the beautiful memories we have together. You have become such an important person to me.
Thank you to my friends Ilaria and Riccardo for being there when I need them the most.
Thanks to my friend Camilla for all the funny moments we have spent together.
Thank you to my friends Francesca and Michela for making every summer so special.
Thank you to my friends Alessandro, Elena, Giorgio, Michela, Samuele and Silvia. We have spent five beautiful years together, and I am so grateful not to have lost you over the years. Thank you to my colleagues and friends who have shared these last five years with me. I would like to thank you for all the parties, the study sessions, the dinners, the trips, the university projects and the new friendships you have made me discover. It has been a wonderful journey also thanks to you.